technische universität
dortmund

Picosecond Ultrasonics for the Modulation and Nanoscopy of Semiconductor Lasers

Dissertation

Zur Erlangung des akademischen Grades
Doktor der Naturwissenschaften

Fakultät Physik
TU Dortmund

Thomas Czerniuk

2017

Erster Gutachter:	Prof. Manfred Bayer	(Technische Universität Dortmund)
Zweiter Gutachter:	Prof. Metin Tolan	(Technische Universität Dortmund)
Dritter Gutachter:	Prof. Andrey Akimov	(University of Nottingham)

Datum der Einreichung: 21. Juni 2017
Datum der Disputation: 18. August 2017

Contents

Part I

Introduction

Chapter 1

Motivation and Outline

Light and sound have always been the main tools of mankind to perceive nature and to communicate with each other. Classical *optical* devices based on refractive lenses like telescopes or microscopes made it possible to observe far away and smallest objects beyond the capability of the human eye. Mirrors were used in ancient light houses to send light signals across kilometer distances. Coming from these rather basic elements, more knowledge about the quantum nature of light led to the development of the first laser in the 1960's [76]. Unlike classical light sources, lasers provide coherent, monochromatic light with a low beam divergence. Lasers turned out to be a break-through for new imaging and communication techniques. Most noteworthy is the establishment of global communication networks like the internet that have paved the way for today's information society. These communication networks are operated with semiconductor lasers whose emission is transported via optical fibers [110]. Lasers are also used in modern imaging/ranging techniques like laser scanning or laser range finding, which allow to obtain rapid and high resolution 3D-information about objects [28].

In modern *acoustic* applications, the frequency and intensity of the employed sound waves are tailored for the specific needs. Ultrasound with relatively strong amplitude is used for acoustic levitation [18]. This techniques allows a controllable container-less transportation and is especially useful wherever materials with a high purity are processed, e.g. in electronic or pharmaceutic industries. In the field of sonochemistry, sound is used to support or selectively start chemical reactions [117, 91]. However, the most prominent applications of sound waves aim at imaging or positioning hidden or buried objects by sending out acoustic pulses and detecting their echoes [71]. Widely known examples are echo-sounding and sonar in seafaring to determine the depth of the ocean underneath ships or the position of other (sub-marine) vessels, respectively. Similar seismic methods are used in geophysics for the investigation of the earth's subsurface either out of scientific interest or economic reasons (to find useful deposits like ore or oil). On smaller length scales, non-invasive ultrasound imaging techniques are used to record in-vivo images of biological organisms. Ultrasound involves high-frequency acoustic waves

with wavevectors so short that they allow one to investigate objects as small as a few micrometers [17].

The interaction of light and sound is exploited in *acousto-optical* devices, which often aim at the manipulation of light by sound: ultrasound waves are injected into photoelastic crystals, where they imprint a periodic grating onto the index of refraction. The employed sound wavelengths are on the order of tens of micrometers, such that light is deflected from and optionally frequency-shifted by the imprinted gratings. Applications comprise acousto-optical modulators and acousto-optical filters, for example [105].

In this thesis, the idea is to scale the sound wavelength further down until it is in the same order or even smaller than the wavelength of visible light. The interaction of light with sound in this regime shall be exploited to improve communication and imaging techniques. Two main questions shall be pursued:

"Can such sound waves be used to increase the speed of optical communications techniques?"

and

"Can acoustic echo-sounding techniques with such short acoustic wavelengths be combined with optical methods?"

To answer these questions, semiconductor based light emitters are subjected to experiments involving ultrashort acoustic pulses. A special focus is put on semiconductor lasers due to their importance for communication technologies.

On the one hand, sound will be used to modulate the emission of semiconductor lasers. To this end, ultrafast mechanical vibrations are launched in the studied lasers, where they affect all laser components; i.e., the laser resonator, the active medium, and the pump mechanism. The mechanical vibrations are imprinted into every aspect of the laser's emission, namely the intensity and the wavelength. The future perspective is to realize fast laser clock rates or tailored emission sequences for optical communication techniques this way.

On the other hand, light shall be combined with acoustic imaging techniques. The resolution limit of conventional echo-sounding is determined by the duration of the acoustic signal, which is sent out in the first place and whose echoes are recorded. Acoustic pulses with spatial extents on the order of hundreds of nanometers are injected into semiconductor lasers. These acoustic pulses are too long to resolve the nanometer-scaled layers forming the studied lasers. An interferometric acousto-optical nanoscopy method with an improved resolution is developed. This method allows a characterization with nanometer precision, despite the relatively long acoustic pulse. As another benefit, information about the internal light field distributions can be extracted from the method.

The thesis is structured as follows. This introductory part I is dedicated to sound. It comprehensively reviews the *picosecond ultrasonics* technique, which is used in all

experiments to generate ultrashort acoustic pulses. Part II presents the first experimental results. The work deals with the emission modulation of semiconductor lasers due to ultrafast vibrations. Various aspects are discussed, like the influence of mechanical vibrations on the active medium of the laser and how its manipulation affects the lasing process. Moreover, the interplay of acoustic and optical resonances supported by the nanometer-scaled laser resonator is exploited for an emission modulation with remarkable frequencies. The combination of acoustic imaging techniques with optics is the topic of part III. An ultrafast optical detection scheme for sound is presented along with the interferometric acousto-optical nanoscopy method mentioned above.

Chapter 2

Picosecond Ultrasonics

Sound waves in general are a variation of the density and the pressure inside a medium propagating at its speed of sound. In the case of the semiconductors studied in this thesis, the atoms are crystallized into a lattice with a certain periodicity. One distinguishes between sound waves with wavelengths much longer and of the same order than this characteristic length scale. In the first case, a physical description that assumes a continuum for the solid and the deformation field holds true. In the latter, one needs to take the finite spacing of the crystal atoms into account. Sound waves are treated in the corresponding picture as coherent superpositions of quantized vibrations of the crystal lattice. These collective excitations are denoted *phonons*.

The key tool for all experiments presented in this work are ultrashort acoustic pulses. There are two established techniques for the generation of such pulses. The first one relies on electric metal transducers grown on a piezoelectric substrate, which are used to excite **s**urface **a**coustic **w**aves (SAWs). The available frequency range is limited by the spacing of the metal transducers and typically reaches phonon frequencies of up to 30 GHz [67]. In principle, a pulsed operation of SAWs is possible. Rectangular, sawtooth, and delta-like pulses have been realized via Fourier synthesis recently, although the limited frequency range provides a lower limit of the pulse duration of about 800 ps up to now [108].

The second technique is based on the injection of heat into a metal transducer by a sub-picosecond laser pulse and is referred to as picosecond ultrasonics. The ultrafast increase in temperature following the absorption of the laser pulse sets up a thermal stress in the metal, which launches an acoustic pulse with a duration down to 10 ps [128]. The spatial extent of pulses created this way is only a few tens of nanometers. Acoustic pulses are used in part II to manipulate lasers on a picosecond timescale and in part III to characterize semiconductor heterostructures with nanometer dimensions. Only the picosecond ultrasonics technique provides pulses with the required spatial and temporal finesse.

Due to the particular relevance of the *picosecond ultrasonics* technique for all exper-

iments presented here, this introductory part shall give a review of this method. It starts with a short recap of the two theoretical models necessary to describe mechanical vibrations. In the beginning, the phonon concept will be presented in section 2.1. In this picture, ultrafast acoustic pulses can be considered as wave packages of coherent phonons. In the following section 2.2, the second theoretical framework, namely continuum elasticity as the long wavelength limit for phonons, will be discussed. With the help of this framework, the generation process of the ultrashort acoustic pulses by means of optical excitation with lasers will be detailed in section 2.3. In all of the conducted experiments, the acoustic pulses need to propagate from the place of their creation through elastically nonlinear and dispersive media to the structures they are supposed to manipulate/investigate. During this propagation, the shape of the acoustic pulses may significantly change and the corresponding equation of motion will be highlighted in section 2.4. Nonlinear propagation effects can lead to the formation of shockwaves and, ultimately, acoustic solitons [54].

2.1 Phonons

In order to describe lattice vibrations in a crystal on a microscopic level, it is necessary to solve the crystal's Hamiltonian, which contains both the electronic and the atomic nuclei system as well as their interaction terms. Since the coulomb forces acting on the electrons and nuclei are the same, but the electron's mass is several orders of magnitude smaller than the nuclei mass, the electron dynamics evolve on a faster timescale. In the *Born-Oppenheimer-approximation* these two subsystems are therefore separated and solved independently: in a first step, the electronic eigenenergies are obtained for fixed core positions. Afterwards, the electronic eigenenergies, in which the positions of the atoms enter as parameters, are treated as an effective potential for the atoms.

The theoretical description given here and in the next section closely follows Ref. [35]. Consider N atoms in d dimensions with positions $\underline{\vec{R}} = \left(\vec{R}_1, ...\vec{R}_N\right)$. The Hamiltonian is given by

$$H = \sum_{n=1}^{N} \frac{\vec{P}_n^2}{2M_n} + V_{\text{eff}}\left(\underline{\vec{R}}\right) , \tag{2.1}$$

where $\vec{P}_n$ is the momentum of the n-th atom, M_n its mass, and V_{eff} is the effective potential of the atomic nuclei, which already contains the electronic system. If the atoms are displaced to a small extent $\vec{u}_n$ from their equilibrium positions at $\underline{\vec{R}}^0 = \left(\vec{R}_1^0, ..., \vec{R}_N^0\right)$

$$\vec{R}_n = \vec{R}_n^0 + \vec{u}_n \, , \tag{2.2}$$

the effecitve potential V_{eff} can be expanded into a Taylor series:

$$V_{\text{eff}} = V_{\text{eff}}\left(\underline{\vec{R}}^0\right) + \sum_{n,\alpha} \left.\frac{\partial V}{\partial R_{n\alpha}}\right|_{\underline{\vec{R}}^0} u_{n\alpha} + \frac{1}{2} \sum_{n\alpha,n'\alpha'} \underbrace{\left.\frac{\partial^2 V}{\partial R_{n,\alpha'} \partial R_{n',\alpha'}}\right|_{\underline{\vec{R}}^0}}_{\Phi_{n\alpha,n'\alpha}} u_{n\alpha} u_{n'\alpha'} + \dots . \quad (2.3)$$

Here, the indices n and n' run over all atoms while α and α' run over all dimensions. The first term is a constant energy offset, which is associated with the energy of the system in equilibrium. The second term includes the first derivatives and vanishes because the effective potential is minimized in the equilibrium position: $\frac{\partial V}{\partial R_{n\alpha}}\left(\underline{\vec{R}}^0\right) = 0$. In the harmonic approximation, this series is truncated after the third term with the second order derivatives. An additional index μ is required for crystals with r atoms of different masses M_μ in a unit cell. The equation of motion for the μ'th atom in the n'th unit cell is given by:

$$M_\mu \frac{\partial^2 u_{n\alpha\mu}}{\partial t^2} = -\sum_{n'\mu'\alpha'} \Phi_{n\mu\alpha,n'\mu'\alpha'} u_{n'\mu'\alpha'} \,. \quad (2.4)$$

A solution is obtained by a plane wave ansatz with a wavevector $\vec{q}$ for the spatial and a frequency $\omega(q)$ for the temporal dependence. For each $\vec{q}$ there are $d{\cdot}r$ eigenvalues for $\omega(q)$. The corresponding $d{\cdot}r$-dimensional eigenvectors can be written as a set of d-dimensional vectors - one for each of the r atoms of the crystal basis - which describe the vibration's polarization.

Such a plane wave in a crystal is associated with a quasi-particle called phonon. Phonons can be classified by their polarization: if the atoms are moving in parellel or perpendicular to the direction of the wavevector $\vec{q}$, the phonon is called longitudinal or transverse, respectively. Crystals with more than one atom per unit cell can experience vibrations where the different types of atoms are oscillating in anti-phase. These are optical phonons, in contrast to acoustic phonons, where neighboring atoms are moving in phase. Summarized, there are one longitudinal acoustical (LA) and $(d-1)$ transverse acoustic phonons (TA) as well as $(r-1)$ longitudinal optical (LO) and $(r-1)(d-1)$ transverse optical phonons (TO). An overview of the two kinds of phonons and their polarization states is sketched in the left panel in Fig. 2.1. On the right hand, the typical dispersion relation of a 1-dimensional crystal with next-neighbour interaction only and two different kinds of atoms is sketched. While the acoustic phonon branch (LA) is linear for $q \ll \pi/a$ and vanishes for $q = 0$, the frequency of optical phonons remains non-zero everywhere. Towards the boundaries of the first Brillouin zone at $q = \pi/a$, with a being the crystal lattice constant, the dispersion of both the LA and the LO phonon flattens, leading to a decreased phonon group velocity.

The phonon occupation number fulfills the *Bose-Einstein-distribution* in thermal equilibrium and the phonons possess a random phase. In order to generate high amplitude

deformation pulses, which are the key tool for all experiments in this work, it is necessary to create coherent acoustic phonons that build up to a single acoustic pulse. The classical elasticity theory provides a suitable framework to describe the dynamics of such acoustic pulses and will therefore be reviewed in the next section.

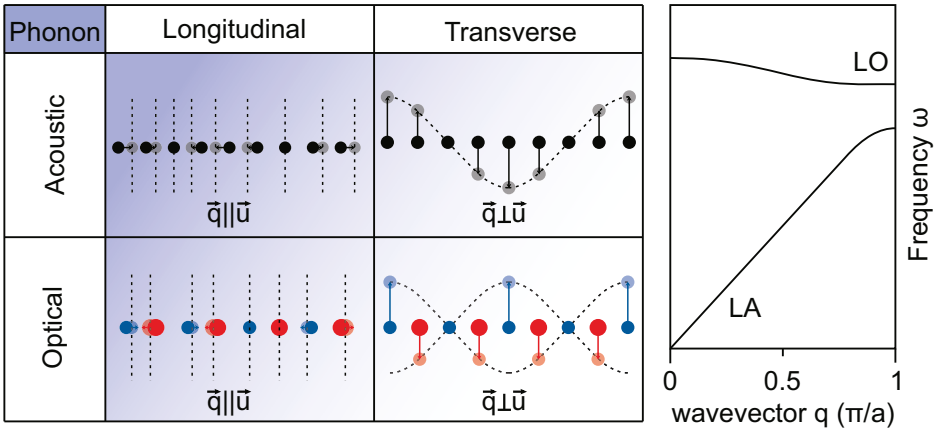

Figure 2.1: Different classes of phonons and their characteristics. Panel (a): Acoustic and optical phonons and their two polarization states. Optical phonons require at least two atoms in the unit cell, which oscillate in anti-phase. Panel (b): Typical dispersion relation for a 1-dimensional ($d = 1$) crystal with two atoms ($r = 2$). The dispersion of the acoustic branch (LA) is linear for $q \ll \pi/a$, while optical phonons (LO) may also occur for $q = 0$.

2.2 Elasticity Theory

The classical elasticity theory describes how a body is responding to internal and external forces. In the corresponding picture, a solid is assumed to be a continuum and so is the displacement field. It is only valid for phonons in the long wavelength limit $q \ll \pi/a$, for which the finite spacing of the lattice is negligible and the crystal can be treated as a continuum. From here on, only one atom per unit cell is assumed and optical phonons are not being considered anymore. In the long wavelength limit, the variation of the displacement for neighboring lattice sites R_n and $R_{n'}$ is only small and may be

approximated by the tailor expansion

$$u_{n'\alpha'} = u_{\alpha'}(R_{n'}) = u_{\alpha'}(R_n) + \sum_{\beta} \frac{\partial u_{\alpha'}(R_n)}{\partial r_\beta}(R_{n'\beta} - R_{n\beta}) \tag{2.5}$$
$$+ \frac{1}{2}\sum_{\beta\beta'} \frac{\partial^2 u_{\alpha'}}{\partial r_\beta \partial r_{\beta'}}(R_{n'\beta} - R_{n\beta})(R_{n'\beta'} - R_{n\beta'}) + \dots$$

If this expression is inserted into Eq. (2.4), the displacement field is turned into a continuum $u(R_n, t) \to u(r, t)$, and the mass density ρ is introduced, the following wave equation can be found:

$$\rho \frac{\partial^2 u_\alpha}{\partial t^2} = \sum_{\alpha'\beta\beta'} C_{\alpha\alpha'\beta\beta'} \frac{\partial^2 u_{\alpha'}(r,t)}{\partial r_\beta \partial r_{\beta'}}. \tag{2.6}$$

Here, the 4th rank tensor of elastic coefficients or stiffness tensor $C_{\alpha\alpha'\beta\beta'}$ appears [35]. It is a macroscopic quantity describing the response of a solid towards deformations and is defined by a sum over the microscopic interatomic force constants $\Phi_{n\alpha,n'\alpha'}$ and the atomic distances $(R_{n'\beta} - R_{n\beta})$. In the macroscopic picture of classical elasticity theory, an infinitesimal volume element dV is considered, exerted to forces $d\vec{f}$ from its neighboring volume elements via their common surfaces $d\vec{A}$. Since forces and surfaces are not always perpendicular (e.g. shear strains), they are related via a 2nd rank tensor, the stress tensor σ

$$d\vec{f} = \sigma d\vec{a}, \tag{2.7}$$

which has the dimension of pressure. If there are no external forces acting on a body, the total force $\vec{F}$ on dV can, on the one hand, be deduced from the stress tensor via a surface integral and, on the other hand, from the left side of Eq. (2.6):

$$\vec{F} = \oint\limits_{O(dV)} \sigma d\vec{a} = \int\limits_{dV} \rho \frac{\partial^2 u_\alpha}{\partial t^2} dV. \tag{2.8}$$

After applying Gauss's theorem to the surface integral and comparing the two integrands, one can find the relation between the 2nd rank stress tensor and the 4th rank tensor of elastic coeffients, which turns out to be linear. They are connected by the strain tensor η

$$\sigma_{\alpha\beta} = C_{\alpha\beta\alpha'\beta'}\eta_{\alpha'\beta'} \tag{2.9}$$
$$\eta_{\alpha\beta} = \frac{1}{2}\left(\frac{\partial u_\alpha}{\partial r_\beta} + \frac{\partial u_\beta}{\partial r_\alpha}\right). \tag{2.10}$$

While the displacement $\vec{u}$ itself does not describe a deformation of a body (e.g., a constant displacement is equivalent to a translation of the whole body), its variation does.

If different parts of a body are moved to a different extent, the body is stretched or compressed. The strain tensor η describes these deformations: diagonal components of η account for uniaxial deformations, while the off-diagonal elements represent shear strains. Eq. (2.9) is referred to as the generalized version of *Hook's law*, because it connects a deformation η via force constants C to the equivalent of a force σ. The equation of motion for an acoustic wave traveling through the crystal is simplified to

$$\rho \frac{\partial^2}{\partial t^2} u_\alpha = \sum_\beta \frac{\partial}{\partial r_\beta} \sigma_{\alpha\beta}. \tag{2.11}$$

In the following section, the generation of acoustic pulses by the *picosecond ultrasonics technique* will be detailed using this framework. The process is based on the creation of non-equilibrium coherent longitudinal acoustic phonons, which superimpose to an ultrashort acoustic pulse. Both pictures will be needed: (i) the elasticity theory to account for the thermal stress following the absorption of the laser pulse in the generation process; (ii) the phonon concept to understand the nonlinear and dispersive propagation effects.

2.3 Generation of Picosecond Acoustic Pulses

The picosecond ultrasonics technique has been established in the 1980s and still provides the shortest acoustic pulses nowadays. It is based on the optical excitation of a strongly absorbing material: a metal film is illuminated by a sub-picosecond laser pulse and absorbs the optical energy within several nanometers. The following rapid thermal expansion launches an acoustic pulse propagating away from the surface of the metal film. In the experiments performed here, the metal film was deposited on the backside of the samples prior to the experiments. This means that the acoustic pulse needs to travel from the sample's backside through the substrate before reaching the studied structures located on the front. The different stages from the optical excitation and the creation of the acoustic pulse to the propagation through the substrate will be detailed in this section.

This review will closely follow the theory developed in the original publication in Ref. [128]. Consider a short laser pulse with an energy Q, which is absorbed by a metal film with an absorption length ς. The full width at half maximum (FWHM) radius of the laser spot r shall be much larger than this absorption length and than the film's thickness d, too. The absorbed energy leads to an increase in temperature ΔT, which only depends on the distance z from the surface of the metal film

$$\Delta T(z) = \frac{(1-R)Q}{\pi r^2 \varsigma C} \exp\left(-z/\varsigma\right). \tag{2.12}$$

In this equation, R is the reflectivity of the metal film and C is its heat capacity per unit volume, which translates absorbed energy into an increase in temperature. Fig 2.2

depicts the geometry. In this simple picture, the energy is directly transferred from the electrons absorbing the light in the first place to the crystal lattice. However, the electrons may diffuse through the metal film before losing their energy and thus the final temperature profile may vary from Eq. (2.12). This effect is discussed later in this section.

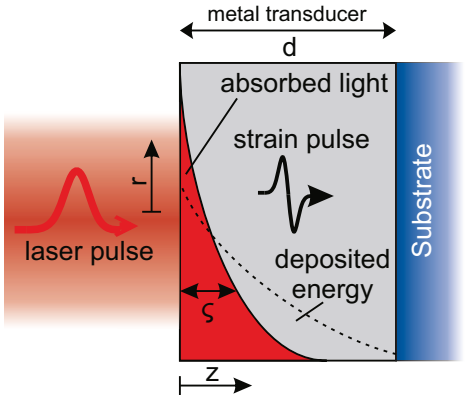

Figure 2.2: Schematic of the generation process of ultrashort acoustic pulses: A laser pulse is absorbed by a metal film in a volume close to the surface (red area). Due to electron and thermal diffusion, the final lattice temperature profile (dashed line) differs from the initial energy deposition. The rapid thermal expansion launches a strain pulse that propagates through the metal film.

In an elastically isotropic medium, the rapid temperature increase leads to an isotropic thermal stress

$$\sigma_{th} = -3B\beta\Delta T(z), \tag{2.13}$$

where B is the bulk modulus and β the linear expansion coefficient of the material. If an isotropic material is assumed, a stress profile that only depends on z will also lead to motion only along this direction. The only non-vanishing strain tensor component thus is η_{zz} and the stress-strain relation Eq. (2.9) simplifies to:

$$\sigma_{zz} = \underbrace{3\frac{1-\nu}{1+\nu}B\eta_{zz}}_{\text{Hook's law}} - \underbrace{3B\beta\Delta T(z)}_{\text{thermal}}. \tag{2.14}$$

Here, the component C_{3333} of the stiffness tensor is expressed by the bulk modulus B and Poisson's ratio ν. The thermally induced stress is included as an inhomogeneous stress source. For simplicity, the indices will be omitted in the following.

The equation of motion for the strain η can now be deduced from Eq. (2.11). Together with the initial condition of zero strain everywhere ($\eta(z) = 0$) and the boundary condition of a vanishing stress at the metal surface ($\sigma(z = 0) = 0$), an analytical solution can be found, which can be divided into two parts. The first is a static strain at the metal surface due to the long-lived thermal expansion, while the second one is an acoustic strain pulse, which will leave the initially heated surface region and propagate into the metal film. Note that the driving force of this pulse is not the thermal stress itself, but its variation.

The shape of the propagating strain pulse is given by

$$\eta(z,t) = \underbrace{\frac{3(1-R)Q\beta B}{2\pi r^2 C \varsigma v^2}}_{\eta_0} \cdot \exp\left(-|z-vt|/\varsigma\right)\mathrm{sgn}(z-vt). \tag{2.15}$$

It is localized around $z = vt$ and moves with a sound velocity $v^2 = 3\frac{1+\nu}{1-\nu}\frac{B}{\rho}$. Two main regions can be distinguished: a leading compressive part ($\eta < 0$) for $z < vt$, followed by a discontinuity at $z = vt$, and a tensile part ($\eta > 0$) afterwards. The strain amplitude can be controlled by the optical excitation energy and reaches typical values of 10^{-4}-10^{-3}. The strain profile decays exponentially away from the center on a length scale defined by the optical absorption length ς.

The instantaneous energy transfer from the hot electrons to the lattice assumed so far is not valid, but several relaxation processes need to be considered, which are sketched in Fig. 2.3. The electrons and the lattice are assumed to form subsystems to which an individual temperature is assigned [123]. The electronic subsystem initially absorbs the laser pulse and stores all energy, so that its temperature T_e increases by several hundred K. In the interval between the optical excitation at $t = 0$ and the time at which the strain pulse leaves the heated area at $t = \tau = \varsigma/v$, several processes occur: first, the electrons start to diffuse through the metal film, thus spreading the heat to a larger volume than initially heated. This effect cannot be neglected when the diffusion constant D_e is of the same order of magnitude as τ, which is usually the case for metals. At the same time, the electrons start to lose their energy to the lattice with a rate governed by the electron-phonon-coupling. As a result, the lattice temperature T_l starts to increase and thermal diffusion with a constant D_{th} sets in. Finally, the electronic and the lattice subsystem are in thermal equilibrium with each other after the strain pulse has left the heated area. The strain pulse becomes broader and smoother than initially considered according to Eq. (2.15) and can be modeled by the derivative of a Gaussian.

After the propagation through the metal film is completed, the acoustic pulse reaches the interface to the substrate [cf. Fig. 2.2]. At this interface, the acoustic pulse is partly reflected and transmitted according to the coefficients of acoustic reflection r and transmission t, respectively

$$r = \frac{Z_{\text{sub.}} - Z_{\text{film}}}{Z_{\text{sub.}} + Z_{\text{film}}} \tag{2.16}$$

$$t = \frac{2Z_{\text{sub.}}}{Z_{\text{sub.}} + Z_{\text{film}}}, \tag{2.17}$$

where $Z = \rho v$ is the acoustic impedance of a material [122]. It is advantageous to choose two materials with a similar acoustic impedance in order to optimize the injection into the sample. The acoustic pulse has to travel through substrates with thicknesses ranging from several ten to hundreds of micrometers in the experiments performed in this thesis. These thicknesses are orders of magnitude larger than the thickness of the metal film,

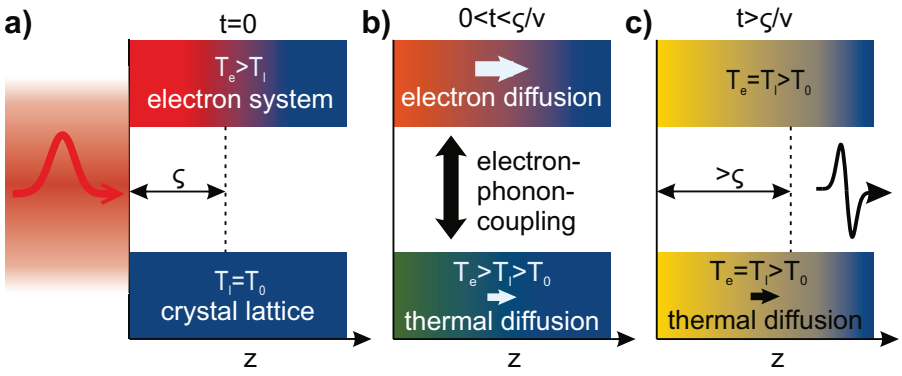

Figure 2.3: Stages of the transfer of the optical energy to the crystal lattice. Panel (a): The electronic system of the metal absorbs the light and reaches a temperature T_e on a length scale given by the absorption length ς. The color indicates the heat deposition. Panel (b): In the time interval between excitation and before the strain pulse leaves the heated area, the electrons diffuse through the metal film and spread the heat. Via electron-phonon-coupling energy is transferred to the crystal, where thermal diffusion sets in simultaneously. Panel (c): Electron and lattice systems have thermalized and the strain pulse has left the surface area.

which is about 100 nm. During the propagation, the shape of the strain pulse may be altered due to anharmonic and dispersive effects that accumulate with longer distances and are especially important for high strain amplitudes (i.e. for high optical excitation densities). The mechanisms responsible for this evolution and the final shape of the acoustic pulse are discussed in the following section.

2.4 Nonlinear Acoustic Pulse Propagation

High amplitude strain pulses cannot be described by the equation of motion deduced earlier in the elasticity theory [cf. Eq. (2.11)]. The first shortcoming is the harmonic approximation for the effective atomic core potential. In terms of elasticity this is related to Hook's law that linearly links strain and stress and is not true anymore for strong deformations (i.e. displacements) of the body. Moreover, the finite spacing of the atoms becomes important for phonons with wavelengths as short as the lattice constant, which corresponds to frequencies of a few hundred GHz for most semiconductor substrates. For such phonons, a nonlinear dispersion needs to be considered (cf. Fig. 2.1). Both effects are discussed in the following.

Including higher orders of strain tensor components in the definition of the stress tensor in Eq. (2.9) introduces the anharmonicity into the system and leads to a modified equation of motion. Since the consideration is still restricted to an isotropic medium as

well as stress and motion only along the z-direction, the simplified nonlinear equation of motion is given by

$$\rho\frac{\partial^2 u}{\partial t^2} = \frac{\partial^2 u}{\partial z^2}\left(C_2 + \frac{\partial u}{\partial z}C_3\right), \tag{2.18}$$

where C_2 is associated with the linear and C_3 with the nonlinear propagation [130]. While C_2 is a combination of second order elastic constants, C_3 also contains third order elastic constants. From this equation follows that the sound velocity is not constant anymore, but a function of the strain ($\eta = \partial u/\partial z$). For most solids C_3 is negative leading to a higher and lower sound velocity for compressive ($\eta < 0$) and tensile strain ($\eta > 0$), respectively. As a result, the shape of the strain pulse is not conserved during propagation.

To account for the flattening of the dispersion towards the Brillouin zone edge, a parameter $\beta > 0$ is introduced to the dispersion relation

$$\omega(k) = ck - \beta k^3. \tag{2.19}$$

With both mechanisms included, the equation of motion for the strain reads

$$\rho\frac{\partial^2 \eta}{\partial t^2} = C_2\frac{\partial^2 \eta}{\partial z^2} + C_3\frac{\partial \eta}{\partial z}\left(\eta\frac{\partial \eta}{\partial z}\right) + 2v\rho\beta\frac{\partial \eta^4}{\partial z^4}. \tag{2.20}$$

and has the form of the *Korteweg-de-Vries* equation [130]. The impact of the nonlinearities crucially depends on the initial strain amplitude and the travel distance during which the nonlinear effects accumulate. Starting from an input strain pulse, the *Korteweg-de-Vries* equation needs to be numerically solved to simulate the final profile for a given propagation length.

The calculated strain pulse for a 100 nm thick aluminum film is plotted for an initial optical excitation density of $3\,\mathrm{mJ/cm^2}$ [cf. Fig. 2.4 (a)] and $10\,\mathrm{mJ/cm^2}$ [cf. Fig. 2.4 (b)]. Black curves represent the input strain pulses injected into the substrate and feature a bipolar shape, which can be modeled by the derivative of a Gaussian. The part that is not injected into the substrate at first, but is reflected at the interface to the substrate is also included and trails behind the main pulse at t=35 ps after it has completed one additional round trip in the metal film. Its sign is flipped due to the reflection at the open surface of the metal film. After the propagation through a substrate consisting of 100 µm of (100)-orientated GaAs, the profile has significantly changed (red curves). In the case of the lower excitation density, the dominant mechanism is the anharmonicity: the parts of the pulse with compressive strain ($\eta < 0$) move faster than the parts with tensile strain ($\eta > 0$), leading to the formation of a shockwave with a N-shape. Due to the sharp edges, the corresponding phonon spectrum is broadened and contains phonons of higher frequency [cf. Fig. 2.4 (c)] . For the higher excitation density, the shockwave becomes more pronounced and the sharper edges are accompanied by phonons reaching

frequencies up to the THz-regime [cf. Fig. 2.4 (d)]. For such phonons, the dispersion becomes nonlinear and the group velocity is reduced. There is a stable solution for compressive strain wave packages called solitons, in which the two effects balance each other. They propagate faster than the speed of sound and three of them appear in front of the shockwave in Fig. 2.4 (b) around t=-15 ps (indicated by the arrows). Solitons are of particular interest, due to their short duration of only a few picoseconds. They provide an extraordinary high spatial and temporal resolution and therefore are very promising candidates to study semiconductor heterostructures [54].

There are several ways to tailor the strain pulse to the specific needs. In order to generate high frequency phonons - or for the best spatial resolution even solitons - a long propagation distance is favorable, because the nonlinear effects accumulate. However, damping of the strain pulse during the propagation also has to be taken into account. There are two contributions, depending on the temperature and the phonon frequency: the first is the anharmonic interaction of the launched longitudinal acoustic phonon with the thermal phonon bath; this is the dominant mechanism for phonons with frequencies below approximately 250 GHz. Here, the phonons are assumed to set up a slowly varying strain field that shifts the frequencies of the thermal phonons out of equilibrium, so that relaxation within a time constant τ_{th} occurs. The associated damping coefficient scales linearly with the temperature T and the phonon frequency dependence is given by $\omega^2\tau_{\mathrm{th}}^2/(1+\omega^2\tau_{\mathrm{th}}^2)$. For higher frequencies, phonon-phonon-scattering or *Herring* processes are the main contribution. The interaction strength scales quadratic in the phonon frequency and varies with T^3 [22]. Especially for high frequency phonons, it is important to minimize the attenuation by cooling the sample down to cryogenic temperatures.

The conditions for the acoustic pulse generation need to be matched to the desired experiment. Experiments exploiting high frequency components or solitons require a high optical excitation density for maximum initial strain amplitude and a non-vanishing propagation distance such that the nonlinear features come into play. It is necessary to account for the increased damping of these phonons by cooling the sample down to cryogenic temperatures. In contrast, experiments at room temperature can only be performed with a thin substrate and thus do not offer the possibility to work with solitons, for example.

After the strain pulse has traversed the substrate, it will reach the structures to be investigated, located on the side of the sample opposite to the metal transducer. In this work, the acoustic pulses are exploited for two purposes, namely (i) the modulation of the light emission from semiconductor lasers and (ii) the nanoscopy of layered semiconductor heterostructures. In the following second part of this thesis, the different possibilities to modulate the light emission intensity and the emission wavelength of semiconductor lasers with picosecond ultrasonics are discussed. This involves the interaction of the acoustic pulse with the gain material of the lasers, which is the main reason for the intensity modulation, as well as the interaction with the optical resonator, which offers a

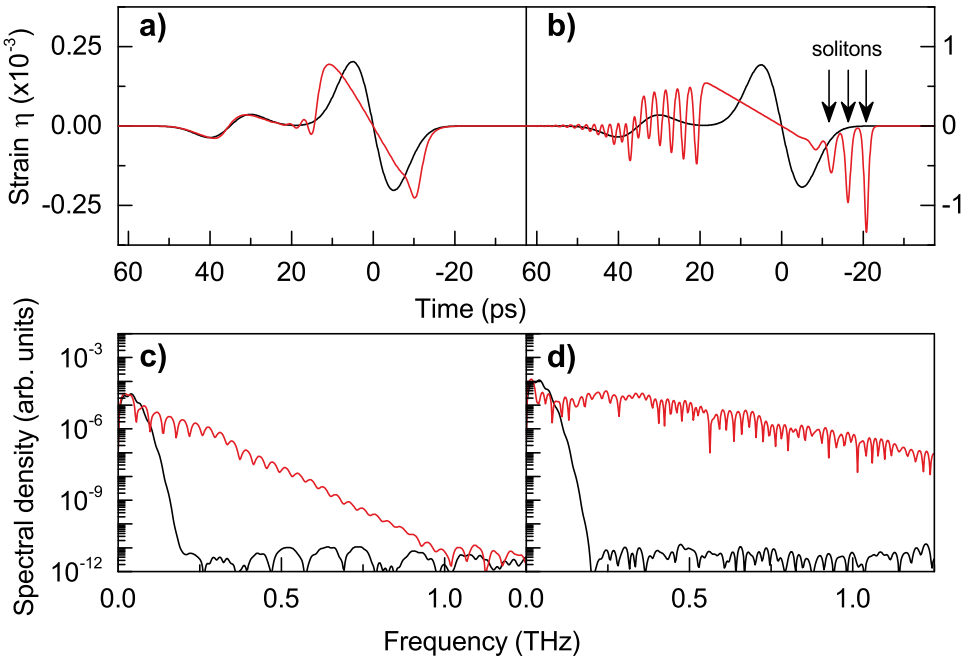

Figure 2.4: Nonlinear strain pulse propagation for two different excitation densities and corresponding phonon spectra: Panel (a): Temporal strain pulse profile $\eta(t)$ for an optical excitation density of 3 mJ/cm^2 before (black) and after (red) the propagation through 100 µm (100)-GaAs. After the propagation, the strain pulse shows a N-shape. Panel (b): For an increased excitation density of 10 mJ/cm^2, the sharper N-shape contains high frequency phonons and nonlinear dispersion comes into play. As a result, solitons appear (indicated by the arrows). Panel (c): Phonon spectra before (black) and after (red) the propagation through the substrate for the strain pulses shown in (a). The phonon spectrum gets significantly broadened. Panel (d): The phonon spectrum of the strain pulse with solitons shown in panel (b) contains phonons up to 1 THz.

route to manipulate the emission wavelength. In the third part of this thesis, the acousto-optical nanoscopy based on picosecond ultrasonics will be presented. These experiments are, on the one hand, conducted in samples with substrates that lack nonlinearities, such that the acoustic pulses remain short and Gaussian. On the other hand, also rather thick substrates that feature strong nonlinearities are used in combination with phononic low pass filters in order to further tailor the acoustic spectrum.

Part II

Semiconductor Laser Emission Modulation

Introduction

The first ruby laser was successfully demonstrated in the 1960's by Theodore Maiman as a source of coherent, monochromatic light with high brilliance [76]. In the first years, engineers and scientist were obviously not prepared for its invention and the laser was said to be a 'solution looking for a problem'. The historic publication of Maiman was even turned down by publishers due to a lack of novelty [47]. However, already in 1969, researchers used laser radiation to measure the distance between the earth and the moon in a spectacular experiment: they sent a laser beam to the moon that was reflected by a retroreflector, which the astronauts of the Apollo 11 mission had left on the surface [13]. From the time of arrival of the laser pulse back on the earth, the distance between earth and moon was measured with a precision of 3 cm.

Coming from these rather abstract beginnings, lasers nowadays affect almost every aspect of modern life. There are manifold medical applications of lasers, ranging from surgeries with laser-scalpels, to laser-assisted therapies (like lithotripsy for the treatment of kidney stones or phototherapy, for example) and diagnostics. Lasers are used to cut, drill, and weld with unsurpassed precision in industrial manufacturing processes. For the production of micro-electronics, photolithography with UV lasers is essential to write chip structures into semiconductor substrates. Lasers helped to shrink the size of chips and transistors to reach faster processing speeds and facilitated the rise of electronics which culminated in the 'Digital Revolution'. From 1997 to 2007, the relative amount of digitally stored information rose from 3 % to 94 % [55]. The possibility to process huge amounts of data with efficient computers goes hand in hand with the demand for huge data storage devices and fast communication channels. Lasers were mainly related to the fabrication process of microchips until the 1980s, but started to play an active role for the information technology afterwards with the invention of new photonic applications. Optical data storage devices like CDs, DVDs, or BluRays were the state-of-the-art for many years.

Today, one of the most important application of lasers for information technology is optical fiber communication. Data transport via light has several advantages compared to the classical transport of electrical signals via copper cables: lower resistance, faster transportation of information, less material cost, and the ability to transfer several optical wavelengths at once. Using a broad optical transmission spectrum allows one to

send several signals simultaneously, since photons barely cross-talk. Copper cables were successively replaced in the near past for these reasons: starting on global distances, the first submarine optical communication cable was laid between Britain and the Isle of Man in the early 1980s. Shortly after this, all intercontinental copper cables were replaced by optical fibers enabling the world-wide internet. In more recent years, the distribution of broad-band internet among private households is realized by optical fibers laid inside cities. The trend to replace copper wires by optical connections on ever shorter distances has reached microchips now. In integrated circuits with nanometer-sized transistors, the copper connectors are tightly packed. Due to parasitic capacities, wire cross-talk, and signal propagation delay, the communication between transistors may take as long as the computation itself. In 2000, a 'looming crisis' due to the 'interconnect bottleneck' was predicted [88]. Optical interconnects on-chip or from chip-to-chip are supposed to replace copper connectors in future generations of electronics. Due to the steadily increasing importance of light-based technology, the UN General assembly announced the year 2015 to be the 'International Year of Light and Light-based Technologies' [87].

The rapid increase in data throughput of optical fibers is mostly driven by advanced multiplexing techniques and the possibility to use more and more wavelengths in parallel. While the record transmission rates for short distances (<200 km) rose from 14 terabit/s in 2006 [124] to 1 petabit/s in 2012 [125], the modulation bandwidth of the employed lasers was not even doubled from 1997 to 2012 [69, 133]. The current technological limit is approaching frequencies on the order of 30 GHz, which is still far from the theoretical capability of the employed lasers. Their intrinsic cut-off frequency is defined by the picosecond lifetime of photons in the cavity and on the order of several hundred GHz; there is consequently a huge room for improvements, until the intrinsic limit comes into play.

There are several techniques that allow to modulate the emission intensity of a laser. The first one is named Q-switching. The quality of the optical resonator is artificially worsened by implementing a Q-switch, for example an acousto-optical modulator (AOM). While an AC-bias is applied to the AOM, light from inside the cavity is deflected out, which creates a huge optical loss channel and effectively suppresses lasing. The laser is nevertheless pumped continuously and the energy is released in a massive laser pulse upon switching the AOM off. This technique is the method of choice, when huge peak powers are desired. The fastest reported active Q-switch operation takes place at a repetition rate of 3 GHz and with pulse durations as short as 20 ps [4].

Shorter pulse duration down to femtoseconds are obtained with a second technique, called Mode-locking. The idea here is to excite many photonic modes at once and lock their phases, such that they superimpose to a single ultrashort pulse in the time domain. The pulses emitted by mode-locked lasers can be as short a few femtoseconds and the repetition rate might be as high as 200 GHz [3]. However, the output cannot be controlled on these timescales.

The modulation scheme employed for data transfer through optical fibers is based on a direct modulation of the pump excitation. Electrically driven semiconductor lasers are used to convert electronic into optical signals. The main bandwidth limitation is due to electric parasitic capacities and self-heating [118].

In this part of the thesis, picosecond acoustic pulses are injected into semiconductor lasers. Nonlinear acoustic pulses contain sub-terahertz phonons, which manipulate the laser on its intrinsic timescale. Picosecond ultrasonics therefore offer a promising new tool to modulate semiconductor lasers in terms of emission intensity and wavelength faster than it is possible up to now. This part is structured as follows: chapter 3 briefly reviews laser physics in general and presents how each laser component is realized in the studied semiconductor lasers. Based on these considerations, the influence of ultrafast vibrations on every laser component will be discussed: chapter 4 deals with the interaction of coherent phonons with the active medium of a laser; the following chapter 5 elucidates the role of the resonator; and finally the influence of the excitation scheme is discussed in chapter 6.

Chapter 3

Vertical-Cavity-Surface-Emitting-Lasers

There are two commonly used types of semiconductor lasers, namely **l**aser **d**iodes (LDs) and **v**ertical-**c**avity-**s**urface-**e**mitting-**l**asers (VCSELs). The main difference between the two classes is the design of the resonator. In the case of the LD, which basically consists of a chip with a n-p-junction, the chip's side surfaces are used as the reflectors, offering a sufficient reflectivity for laser operation throughout a broad wavelength spectrum. The light field is emitted from the side of the chip with a rather large divergence, which makes a coupling into optical fibers challenging [83]. In contrast to that, VCSELs rely on microcavities, resonators supporting only a specific wavelength (and the respective higher harmonics). The light field is emitted from the top surface of the laser and provides a much better divergence. Moreover, the cross sectional profile of the emitted optical mode can be tailored by adding oxide masks to the surface [58]. This way, the injection into optical fibers can be optimized, so that this class of lasers is the common choice for optical communication networks and therefore studied here.

Besides the microcavity resonator, which all VCSELs have in common, there is a large variety of possible active media, pumping mechanisms and geometries designed for the specific needs. These specific needs comprise, for example, a low laser threshold [96], high optical output power [60], or a low beam divergence [115]. This chapter gives a comprehensive overview of the different kinds of VCSEL studied in this work and is divided into two sections. Section 3.1 starts with a short recapitulation of the important key figures and the basic constituents of lasers in general. Section 3.2 describes how these constituents are realized in VCSELs. It will address simple VCSEL layouts, like an optically pumped planar microcavity structure, as well as state-of-the-art designs, namely electrically driven micropillar lasers used for advanced applications like polariton lasing [106] and threshold-less lasing [94].

3.1 Laser Operation

The three basic components of a laser are the active medium, the resonator and a pump mechanism. Their function and characteristics will briefly be reviewed in this section based on the description given in Ref. [82].

The active medium provides electronic levels that can couple to an external electric field and thereby absorb or emit a photon; the latter due to spontaneous or stimulated emission. In the simplest case of a two-level system coupled to a monochromatic electric field, the rate equation for the population densities N_1 and N_2 of the ground state $|1\rangle$ and the excited state $|2\rangle$, respectively, read

$$\begin{aligned} \dot{N}_1 &= -\Gamma_1 N_1 + A_{21} N_2 + \sigma(\omega)\Phi\left(N_2 - N_1\right) \\ \dot{N}_2 &= -\Gamma_2 N_2 - A_{21} N_2 - \sigma(\omega)\Phi\left(N_2 - N_1\right). \end{aligned} \tag{3.1}$$

Here, scattering of the electrons out of the two-level system via phenomenological rates Γ and spontaneous emission with the respective Einstein coefficient A_{21} is included. The last term is due to the interaction of the electric field and the two level system and describes absorption and stimulated emission, respectively. The photonic flux Φ of the external electric field $E = E_0 \exp(i\omega t)$ is given by its intensity I over the photon energy $\hbar\omega$. Photons emitted via stimulated emission have the same direction, energy and phase as the photons inducing the process. The interaction cross section $\sigma(\omega)$ can be expressed by the Einstein coefficient B_{12} for stimulated emission

$$\sigma\left(\omega\right) = \frac{\hbar\omega}{c} B_{21} S\left(\omega\right). \tag{3.2}$$

The function $S(\omega)$ denotes the linewidth of the electronic transition hosted by the active medium. Usually it is a normalized Lorentzian profile, where the center is defined by the frequency ω_0 associated with the transition energy and where the broadening is given by the total dephasing rate of the system. That means that for the most efficient laser operation, the frequency of the external field should match the resonance of the active medium and the detuning $\Delta = \hbar\left(\omega - \omega_0\right)$ must vanish. Moreover, one can see that the system is loosing energy for $\dot{N}_2 < 0$, which is the case when energy is converted into light. To achieve this situation, the electrons must be pumped from the ground state into the excited state. The pump can be included by a phenomenological pump rate from $|1\rangle$ to $|2\rangle$ in the rate equations. When a population inversion is reached due to pumping and $N_2 > N_1$, the stimulated emission becomes the dominant interaction term. The energy brought into the system by the pump is then transferred into the coherent light field.

The continuity equation for a propagating lightfield inside the active medium given below contains the homogenous part on the left and the inhomogeneous part due to the

light-matter-interaction on the right side

$$\frac{1}{c}\frac{\partial}{\partial t}I + \frac{\partial}{\partial z}I = \sigma(\omega)I\left(N_2 - N_1\right) = g(\omega)I. \tag{3.3}$$

If the active medium is considered to be placed in a resonator built from two reflectors with reflectivities R_1 and R_2, the coherent lightfield intensity is increased after each round trip if the losses are compensated by the gain $g(\omega)$

$$R_1 R_2 \exp\left(2Lg(\omega)\right) = 1. \tag{3.4}$$

In this equation, L denotes the traverse length through the active medium. This condition is the threshold gain, which is the starting point for laser operation. For a higher gain, the light field intensity grows as long as a stable population inversion is sustained and until the stimulated emission becomes as strong as the rate by which the electrons are pumped from the ground level to the excited level. The reflectivity of one mirror is typically close to unity (*high reflector*), while the other one's reflectivity is significantly lower (*output coupler*). In this case, the output power of the laser is approximately proportional to the lightfield intensity inside the resonator times the reflectivity of the output coupler.

However, the pump cannot be an external lightfield of photons resonant with the laser transition, because once $N_1 = N_2$ is reached, the pump itself would cause stimulated emission. Obviously, additional electronic levels are required. For most lasers nowadays, four electronic transitions are used like sketched in Fig. 3.1 (a): the ground state $|0\rangle$, the highly excited state $|3\rangle$, the top and bottom laser level $|2\rangle$ and $|1\rangle$, respectively, which mark the laser transition. The pump excites electrons from $|0\rangle$ to $|3\rangle$, from where a fast non-radiative decay to $|2\rangle$ takes place, such that $N_3 \approx 0$. The stimulated emission leads to the radiative decay from the top laser level $|2\rangle$ to $|1\rangle$. A fast non-radiative decay channel from $|1\rangle$ to $|0\rangle$ justifies the approximation of $N_1 \approx 0$. Due to the empty bottom laser level, a population inversion can be reached for relatively low pump levels.

Fig. 3.1 (b) depicts a typical input-output curve that shows the dependence of the laser output power on the excitation power. It can be divided into two different regimes. For low pump powers, no population inversion can be reached because the spontaneous emission is faster than the rate by which electrons are excited. The laser output power is a linear function of the pump power. Since the spontaneous emission is an undirected process, only a small fraction of the emitted photons is funneled into the resonator mode. This ratio depends on the geometry of the resonator and is labeled β-factor. Once the pump power is high enough to reach the threshold limit, the stimulated emission process starts to dominate. For high pump rates, spontaneous emission can be neglected and almost all photons are guided into the coherent light field. The dependence of pump power and laser output is still linear, but now with a much steeper slope. Fig. 3.1 (b) sketches a typical input-output curve (mind the double logarithmic plot: the steeper linear slopes leads to a higher y-offset).

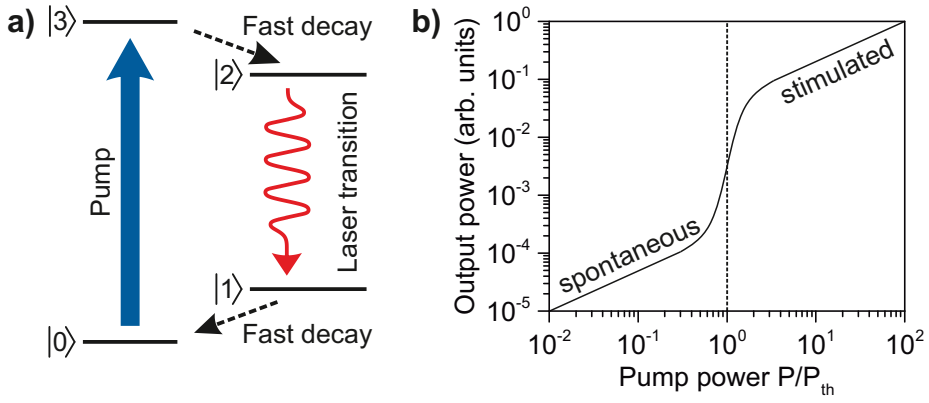

Figure 3.1: Sketch of the pumping mechanism in a four-level laser: Panel (a): Scheme of the four electronic levels involved in the laser process. The external pump is off-resonant from the laser photon energy not to induce stimulated emission by itself. Panel (b): Double logarithmic sketch of a typical input-output curve. Before the laser threshold P_{th} is reached, the laser operates in the spontaneous emission regime. Once the threshold is crossed, the intensity is guided into the resonator mode and a jump in the emission intensity is observed.

In a VCSEL with a typical size of only a few micrometers, all of the three laser components are nanometer-sized structures. How these are realized in the studied samples will be detailed in the following section.

3.2 Laser components in VCSELs

This section will present how the different laser constituents are realized for various types of VCSELs. It will start with a description of two different resonator geometries (microcavities and micropillar resonators), continue with a short review of the employed heterostructures serving as the gain material (quantum wells and quantum dots) and close with a discussion of the different pump mechanisms (electrical and optical pumping).

3.2.1 Microcavities and Micropillar Resonators

In the most basic design, VCSELs are planar layered structures. These are usually grown by **m**olecular **b**eam **e**pitaxy (MBE) on substrates along high symmetry crystallographic axes (e.g. the [100]-direction) [42]. If different crystalline materials with a similar lattice constant are grown on top of each other, heterostructures with high quality, i.e. low internal strain and few lattice dislocations, can be fabricated. The reflectors of VCSELS are periodic stacks of alternating layers made of two materials with similar lattice

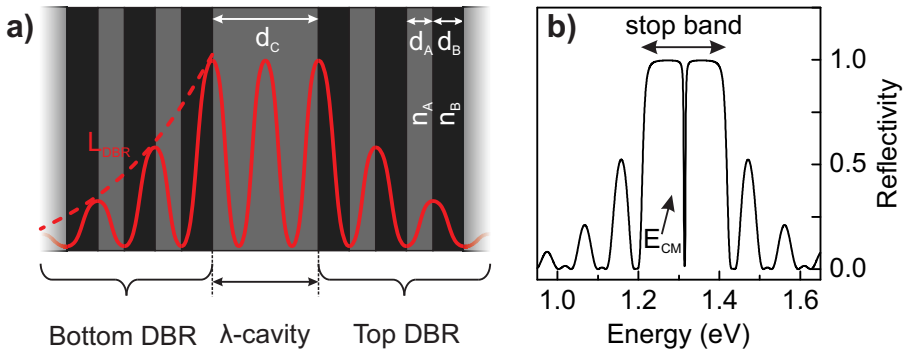

Figure 3.2: Optical microcavity resonator. Panel (a): Sketch of a microcavity layout made of two materials showing the periodic structure of the two DBRs and the sandwiched cavity layer. It hosts a confined light mode (red line) that exponentially decays within the mirrors. For a λ cavity (m=2) and $n_A > n_B$, there is an anti-node in the cavity layer center. Panel (b): Calculated reflectivity spectra for a typical microcavity. Inside the stop band the energy of the resonant light mode E_{CM} appears as a dip.

constants, but different refractive indices. At each layer interface, an incoming light wave is partially transmitted and reflected due to the refractive index mismatch. The layer thicknesses d_i (where i=A,B denotes the two materials) can be chosen such that the reflected parts interfere constructively for a specific wavelength λ_{DBR}. For light of perpendicular incidence this is the case if

$$\lambda_{\mathrm{DBR}} = \frac{d_i}{4n_i} \tag{3.5}$$

is fulfilled. The amplitude of the transmitted wave decays exponentially in the periodic structure and it works as an efficient reflector for photons with that certain wavelength. Since the condition above is the same as the Bragg condition in X-ray analysis, these reflectors are labeled **d**istributed-**B**ragg-**r**eflectors (DBRs). The reflectivity spectrum for arbitrary frequencies can be calculated by the transfer-matrix-formalism (see chapter 8), which reveals that there is a region of high reflectivity centered around λ_{DBR}, called the photonic stop band. Its width is defined by the refractive index contrast.

If two of these DBRs sandwich a cavity layer, a microcavity resonator is obtained. The central cavity spacer acts as a defect layer within the periodic structures surrounding it and can host confined modes if the optical wavelength associated with its thickness falls into the stop band of the reflectors. In order to do so, the cavity layer thickness d_{C} must be given by

$$d_{\mathrm{C}} = \frac{\lambda_{\mathrm{DBR}}}{n_{\mathrm{C}}} \frac{m}{2}, \tag{3.6}$$

with m being an integer. The electric field distribution of the localized mode depends on n_{C}: if the refractive index of the cavity layer is lower or higher than the one of adjacent layers of the two DBRs, the electric field possesses nodes or anti-nodes at the interfaces, respectively. The integer m must be chosen to be uneven in the first, and even in the second case, to obtain a light field maximum in the center of the resonator, which is required for most applications. In the reflectivity spectrum of the microcavity, the photonic resonance is indicated by a dip inside the DBR stop band. Fig. 3.2 sketches the layout of a typical microcavity with a λ-cavity spacer (m=2) and the field distribution of the photonic resonance [cf. Fig. 3.2 (a)], as well as the corresponding reflectivity spectrum [cf. Fig. 3.2 (b)].

The lightfield expands into the mirrors with a penetration length L_{DBR} given by

$$L_{\mathrm{DBR}} = \frac{d_{\mathrm{A}} + d_{\mathrm{B}}}{\ln\left(\frac{n_{\mathrm{A}}}{n_{\mathrm{B}}}\right)}. \tag{3.7}$$

The energy of the resonance of the whole microcavity E_{CM} is not solely determined by the cavity layer thickness, but needs to be corrected for this influence. This corrections becomes the more important, the more the dimensions of the cavity layer and the reflectors are misaligned; i.e. when Eq. 3.6 is only approximately fulfilled. Another quantity, the effective DBR length d_{DBR} is defined

$$d_{\mathrm{DBR}} = \frac{n_A n_B \lambda_{\mathrm{DBR}}}{2\,(n_B - n_A)}, \tag{3.8}$$

which allows to calculate E_{CM} by a weighted mean:

$$E_{\mathrm{CM}} = \frac{d_{\mathrm{C}} E_{\mathrm{C}} + d_{\mathrm{DBR}} E_{\mathrm{DBR}}}{d_{\mathrm{C}} + d_{\mathrm{DBR}}}. \tag{3.9}$$

In the equation above, the energy E_{DBR} and E_{C} correspond to the photon energy associated with λ_{DBR} and the cavity layer thickness, respectively [62]. The width of the microcavity resonance δE_{CM} is determined by the lifetime of the photons. By increasing the number of doublelayers in the DBR, their reflectivity can be enhanced which results in a longer lifetime and a narrower resonance. The Q-factor is defined by the ratio $E_{\mathrm{CM}}/\delta E_{\mathrm{CM}}$ and can reach values of a few 10,000 in high quality resonators. Such high Q factors increase the lifetime of trapped photons to up to several picoseconds. Moreover, one can define the output direction of the laser emission by adding more doublelayers in the bottom mirror close to the substrate compared to the top mirror.

Fig. 3.3 (a) shows **s**canning **e**lectron **m**icroscopy (SEM) images of an AlAs/GaAs microcavity with 23 and 27 doublelayers in the top and bottom mirror, respectively [1]. A λ-cavity GaAs spacer is sandwiched in between [see Fig. 3.3 (b)], which provides for this material composition a light field distribution with an anti-node in the center of the cavity.

[1] The images were recorded in the group of Christian Schneider from the University of Würzburg

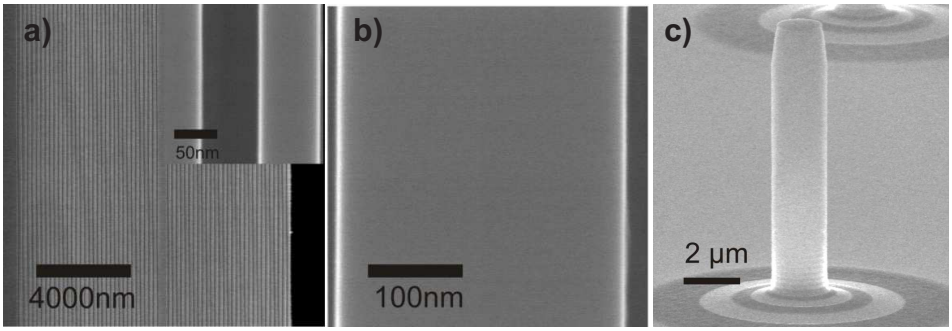

Figure 3.3: SEM images of microresonators. Panel (a): Planar microcavity made from AlAs and GaAs layers with 27 and 23 doublelayers in the bottom and top DBR. The inset shows a close up of a DBR doublelayer. Panel (b): Central λ-cavity spacer of the microcavity. Panel (c): Micropillars with a variable diameter are obtained from such planar structures by an etching process.

A micropillar resonator is depicted in Fig. 3.3 (c), which was fabricated from the initially planar structures shown in the other panels. The main advantage of micropillars compared to microcavities is the larger confinement of the light field not only by the DBRs in the growth direction, but in all three dimensions due to the pillar geometry. This geometry is obtained by the following procedure [95]: subsequent to the MBE growth, the planar structure is spin-coated with an electron-beam-sensitive resist. Into this resist, the pattern for the micropillar cross sections (usually with a circular area) is written by electron-beam-lithography with nanometer resolution. Afterwards the resist is developed and removed from the future positions of the micropillars. Then, a Nickel mask is deposited on top. The remaining resist covering the areas, which are supposed to be etched away, is then removed in a lift-off process, which also takes away the Nickel mask. Finally, plasma etching is used to shape the micropillars out of the microcavity. Note that the thickness of the Nickel mask has to be carefully adjusted such that it is completely etched away and a clear top surface of the micropillar is obtained.

The optical resonances E_{MP} in micropillars are blueshifted relative to the optical resonances E_{CM} of planar microcavities. In micropillars with a circular cross-section, the optical resonances E_{MP} are given by

$$E_{\mathrm{MP}} = \sqrt{E_{\mathrm{CM}}^2 + \frac{h^2 c^2}{\epsilon} \frac{x_{n_\varphi, n_R}^2}{R^2}}, \tag{3.10}$$

where x_{n_φ, n_r} is the n_r-th zero of the Bessel function $J_{n_\varphi}(x/R)$. Since this blueshift is owed to the additional light field confinement, it scales inversely with the micropillar radius R. The field distributions of these modes are described by the microcavity eigenmodes in the growth direction and in the perpendicular plane by Bessel functions of

the first kind. Consequently, the ground mode possesses an anti-node in the center of the micropillar and vanishes at the edges. However, one has to guarantee a sufficient sidewall quality during the etching process, because the scattering of photons at sidewall imperfections may become the dominant loss contribution and limit the total Q factor, especially for thin micropillar resonators [95].

3.2.2 Quantum Wells and Quantum Dots

Semiconductor heterostructures serve as the gain material in VCSELs. They are placed at the light field anti-nodes of the photonic modes supported by the microcavity and micropillar resonators, i.e. in the center of the cavity layer [cf. Fig. 3.2 (a)]. These heterostructures are composed of two semiconductors with a different band gap energy and allow to trap excited electrons and holes in a potential minimum.

Quantum **w**ells (QWs) are planar structures and consist of a layer with a thickness d_{QW} smaller than the electron's de-Broglie wavelength. This layer is made from material A and sandwiched by two barriers made from a different material B, like shown in Fig. 3.4 (a). When the band gap of the quantum well layer E_{G}^{A} is smaller than the one of the barriers E_{G}^{B}, the structure serves as a finite potential well in the growth direction. Electrons and holes can be trapped in a series of confined localized states, with confinement energies E_n^{QW} that can be approximated by considering an infinitely deep potential well

$$E_n^{\mathrm{QW}} = \frac{\hbar^2}{2m^*}\frac{\pi^2}{d_{\mathrm{QW}}^2}n^2, \tag{3.11}$$

where m^* is the effective mass of the electron or the hole. If both an electron and a hole are trapped in a QW, they may recombine and emit a photon with an energy, which is given by the sum of the band gap and the confinement energies corresponding to the electron's and hole's quantum well state. Since QWs are planar structures, the motion in the plane perpendicular to the growth direction is not constrained and the electrons and holes can be treated as free particles along these dimensions. QWs are grown lattice-matched by MBE and in the case of VCSELs are inserted during the growth of the cavity layer.

In contrast, **q**uantum **d**ots (QDs) provide a full three dimensional quantum confinement, which results in a discrete spectrum of electronic states. A QD is a small island of a semiconductor, which is completely encapsulated by a second semiconductor with a higher band gap energy. These heterostructures are grown with MBE by the Stranski-Krastanov method: single atomic monolayers of the semiconductor, from which the QDs shall be formed, are deposited on a substrate with a different lattice constant. The substrate's lattice constant is forced upon the to-be-QD material, which results in a high internal strain. After the growth of a few atomic monolayers called the wetting layer, the internal strain prevents further grow. Instead, the strain energy is minimized by

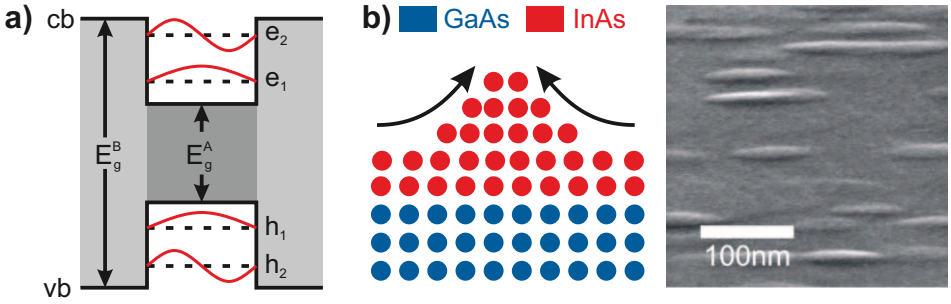

Figure 3.4: Semiconductor QW and QD heterostructures. Panel (a): Scheme of a QW made from semiconductor A (shaded in dark gray) sandwiched by barriers made from semiconductor B (shaded in light gray). Due to the different band gaps E_g, excited electrons and holes are trapped by the QW in discrete confined states, whose wave functions are illustrated by the red curves. Panel (b): Sketch of the growth of InAs QDs on a GaAs substrate (left). InAs QDs emerge as islands from the wetting layer. On a SEM image of InGaAs QDs deposited on a GaAs substrate, elongated QDs with different shapes and sizes are identified (right).

forming small islands on top of the wetting layer, which are the QDs [cf. Fig. 3.4 (b)]. The QDs can be annealed by elevating the temperature to heal out crystal defects and facilitate regular shapes. Finally, the QDs are capped again. Note that islands do not form for arbitrary material pairs with a lattice constant mismatch, but in many material systems only undesired effects like lattice dislocations occur. Most widely used nowadays is the AlAs/GaAs/InAs material system, which will also be investigated in this thesis. The electronic states in these 3D-confined structures are determined by the shape and the size of the QDs; usually the confinement in the growth direction is the strongest and allows for only one electronic state, while a radially symmetric and harmonic potential is assumed for the lateral dimensions [93]. From this consideration, one obtains electronic eigenstates with equidistant energies, which are referred to as the QD shells and numbered s,p,d,... according to the convention for atomic orbitals. However, QDs are actually often not radially symmetric, but for example elongated like presented in the SEM image in Fig. 3.4 (b). Here, one can also see that the shape and the size of the individual QDs differ, which translates into an inhomogeneous broadening of the transition energies of the QD ensemble.

Both types of heterostructures offer advantages, which make them suitable for different applications: QWs, on the one hand, can host many charge carriers due to the continuous density of states for the two non-confined dimensions. Therefore, QWs provide a large optical gain and a high light-matter-interaction, making them attractive candidates to reach the strong light-matter-coupling regime [113]. New physical phenomena can be observed in this regime, e.g. polariton lasing, which is basically coherent light emission

from a Bose-Einstein-Condensate and fundamentally different from conventional lasing [40, 25]. QDs, on the other hand, only support a few electronic states and a population inversion can be achieved for relatively low excitation densities [96]. Besides lasing, micropillars containing a single QD offer the possibility to produce entangled or single photons [59, 41].

3.2.3 Electrical and Optical Pumping

In order to sustain a stable population inversion during lasing, energy needs to be supplied to the semiconductor heterostructures in the form of excited electrons and holes. This can either be achieved by optical or electrical excitation.

Optical excitation is the easiest way to transfer energy into the system: a pump laser is incident on the VCSEL and generates electron-hole pairs via interband absorption. This can be done by resonant optical excitation, i.e. the photon energy of the pump laser is chosen to match an optically allowed transition of the active medium. Since the wavelength of resonant photons falls per design into the optical stop band of the mirrors, the laser needs to be incident under an angle, such that the wavevector in the growth direction is small enough not to be affected by the DBRs. The optical excitation can also be realized off-resonantly. In this case, the photon energy is high above the band gap and absorbed in various layers of the VCSEL. One very intuitive choice is to tune the wavelength of the photons to the higher energy flank of the optical stop band and into the absorption regime of the cavity layer material. This way, the electrons and holes are generated in the cavity layer adjacent to the semiconductor heterostructures and can efficiently populate the heterostructures.

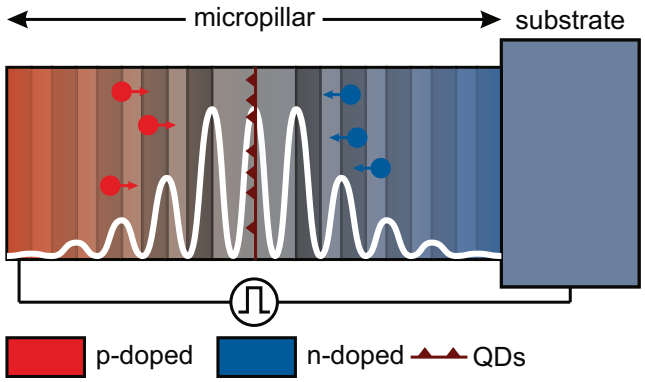

Figure 3.5: Electrically driven micropillar VCSEL with QDs. The n- and p-doping concentration becomes the smaller, the higher the amplitude of the localized photonic mode (white curve) to avoid absorption of the coherent light field. Applying a voltage makes charge carriers move into the QDs in the central intrinsic region and generate light on recombination.

For practical applications, VCSELs are usually electrically driven, which requires some further processing but allows one to operate the VCSEL without external pump lasers. Moreover, in many applications like optical telecommunication, VCSEL are used to convert electronic into optical signals. In Fig. 3.5 the layout of an electrically pumped micropillar laser with QDs is sketched. The laser is turned into a diode by n-doping the substrate and the bottom DBR and p-doping the top DBR. Once a sufficient voltage between the substrate and the micropillar's top facet is applied, the free charge carriers injected by the doping can propagate into the direction of the p-n-junction through the depletion area. Here, they relax into the QD ground state and build up the laser light field on recombination. The generated photons can however be absorbed by the dopants, which introduces a new loss mechanism and leads to a broader laser linewidth and a less efficient pump mechanism. Optical absorption and electrical resistivity have to be carefully balanced against each other. The result is a doping concentration, which is gradually reduced from the outer layers of the microcavity towards the cavity layer in the center, where the lightfield is localized.

In this part of the thesis, various types of VCSELs will be subjected to experiments with picosecond ultrasonics. The impact of the presented gain materials, resonator geometries and pumping mechanisms on the possibility to modulate the emission intensity and wavelength will be examined in detail. Chapter 4 provides a comprehensive overview of the interaction mechanisms of the acoustic pulse with the *active medium* of a VCSEL as a starting point of the analysis. Based on these interaction mechanisms, a theoretical model will be developed to describe the emission intensity dynamics of a microcavity laser with QDs, which are shaken by a picosecond acoustic pulse. Afterwards, the validity of the theoretical model will be tested for a broad range of experimental conditions by comparing simulations with experimental findings. Chapter 5 discusses the influence of the *resonator* on the laser emission modulation. Microcavities can not only host localized photonic modes but also phononic modes. The first category relies on a contrasting refractive index in the DBR layers, while the second category is caused by a mismatch of the acoustic impedance. Phononic eigenmodes shall be exploited to enhance the interaction of the acoustic pulse with the VCSEL. Finally, optically and electrically excited micropillar lasers will be examined in chapter 6 to clarify the role of the *pump mechanism* for the lasing modulation by picosecond ultrasonics.

Chapter 4

Picosecond Control of a Planar Quantum Dot Laser by Coherent Phonons

The performance of VCSELs depends crucially on the spectral overlap of the photonic mode supported by the resonator with the electronic transitions of the active medium. This overlap is usually arranged per design of the heterostructures and ensured by the high accuracy of the MBE growth.

Here, an approach to dynamically change a VCSEL's emission is presented that does not rely on a direct modulation of the pump excitation like in commercially used lasers. Instead, the modulation shall be achieved by a control of the laser's efficiency via the spectral overlap. In this chapter, this control is realized by manipulations of the active medium. Previous work has shown the possibility for a fine-tuning of the active medium with respect to the cavity mode by varying the temperature and applying electric and magnetic fields. All of these methods however suffer from drawbacks in terms of speed and efficiency of the emission modulation: changing the temperature is usually a slow process and applying even strong electric [86] or magnetic fields [98] induces only small energetic shifts compared to the linewidth of most laser gain materials. Picosecond ultrasonics are a promising new tool for a fast and efficient modulation of the detuning between gain material and resonator. Recently, an enhancement of the lasing emission of a VCSEL on an ultrafast timescale by a factor of up to two orders of magnitude was demonstrated. This occurs, when a picosecond acoustic pulse passes through the active medium, which suggests that this enhancement is mostly due to a modulation of the gain material rather than to a shift of the photonic mode [19].

This chapter is dedicated to a study of the impact of acoustic pulses on the active medium and shall clarify to what extent the laser emission intensity can be modified this way. The studied VCSEL is identical to the one used in the initial demonstration

in Ref. [19], i.e. a planar optically excited microcavity laser with an ensemble of QDs as the active medium. Although the behavior of the system for an adiabatically varying detuning is rather intuitive on a qualitative level - decreasing the detuning will result in a better performance and consequently increase the emission intensity and vice-versa -, picosecond acoustic pulses contain high-frequency phonons and transient effects may play an important role. So far, the transient contribution to the overall emission response was not figured out, which is one of the key questions that this chapter shall tackle.

The chapter is structured as follows: the first section briefly reviews how straining a semiconductor heterostructure modifies the electronic levels and examines how this affects the lasing process. Subsequently, a semiclassical model is developed for a microscopic description of the laser under influence of the acoustic pulse. The model shall properly account for the dependence on (i) the initial detuning between the QD ensemble and the cavity mode and (ii) the optical excitation levels with respect to the laser threshold. An experimental setup to measure the laser response under varying conditions for these two quantities is presented in section 4.2. With the help of the model and the setup, simulations and experimental findings are compared to validate the theoretical approach. These results are presented and discussed in section 4.3 at the end of this chapter. Most of the presented results were published in Ref. [34]. The model was developed and the simulations were performed by Daniel Wigger from the University of Münster.

4.1 Semiclassical Laser Model

Mechanical deformations of a semiconductor heterostructure alter the energies of the electronic transitions. In a bulk semiconductor, the energy shift is related to the applied strain and is composed of a uniaxial and a shear contribution, which are associated with the diagonal and off-diagonal elements of the strain tensor η, respectively. Since in the experiments performed here, only uniaxial strain in one direction is assumed (cf. chapter 2), the second contribution will be neglected for simplicity. In a first-order approximation, one can assign an individual deformation potential constant a_i for each electronic band denoted by i that linearly links the energy shift to the applied strain η. In the case of zink blende semiconductors like AlAs/GaAs/InAs studied here, the light-hole and heavy-hole valence bands are degenerate at the Γ point. The net change of the band gap ΔE_G at the Γ point is described by

$$\Delta E_\mathrm{G} = (a_\mathrm{c} - a_\mathrm{v})\eta = a\eta. \tag{4.1}$$

Here, a_v accounts for the valence band that is shifted closer to the conduction band and a is the net band gap deformation potential (it will be only called deformation potential from here on). For most semiconductors, a is on the order of -10 eV [100], which results in shifts of 10 meV induced by the typically employed strain amplitudes of about 10^{-3}. The

acoustic pulse also alters the size of heterostructures and thereby modulates the confined electronic states. The shift of the confinement energies can also be linked to the applied strain by another deformation potential constant. However, a short calculation based on Eq. 3.11 shows that this constant is on the order of the confinement energy itself, which is usually a few tens of meV here, and therefore much smaller than the bulk deformation constant. The effect is therefore neglected in the following.

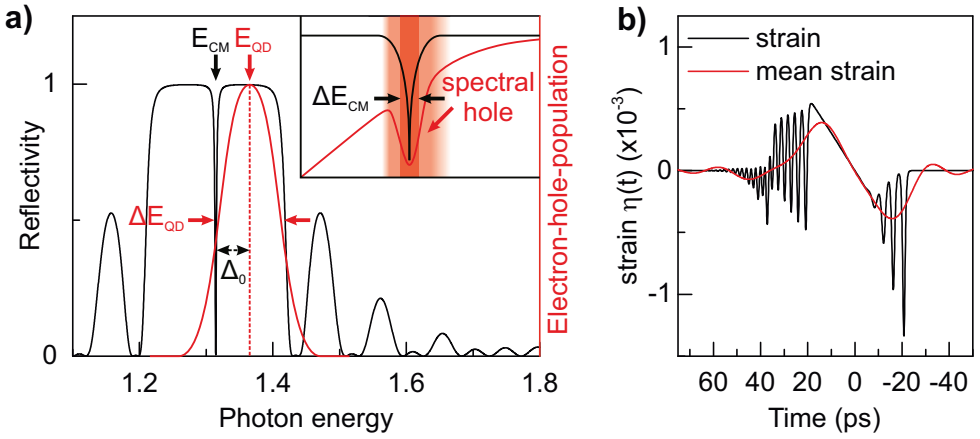

Figure 4.1: Interaction of the acoustic pulse with the QD laser. Panel (a): optical reflectivity of the microcavity resonator (black) and electron-hole population density of the QD ensemble (red). Cavity mode and active medium are detuned. The inset shows the spectral hole, which is burned into the electron-hole population density due to lasing. Panel (b): example of a calculated strain pulse profile $\eta(t)$ featuring high nonlinear characteristics (black curve). Applying a low pass filter with a cutoff frequency of 50 GHz, given by the approximate lifetime of electron-holes in the lasing regime, indicates the slowly-varying mean applied strain (red curve).

Fig. 4.1 illustrates how the lasing efficiency is affected by spectral shifts of the optical gain material. Fig. 4.1 (a) sketches the properties of a VCSEL with a microcavity and an ensemble of QDs. The black curve shows the optical reflectivity of the resonator and features the broad stop band with a near unity reflectivity. Inside, the cavity mode appears as a dip at E_{CM} with a FWHM of ΔE_{CM}. The electron-hole population density of the inhomogeneously broadened QD ensemble is sketched in red by the Gaussian profile centered at E_{QD} with a width of ΔE_{QD}. If the initial detuning Δ_0 between the cavity mode and the ensemble is non-zero, the laser is not working optimally. But even if this detuning is vanishing, only a small fraction of the QDs can contribute to the lasing process, because the resonator's width ΔE_{CM} is significantly smaller than the width of the QD ensemble ΔE_{QD}. The inset in Fig. 4.1 (a) elucidates this situation: the QDs in resonance with the cavity mode contribute to the lasing process and the

lifetime of excited electrons is reduced to due to stimulated emission to somewhat below ∼10 ps. Therefore, a spectral hole emerges in the electron-hole-population density with a position and a width determined by the the cavity mode, while the QDs in its vicinity form a highly excited energy reservoir unavailable for the laser. In the following, two mechanisms responsible for the modulation of the laser emission will be discussed. These mechanisms occur on two different timescales separated by the intrinsic timescale of the system, namely the lifetime of the electrons in the spectral hole, which is usually a few picoseconds [53].

Fig. 4.1 (b) shows the calculated strain profile $\eta(t)$ of an acoustic pulse featuring strong non-linear characteristics as a black curve (cf. chapter 2). It contains high frequency phonons resulting in fast oscillations, which can be seen in particular in the trailing part of the acoustic pulse for 20 ps$< t <$60 ps. Moreover, three pronounced solitons precede the main part of the acoustic pulse and appear around t=-15 ps. Applying a low pass (red curve) with a cut-off frequency given by the lifetime of the electrons under lasing shows that the acoustic pulse also exerts a slowly-varying strain evolving slower than the intrinsic timescale. This slowly-varying mean strain in turn leads to a mean spectral shift of the QD ensemble, which result in an *adiabatic* response, i.e. the laser emission intensity will adiabatically follow the number of resonant QDs from among the ensemble. If the QD ensemble and the cavity mode are initially non-resonant, the acoustic pulse may, on the one hand, overcome the detuning and enhance the laser emission. On the other hand, the mean applied strain may as well shift the QD ensemble further away from the cavity mode and make the laser less efficient.

Coherent oscillations with a shorter period than the intrinsic timescale of the lasing system lead to the transient *shaking* effect: when the QD ensemble is rapidly shaken, the highly excited QDs on both sides of the spectral hole are dynamically coupled to the resonator mode. The energy stored in them is fed into the light field, which one might think of as an artificial broadening of the spectral hole. This transient *shaking* effect will increase the number of QDs contributing to the lasing, even if the mean applied strain is zero.

Fig. 4.2 shows the theoretical model to describe the laser under influence of applied strain including the two presented mechanisms. On the right side the QD ensemble is sketched, which is treated as a two level system, with an electron ground state $|G\rangle$ and an excited state $|X\rangle$. Due to the inhomogeneous broadening of the ensemble, the transition energies are modeled by a Gaussian distribution centered at E_{QD} with a FWHM of ΔE_{QD}. The QDs are closely spaced, such that an continuous distribution $n(E)$ is assumed. An additional state $|Y\rangle$ is introduced, which represents the wetting layer and is used to model the pumping dynamics. A rate equation model for each QD transition energy E is employed. The pump level is populated from the ground state by a variable pumping rate γ_{p} ($|G\rangle \rightarrow |Y\rangle$). From this excited state, a relaxation into the upper QD state with a rate γ_{r} ($|Y\rangle \rightarrow |X\rangle$) occurs, which is often referred to as the QD

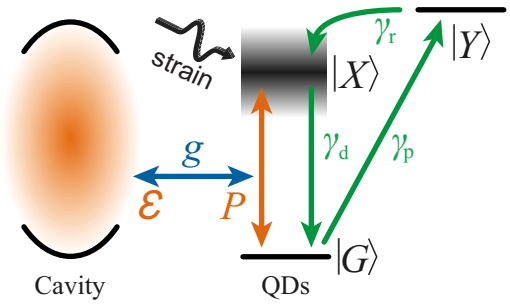

Figure 4.2: Semiclassical laser model. The QDs are described by a rate equation model involving three electronic levels. A polarization builds up in inverted QDs whose coupling to the cavity light field is described in a semiclassical way.

capture rate. Excited electrons decay into the electronic ground state via spontaneous decay with a rate γ_d ($|X\rangle \to |G\rangle$), or by stimulated emission.

The light-matter-interaction is described by a semiclassical model in the rotating wave and slowly varying amplitude approximation. Every QD is coupled with a constant coupling strength g to the internal laser light field $\mathcal{E}$ with a photon energy of E_CM. The light field intensity is initially given by white noise. Once the pump is switched on and the QDs become inverted, a polarization P_E between the ground and the excited state builds up. The strength of the polarization depends on the total population inversion and on the detuning $\Delta_E = E_\mathrm{CM} - E$ of the considered transition energy with respect to the cavity mode; it is the stronger, the smaller the detuning. The polarization is lost due to the longitudinal dephasing contributions of pump and decay. Moreover, a transversal term is added, which is accounted for by a pure dephasing rate γ [24].

The rate equations for the population densities of the QD levels denoted by G_E, X_E, and Y_E as well as for the microscopic polarization P_E of the QDs fully read

$$\frac{\mathrm{d}}{\mathrm{dt}} P_E = -\frac{1}{2}\left(\gamma_\mathrm{d} + \gamma_\mathrm{p} + 2\gamma\right) P_E + i\frac{\Delta_E}{\hbar} P_E + ig\mathcal{E}\left(X_E - G_E\right) \tag{4.2}$$

$$\frac{\mathrm{d}}{\mathrm{dt}} G_E = -\gamma_\mathrm{p} G_E + \gamma_\mathrm{d} X_E - i\left(g^*\mathcal{E}^* P_E - g\mathcal{E} P_E^*\right) \tag{4.3}$$

$$\frac{\mathrm{d}}{\mathrm{dt}} X_E = -\gamma_\mathrm{d} X_E + \gamma_\mathrm{r} Y_E + i\left(g^*\mathcal{E}^* P_E - g\mathcal{E} P_E^*\right) \tag{4.4}$$

$$\frac{\mathrm{d}}{\mathrm{dt}} Y_E = -\gamma_\mathrm{r} Y_E + \gamma_\mathrm{p} G_E. \tag{4.5}$$

For the time evolution of the cavity light field $\mathcal{E}$ the finite reflectivity of the resonator (associated with the spectral width of the cavity mode) needs to be included by a leaking rate γ_l and one obtains

$$\frac{\mathrm{d}\mathcal{E}}{\mathrm{d}t} = -\gamma_\mathrm{l}\mathcal{E} - ig^* \int n(E) p_E(t)\,\mathrm{d}E, \tag{4.6}$$

where $\mathcal{E}(t)$ and $P_E(t)$ are in a frame rotating with the frequency corresponding to the cavity mode [53]. One can see that the strength of the light field depends on the QD ensemble distribution, the population inversion, and the detuning.

The acoustic pulse is introduced as a perturbation into the system. The interaction of the QDs with the coherent phonons leads to a change of the transition energy and the detuning becomes time-dependent $\Delta_E(t) = E_{\mathrm{CM}} - [E + a\eta(t)]$. The deformation potential constant for the InGaAs QDs is set to a=-10 eV [66]. To make the simulations comparable with experimental results, the light emission from the laser is finally time-averaged over a cosine-squared time window with a FWHM of 25 ps. This corresponds to the finite time resolution of the employed experimental setup, which will be detailed along with the investigated VCSEL in the next section.

4.2 Planar Microcavity QD Laser and Experimental Setup

The sample was grown on a (100)-orientated GaAs substrate that was polished down to a thickness of 100 µm. On its backside, a 100 nm thin Al film is deposited and utilized for the generation of picosecond acoustic pulses. The resonator of the VCSEL located on the front side of the substrate is a planar microcavity. Its DBRs consist of alternating $\lambda/4$ layers made from AlAs and GaAs with a thickness of 79 nm and 67 nm, respectively, such that the central stop band wavelength lies in the near-infrared at about 940 nm. In the top and bottom DBR there are 23 and 27 doublelayers, respectively, which makes the top DBR the output coupler of the laser. A λ-cavity layer made from GaAs with a nominal thickness of 268 nm is sandwiched in between the two mirrors. Since the sample has a slight wedge shape, the thickness of the cavity layer varies for different spots on the sample and the optical resonance can be chosen from between 1.33 eV-1.37 eV. The linewidth of the cavity mode is deduced from reflectivity measurements and found to be 1.2 meV.

A thin sheet of $In_{0.3}Ga_{0.7}As$ QDs with a density of 10^{10} cm^{-2} serves as the gain material of the laser. It is located at the light field anti-node of the optical resonance in the center of the cavity spacer. The photoluminescence (PL) spectra of the QD ensemble is shown in Fig. 4.3 (a) as a black curve. It was recorded by the authors of Ref. [19] from the sample side, where the microcavity does not affect the optical properties, at a temperature of about 10 K. The center of the the Gaussian distribution is at E_{QD}=1351 meV with a FWHM of 11 meV. This is about ten times larger than the width of the resonator mode [cf. the spectrum of the lasing emission recorded from the sample front in Fig. 4.3 (red curve)]. The coupling of the cavity mode and the ensemble as a whole is therefore rather weak. Independent from the energetic detuning between cavity mode and QD ensemble, only a small fraction of the QDs contribute to the lasing process.

The photoluminescence was also recorded spectrally integrated and time-resolved to

determine the electron lifetime both in the spontaneous and stimulated emission regime. Fig. 4.3 (b) shows the temporal evolution of the photoluminescence after pulsed optical excitation. If the optical excitation does not exceed the laser threshold (black curve), a decay constant of about $\tau_{\text{spont.}}$=1.6 ns is found, which is drastically reduced to only $\tau_{\text{stim.}}$=22 ps, when the lasing regime is reached (red curve).

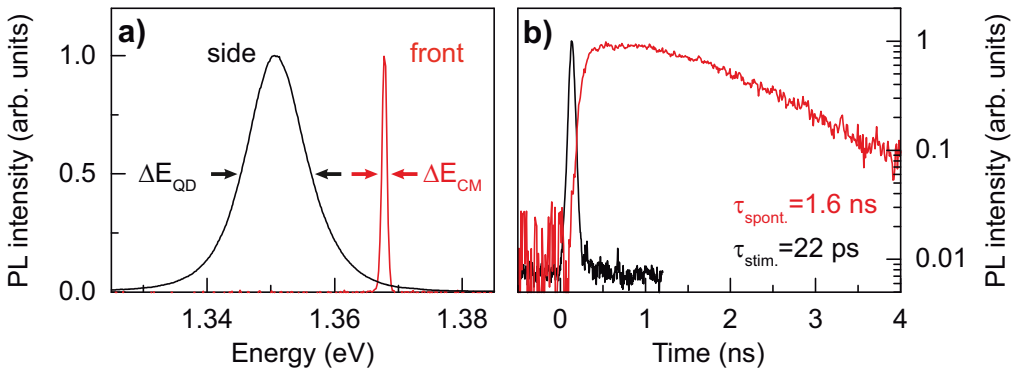

Figure 4.3: Photoluminescence of the VCSEL. Panel (a): PL spectra recorded from the side showing the bare QD ensemble (black curve) and laser emission recorded from the front (red curve). Panel (b): Time resolved measurements of the curves shown in panel (a) after pulsed optical excitation. The decay constant is drastically reduced when the lasing regime is reached.

An overview of the experimental setup used to measure the impact of a picosecond acoustic pulse on a VCSEL is plotted in Fig. 4.4 (a). Like detailed in chapter 2, the acoustic pulse is generated optically by an amplified laser system. The seed laser is a mode locked Ti:Sapphire laser emitting a train of pulses with a duration of 150 fs, a central wavelength of 800 nm, and a repetition rate of 80 MHz. Since the energy per pulse is on the order of ∼10 nJ, reaching the necessary optical excitation densities of ∼10 mJ/cm^2 for a strain amplitude of 10^{-3} would require very tight optical focusing to a few micrometers. To avoid such narrow spots, the pulses of the seed laser are amplified by a regenerative amplifier (Coherent: RegA) by three orders of magnitude at the cost of a lower repetition rate. The RegA emits slightly chirped amplified pulses with a duration of 200 fs, a repetition rate of 100 kHz, and an energy per pulse of ∼10 µJ. This beam is loosely focused to a spot size with a diameter of about 150 µm onto the backside of the sample. Here, an aluminum film is deposited to serve as an opto-mechanical transducer, which is depicted in the close-up in Fig. 4.4 (b). The acoustic pulse is launched at this position and propagates through the substrate towards the VCSEL located on the sample's front side.

The QDs are optically pumped by a second laser. This excitation laser is a frequency-doubled ND:YAG laser emitting pulses with a duration of 23 ns, a central wavelength

of 532 nm and a repetition rate controlled by an internal Q-Switch that is synchronized with the RegA. The excitation photon energy is high above the band gaps of AlAs and GaAs and the power can be adjusted with a gray filter. Both the traversal time of the acoustic pulse through the microcavity as well as the lifetime of electron-hole pairs are considerably smaller than the duration of the laser pulse, such that the excitation can be considered as quasi-continuous. The excitation laser is tightly focused onto the front DBR to a spot with a diameter of 25 µm and incident under an angle. Thereby its reflection from the sample surface is spatially separated from the laser emission.

The VCSEL's emission is collected with an angular aperture of about 2° and afterwards forwarded to a streak camera. Therein, the laser emission is first converted by a photocathode into a stream of electrons. This electron beam passes through a pair of sweep electrodes in order to be deflected. A sawtooth voltage is applied to the sweep electrodes such that the deflection distance becomes time-dependent and can be translated back into the arrival time of the primary photons at the photocathode. Afterwards, the stream of electrons is re-converted into photons by a phosphorous screen, which are finally detected by a CCD. The bias applied to the sweep electrodes has to be synchronized with the RegA pulses via an electrical delay generator. The employed electronics offer a maximum time resolution of 25 ps. The experiments are conducted at cryogenic temperatures to avoid strong phonon-damping during the substrate passage. Therefore, the sample is placed inside a bath cryostat in a helium atmosphere, whose temperature can be set from room temperature down to the boiling point of liquid helium at 4.2 K.

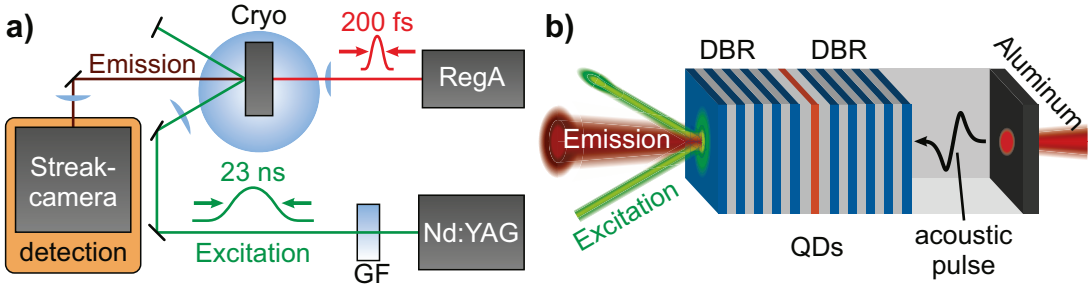

Figure 4.4: Experimental setup. Panel (a): Overview of the setup: a ND:YAG laser optically excites the VCSEL with a power adjustable by a gray filter (GF). The VCSEL is placed in a cryostat and its emission is recorded by a streak camera. The acoustic pulse is generated by a regenerative amplifier (RegA). Panel (b): Close-up of the sample: the acoustic pulse is launched at the backside and propagates towards the microcavity on the front.

4.3 Measured and Simulated Laser Emission Intensity

In this section the emission modulation of the presented VCSEL is experimentally measured and the results are compared with numerical calculations. To prove the validity of the developed model, the experiments are performed for a large variety of experimental conditions. By choosing different sample spots with different cavity modes, the initial detuning $\Delta_0 = E_{\mathrm{CM}} - E_{\mathrm{QD}}$ between the QD ensemble and the cavity mode can be selected. Three scenarios are studied: a large negative and positive detuning as well as an almost resonant case [1]. Moreover, the laser emission modulation is recorded for two different optical excitation levels for each detuning. Since the model does not properly account for spontaneous emission, both excitation levels are chosen above the laser threshold.

4.3.1 Positive Detuning: Δ_0=14 meV

In Fig. 4.5 the findings for a large positive detuning of Δ_0=14 meV are presented. First, the calculated evolution of the strain field $\eta(t)$ at the QD layer is discussed, before moving on to the results of the actual phonon-laser interaction. The simulations are performed as follows: in a first step, the amplitude and the width of the Gaussian displacement pulse are determined from the optical excitation density and the optical absorption length of aluminum. Afterwards, the Korteweg-de-Vries equation is numerically solved for this input to describe the non-linear propagation through the substrate. Subsequently, the acoustic pulse is injected into the microcavity itself and moves onwards to the QD layer. The propagation through the multilayered DBRs is handled by a transfer-matrix and scattering states approach, like detailed in chapter 8. The final result of this procedure for an optical excitation density of 10 mJ/cm^2, a non-linear propagation through the 100 µm GaAs substrate, and the studied microcavity structure is shown in Fig. 4.5 (a). One can clearly distinguish between two distinct acoustic pulses passing the QD layer: the acoustic pulse coming from the substrate side reaches the central cavity layer at a time of $t \approx 0$ ps. In the following, this acoustic pulse will be referred to as the *incident* acoustic pulse. After passing the QD layer, the acoustic pulse propagates further towards the front facet of the VCSEL, where it gets reflected and is directed back into the sample. The *reflected* acoustic pulse hits the QD layer at $t \approx 1350$ ps. This temporal difference is given by twice the transit time through the top DBR. Upon the reflection at the open surface, the sign of the strain field is also flipped, which can be seen in the insets. In the time interval between the passage of the two main pulses, one can see small persisting oscillations that stay inside the cavity. The origin of these long-lived vibrations is related to acoustic resonances of the microcavity. The discussion of these resonances is however postponed to the next chapter, where they will play the central role.

[1] Please note that not every spot on the sample is of good quality. Therefore, experiments could only be performed for an almost (and not exactly) resonant case and for a positive and a negative detuning with a slightly different absolute value.

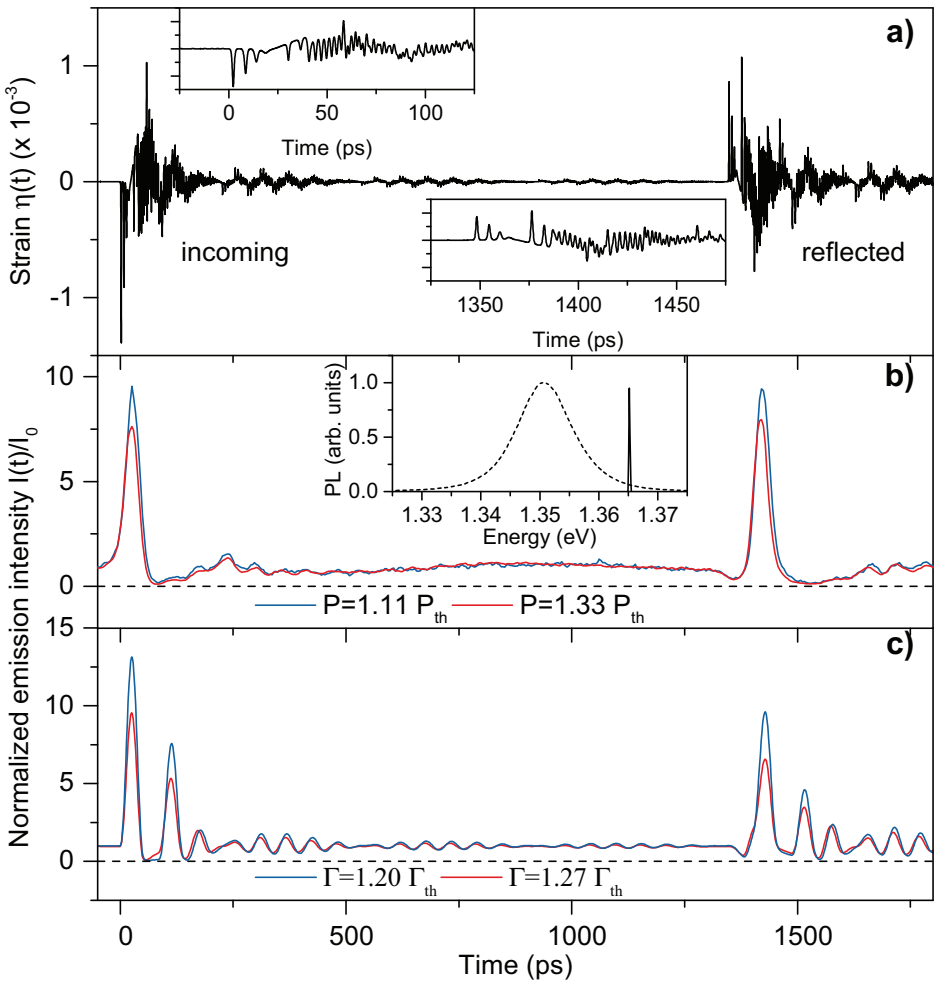

Figure 4.5: Laser emission modulation for an initial positive detuning of Δ_0=14 meV. Panel (a): Calculated strain evolution at the QD layer, showing the incoming pulse at $t\approx$0 ps and the reflected pulse about 1350 ps later in the insets. Panel (b): Experimentally recorded laser modulation. The inset shows the spectral positions of the QD ensemble (dashed line) and the cavity mode (solid line). Panel (c): Simulation of the laser emission intensity.

Fig. 4.5 (b) shows the laser intensity modulation starting when the incident acoustic pulse reaches the QD layer at t=0 ps. The momentary intensity $I(t)$ is normalized to the intensity of the unperturbed laser I_0 to obtain the relative emission change. Two optical excitation levels have been studied. These are in the following always expressed in relation to the particular laser threshold for the considered detuning in order to make the excitation conditions in the experiment and the model comparable. The experimental

and theoretical excitation rate is denoted by P and Γ, respectively.

Each transit of the acoustic pulse leads to a significant modulation of the laser emission intensity for both studied excitation densities. The modulation starts with a huge enhancement in the case of the incident pulse. The reason for this amplification is that the leading compressive part of the strain pulse ($\eta < 0$) blueshifts the QD ensemble and brings it closer to resonance with the cavity mode. Please notice the inset in Fig. 4.5 (b) that depicts the spectral positions of the QD ensemble (dashed curve) and the cavity mode (solid curve). The assumed maximum exerted blueshift is about 10 meV, which overcomes the initial detuning of 14 meV in a large part and the emission modulation is consequently quite efficient. An almost tenfold increase of the laser emission during a time window of 50 ps can be seen here. The following part of dominantly tensile strain ($\eta > 0$) redshifts the QD ensemble in the opposite direction and a quenching is observed. The laser emission drops to almost zero.

After the complete passage of the incident acoustic pulse, the emission shows lasting harmonic oscillations, which are the counterparts of the long-lived vibrations also found in the strain profile $\eta(t)$ for 200 ps$< t <$500 ps. Due to the flipped sign, the reflected acoustic pulse leads to the opposite sequence and first a quenching is observed, followed by a large amplification. Another interesting aspect is the dependence on the optical excitation: a larger amplification is found closer to the laser threshold. From a qualitative point of view this is quite clear: in the transition area from the spontaneous to the stimulated emission, the input-output curve is highly non-linear [cf. Fig. 3.1] and the system is very sensitive to perturbations.

Now the results of calculations based on the semiclassical model are compared with the experimental data. To this end, a set of values for the various quantities like transition energies and rates, coupling strengths, etc. have to be found, which are adopted from the experiment if available. This is the case for: the spectral position E_{QD}=1351 meV and the width ΔE_{QD}=11 meV of the QD ensemble; the cavity loss rate that can be deduced from the cavity mode's linewidth and is found to be γ_l=0.4 ps^{-1}; and for the cavity mode, whose spectral position is different for each studied detuning. The other quantities are experimentally not easy of access and are set to values, which yield the best agreement with the experiment and are in accordance with established theoretical models [24, 23]. The values are set to g=2.8 ps^{-1}, γ_{r}=0.5 ps^{-1}, γ_{d}=0.03 ps^{-1}, and γ=1 ps^{-1}. The laser threshold in the simulations is governed by the spontaneous decay rate γ_{d}, such that it is useful to consider this as an offset and look at a corrected pump rate $\Gamma = \gamma_{\mathrm{p}} - \gamma_{\mathrm{d}}$.

Most of the features of the experimental curve are well reproduced. The two large peaks and the quenching associated with the incident and reflected pulse can be identified and also the small oscillations occurring after each transit are found. Moreover, the enhancement is slightly larger in the simulations when the excitation is closer to the threshold like it is observed in the experiment. However, even for the parameters giving

the best agreement, some deviations remain. The most noticeable difference is the amplitude of the subsequent peaks following the two leading ones, which are pronounced in the simulation but quite faint in the experiment. Moreover, the maximum enhancement is larger in the simulations (factor of ∼13) than in the experiment (factor of ∼10). These deviations are most probably due to the simplified assumptions made in the theoretical treatment: the modeled three-level system for the QDs does not include multi-excitonic effects and does not properly capture the relaxation mechanism of highly excited, hot carriers into the QDs . No damping of phonons is considered in the simulations for the acoustic pulse, which becomes the more important, the higher the phonon frequencies are. All these neglected effects will likely broaden and blur the peaks in the experiment. Please also note that the best agreement is not achieved when the pump excitation P and Γ are set to the same value with respect to the laser threshold for experiment and simulations, respectively. The different choice is related to the different input-output curves in the simulations and the experiment. This issue is addressed at the end of this chapter.

4.3.2 Negative Detuning: Δ_0=-18 meV

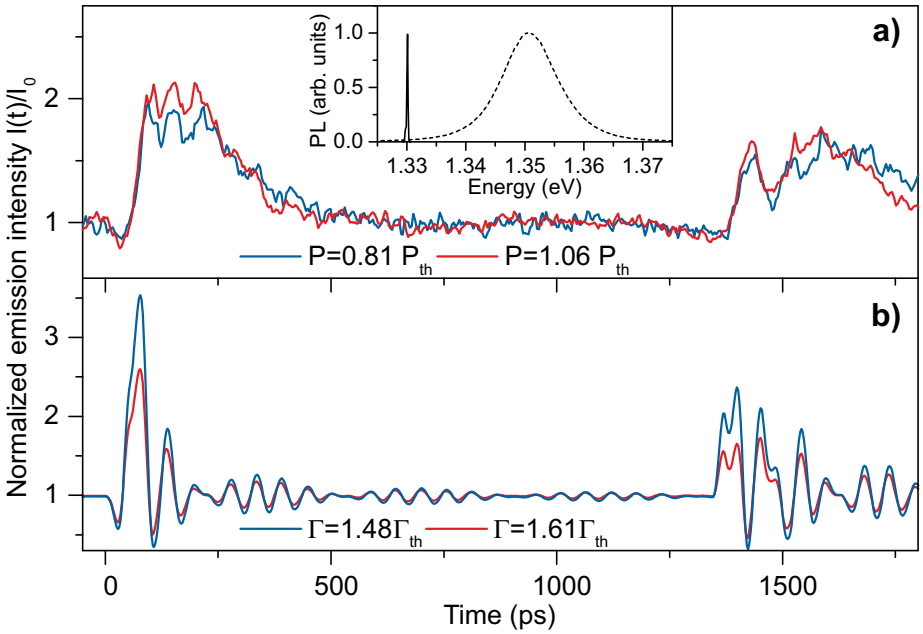

Figure 4.6: Laser emission modulation for an initial negative detuning of Δ_0=-18 meV. Panel (a): Experimentally recorded laser modulation. The inset shows the spectral positions of the QD ensemble (dashed line) and the cavity mode (solid line). Panel (b): Simulation of the laser emission intensity.

If the initial detuning is chosen to be negative and even larger, Δ_0=-18 meV, the results presented in Fig. 4.6 are obtained. Fig. 4.6 (a) shows the experimental curves for this situation and the inset depicts the spectral position of the cavity mode in relation to the QD ensemble. One can see that the cavity mode barely overlaps with the QDs and is located on the outer flank of the distribution. Even for highest optical excitation densities close to damaging the sample, the laser emission is rather weak and a larger noise level is observed in the experiment [cf. the input-output curve in Fig. 4.9 (a)]. The response to the acoustic pulse looks different for this configuration. Two broad peaks at t=0 ps for the incident and at t =∼1350 ps for the reflected acoustic are observed. The emission intensity is doubled only, which is a considerably smaller amplification than found in the previously discussed case of Δ_0=14 meV. Obviously, the number of QDs contributing to the lasing is not increased as significantly as before. This is explained by the larger absolute value of Δ_0 rather than by the opposite sign: the maximum shift of the QD ensemble of about 10 meV can now overcome a smaller part of the initial detuning and additionally, the QD ensemble distribution is flatter at the position of the cavity mode [cf. the insets in Fig. 4.5 (b) and Fig. 4.6 (a)]. The different sign of the detuning still has a minor effect. When looking at the strain profile of the incident and reflected acoustic pulse in detail [see Fig. 4.5 (a)], one can see that the maximum compressive strain (the leading part of the incident pulse at t∼0 ps) is larger than its counterpart of maximum tensile strain (the leading part of the reflected pulse at t∼1350 ps). The acoustic pulse therefore induces higher maximum blueshifts to the QD ensemble and is more capable of compensating positive detunings. The flipped sign of the detuning also leads to an inverted sequence of amplification and quenching: the incoming acoustic pulse starts with a compressive part that blueshifts the QD ensemble, pushing it even further away from the cavity. Consequently, the modulation begins with a slight quenching and only afterwards an enhancement is found.

The simulations reproduce these observations. The sequence of amplification and quenching for the two passages of the acoustic pulse through the QD layer is properly displayed. The calculations also find that the amplification is significantly smaller than in the previous case and predict an enhancement factor of ∼3 for the incident and ∼2 for the reflected pulse. Such an asymmetry is also found in the experiment.

4.3.3 Almost Resonant Case: Δ_0=1.5 meV

The last experimentally studied scenario is an almost resonant case with a small positive detuning of Δ_0=1.5 meV. Fig. 4.7 (a) depicts the recorded curve. Like in the case of a large positive detuning, the modulation begins with a sharp peak. However, since for a smaller initial detuning the laser already works relatively efficient, the enhancement only reaches a factor of about 5. Following the peak, a pronounced quenching and subsequent sizable harmonic oscillations are observed. While the sequence of amplification and quenching is reversed as expected, a striking asymmetry between the incident and the

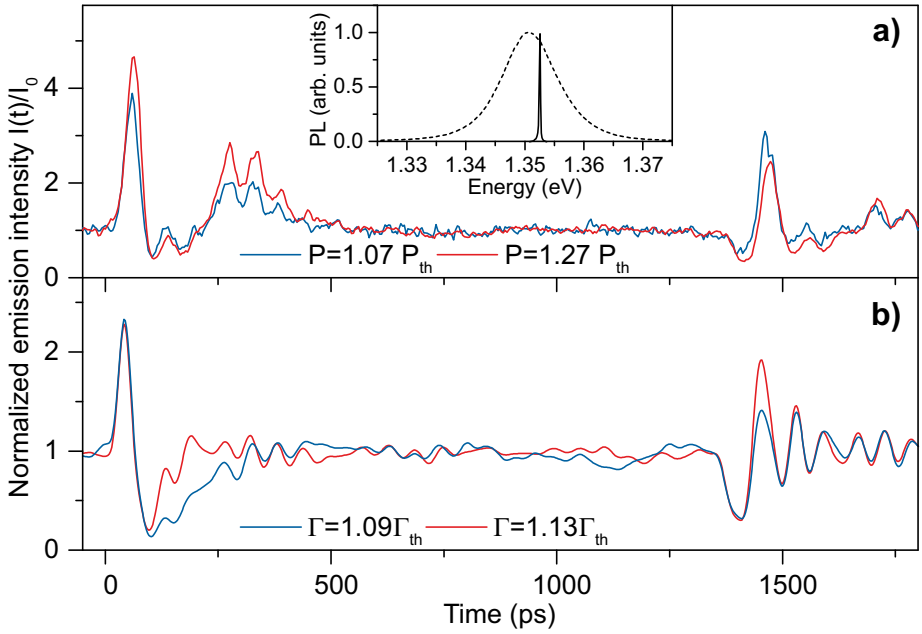

Figure 4.7: Same as Fig. 4.6, but for an initial small positive detuning of 1.5 meV in the experiment and 3.0 meV in the simulations.

reflected acoustic pulse is found: the maximum enhancement in the reflected pulse is approximately halved. The calculations shown in Fig. 4.7 (b) are performed for a slightly larger detuning of Δ_0=3 meV. If chosen this way, the several peaks, the quenching, the harmonic oscillations, and the asymmetry is properly simulated. The adjustment of the detuning in the simulations is in particular required to reproduce the quenching of the laser emission; it will be shown below that if the detuning approaches zero, no quenching will remain anymore.

4.3.4 Vanishing Detuning: Δ_0=0 meV

The studied scenarios show that the developed model captures the most important features of the emission modulation due to shifts of the active medium under various experimental conditions. But if one brings the two different laser modulation mechanisms back to mind - the *adiabatic* response and the transient *shaking effect* introduced in the beginning of this chapter - one has to assess that so far no insight about their role has been obtained. Both mechanisms work simultaneously in the studied scenarios. It is impossible to separate their relative contribution in order to evaluate which one is dominant, or, in the case of the shaking effect, whether it is significant at all. To finally answer this question, the model is employed for a scenario making this distinction possible, namely for a vanishing initial detuning. Here, the QD ensemble is already in perfect

resonance and the mean applied strain can only increase the detuning. Consequently, the adiabatic response will always induce a drop of the emission, while the transient shaking effect is expected to amplify the emission intensity.

Fig. 4.8 presents the results for this situation. The two transits of the acoustic pulse are identified by the two main peaks. During almost the entire passage, the net emission intensity is positive, especially when the fast oscillatory parts of the incident and reflected pulse hit the QD layer at 40 ps$< t <$100 ps and 1380 ps$< t <$1440 ps, respectively [cf. Fig. 4.5 (a)]. The shaking effect clearly exceeds the adiabatic contribution. The analysis shows that transient effects are important and have to be accounted for in the theoretical treatment for the emission modulation by coherent phonons.

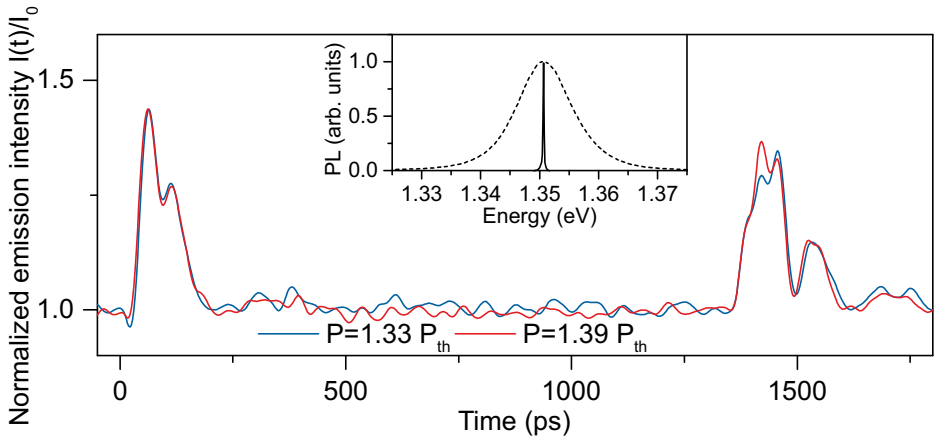

Figure 4.8: Simulation of the laser emission intensity for a vanishing initial detuning.

4.3.5 Evaluation of the Developed Model

The presented comparison between experiment and simulations shows that the theoretical treatment is capable of predicting the laser emission response to a very good degree. The complex interaction of electrons, photons, and phonons is captured well by the rather basic semiclassical laser model. Its simplicity is, on the one hand, an advantage: the model is transparent, easy to handle and implement, and flexibly adjustable to the experimental conditions. On the other hand, the laser model suffers from one intrinsic drawback, which is the description of the spontaneous emission in the semiclassical approach.

Before reaching the lasing threshold, the light field intensity is described by white noise, i.e. it does not depend on the excitation. In reality, it is given by the fraction of the spontaneous emission from excited states being guided into the resonator (given by the β-factor), which obviously depends on the excitation level. The imperfect treatment of the pre-lasing regime in the model becomes obvious, when comparing the measured

and calculated input-output curves, shown in Fig. 4.9. While the most important features are identical, for example the lower laser threshold for smaller detunings, there are also some deviations. In the experiment, the laser threshold is defined as the first kink when the output exceeds the spontaneous emission. The threshold region itself is extended and there is a smooth and broad transition from the spontaneous into the stimulated emission regime during which the input-output curve is highly non-linear. In contrast, the curve in the simulations is essentially flat before the lasing threshold is crossed and afterwards a steep step is found. This makes predictions of the interaction with the acoustic pulse below the threshold impossible. Moreover, the steep slope of the simulated curve might predict a too high modulation amplitude. If one wants to adapt the simulations to the experiment in this regard, one would need to go to a fully quantum-mechanical light description to properly account for the spontaneous decay [23]. However, this is a challenging task when phonons are also included. As a simple alternative, the excitation in experiment and simulations is here not set to the same value relative to the threshold, but instead chosen such that best agreement is achieved.

The developed model can be used to study conditions that are hard to realize experimentally but promise to provide a profound insight into the system. One example is a rectangular (or generally absolutely flat) QD ensemble distribution. This is experimentally hard to achieve, but would eliminate all adiabatic contributions to solely study the shaking effect. Moreover, one can apply tailored strain shapes, e.g. harmonic oscillations with a given frequency, to study the frequency response of the emission modulation. Such studies have recently been performed by the developers of the model from the University of Münster and can be found in Ref. [134]. In the future, it might be interesting to use the model for the purpose of finding the strain profile necessary to achieve a desired laser modulation.

In this section, the possibility to modulate the lasing emission of a VCSEL with picosecond ultrasonics via the active medium was discussed. Two contributions were identified, which are associated with different properties of the QD ensemble that serves as the gain material: the spectral *detuning* with respect to the resonator yield an adiabatic contribution, which may result in a quenching or an amplification, depending on the initial detuning and the applied strain. The *inhomogenous* broadening moreover offers an additional route to increase the lasing emission by shaking. The two mechanism led to an efficient laser modulation. Remarkable amplitudes of almost complete quenchings and up to tenfold enhancements on a picosecond timescale were demonstrated.

In the following chapter, a set of *homogenously* broadened QWs will be employed as the active medium and only the adiabatic response needs to be considered. Under these simplified conditions, the interaction between strain and lasing is easier to handle and the focus of the study will be laid on the resonator. If the resonator supports mechanical eigenmodes and confines them to the same space as the active medium, their interaction might be enhanced. This was already indicated above in the observation of long lasting

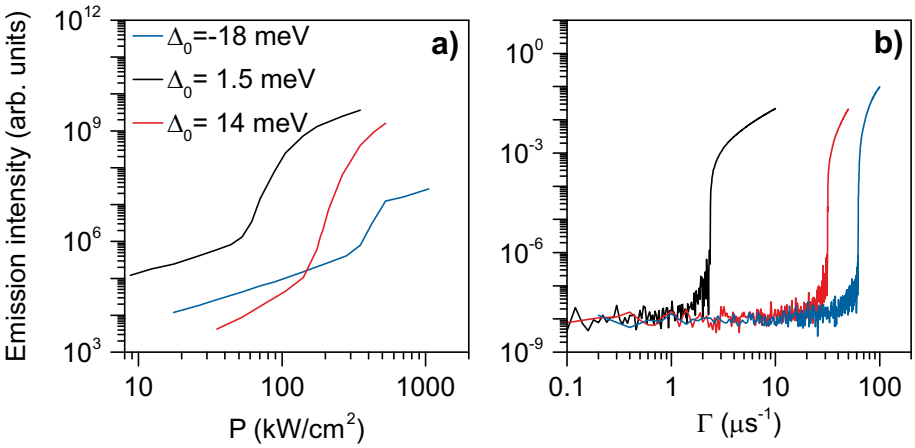

Figure 4.9: Input-output curves. Panel (a): Experimentally measured curves for the three studied detunings. Panel (b): The simulated curves possess a steeper slope owing to the semiclassical nature of the model.

intensity oscillations, which persist after the transit of the incident and the reflected acoustic pulse. The next chapter will highlight the origin of these mechanical resonances and elucidate if they can be exploited for an even longer laser emission modulation than observed in this chapter.

Chapter 5

Lasing from Active Optomechanical Resonators

Optomechanical resonators simultaneously host resonances with long lifetimes for phonons and photons and confine them to the same space. The interaction of these two fundamental excitations of the system is mediated by radiation pressure: imagine an optomechanical system formed from an optical Fabry-Perot cavity, with one semi-transparent coupler mirror and one high-reflector, which is mounted on a spring. If a light field generated by an external optical pump is guided into the cavity through the coupler mirror, photons will start to bounce between the two ends of the cavity. The radiation pressure exerted in each reflection process gives rise to a force that will not affect the fixed coupler mirror, but it will displace the moveable high-reflector from its equilibrium position (known as optical spring effect). This displacement is translated into a shift of the optical resonance, which then in turn yields a back-action onto the light field, e.g. via the coupling efficiency of the pump into the Fabry-Perot cavity [9]. Such a system is able to perform self-sustaining oscillations and can be exploited for a vast number of interesting novel phenomena. If the pump laser is redshifted with respect to the cavity mode by one fundamental phonon energy, each photon that is guided into the cavity annihilates one phonon. This effect is called laser-cooling and allows one to remove so many phonons from the system that the mechanical motion is cooled down to the quantum ground state [5, 126]. Other interesting effects are the coherent transfer of energy from radiation into long-lived mechanical motion [74], optomechanically induced transparency [132], and ultra-sensitive mass detectors with up to yocta-gramm (10^{-28} g) resolution [121]. The latter is based on the idea that single atoms, biological molecules, etc. change the vibrational properties of the optomechanical resonator when they are adsorbed, which is optically detectable due to the high photon-phonon interaction.

Practical realization of optomechanical systems often rely on small micrometer-sized objects, which trap light inside due to total reflections at the surface. Such objects are

for example microdiscs [121] or conical nanorods [89] that possesses various mechanical resonances like breathing, extensional, or flexural modes due to their geometric shapes. The frequencies of these acoustic modes are determined by the dimensions of the total object and are usually in the MHz regime. For the ultrafast modulation of light, higher frequencies need to be exploited that must arise from finer structuring. One very intuitive choice for nanometer-structured devices are DBRs: if not only the refractive index but also the acoustic impedance of the two constituting materials contrast, DBRs can serve as acoustic mirrors, too. A microcavity formed by two dual *photon-phonon-DBRs* facing each other becomes an optomechanical resonator. A recent publication demonstrates that near-infrared light and GHz vibrations are indeed successfully confined in an AlAs/GaAs microcavity. The interaction of photon and phonon is manifold enhanced, which was evaluated by Raman-scattering experiments[44].

By embedding an optically active medium into a dual microcavity, an active optomechanical resonator is obtained. Such a system works as a laser with optical and acoustic resonances. Here, their interplay is investigated with respect to its potential for an ultrafast laser emission modulation. Most of the results were published in Ref. [30]. As a starting point of this chapter, the origin and the properties of the different kinds of vibrational eigenmodes hosted by microcavities will be discussed. In the following section, the investigated VCSEL is shortly characterized. Moreover, the experimental setup is presented, which allows to measure the laser emission after vibrational eigenmodes have been launched. The results are presented and analyzed afterwards in the last section.

5.1 Optomechanical Resonators

Periodic layered structures like DBRs can serve as reflectors for phonons of a specific wavelength. Generally, DBRs do not work as efficient acoustic mirrors, unless a *necessary* and a *sufficient* condition are fulfilled. The first one demands the acoustic impedance of the two materials the reflector is composed of to mismatch; this is necessary to make acoustic reflections at interfaces occur and is the basic prerequisite for the interference-based reflection principle of DBRs. Consider a DBR consisting of alternating layers made from material A and B with thicknesses of d_A and d_B, respectively. Phonons with a wavevector q_m given by

$$2q_m = mG_0 \tag{5.1}$$

fulfill the Bragg-conditions and are reflected back from the structure. In this equation, m is an integer and $G_0 = 2\pi/(d_\mathrm{A} + d_\mathrm{B}) = 2\pi/D$ is the reciprocal superlattice vector. Phonons with these wavevectors cannot propagate through the structure and consequently gaps appear in the dispersion at the corresponding frequencies f_m at

$$f_m = \frac{m}{2\left(\frac{d_\mathrm{A}}{v_\mathrm{A}} + \frac{d_\mathrm{B}}{v_\mathrm{B}}\right)}, \tag{5.2}$$

where v denotes the sound velocity in the respective material. The dispersion is folded back at the edges of the Brillouin-zone [cf. Fig. 5.1 (b)], where the zone-edge stop bands can be found ($q = \pi/D$, $m = 1, 2, 3, \ldots$) and also at the center of the Brillouin-zone, where the the zone-center stop bands are located ($q = 0$, $m = 2, 4, 6, \ldots$). The width of these gaps are determined, on the one hand, by the contrast of the acoustic impedances and, on the other hand, by the layer thicknesses. This regards the *sufficient* conditions for an efficient phonon mirror: to maximize the width of the gaps, which is also a direct measure for the acoustic reflectivity of the corresponding stop band, the ratio between the layer thicknesses has to be carefully chosen. It has to match $d_\mathrm{A}/v_\mathrm{A} = d_\mathrm{B}/v_\mathrm{B}$ and $d_\mathrm{A}/v_\mathrm{A} = d_\mathrm{B}/3v_\mathrm{B}$ for optimum zone edge and zone center stop bands, respectively [129]. If one of the two conditions is met and one class of stop bands is optimized, the frequency gaps of the other class will completely vanish and the reflectivity will drop to zero. Both kinds of stop bands will emerge in intermediate cases, but often with a rather poor reflectivity [1].

Unfortunately, the primary purpose of the DBRs is to serve as optical mirrors and therefore the layer thicknesses are often predetermined: their optical thickness must be equal to a quarter of the optical wavelength [cf. Eq. (3.5)]. In order to work as a dual mirrors, the layer thicknesses must simultaneously fulfill [44]

$$\frac{d_\mathrm{A}}{d_\mathrm{B}} = \frac{n_\mathrm{B}}{n_\mathrm{A}} = \frac{v_\mathrm{A}}{v_\mathrm{B}}. \tag{5.3}$$

Finding two materials, where (i) the acoustic impedances are significantly different; (ii) a similar lattice constant allows stacking different layers on top of each other; and (iii) the ratio of the refractive indices is close to the inverse ratio of the sound velocity, is a quite challenging task. The combination is actually so rarely found that it was called a 'double magic coincidence' when first being discovered and exploited in AlAs/GaAs [70]. Microcavities made from these materials automatically serve as optimized resonators for photons and phonons of the same wavelength. As another plus, the contrast of the acoustic impedances and the refractive indices is very similar, such that one needs the same number of doublelayers to achieve both a sufficient optical and acoustical reflectivity.

In Fig. 5.1, calculations for an AlAs/GaAs microcavity with a GaAs λ-cavity layer optimized for zone-edge modes are presented. Fig. 5.1 (a) illustrates the photonic density $|E^2|$ (red curve) and the distribution of the displacement u (blue curve) for the first zone edge cavity modes (m=1). Both distributions are confined in the cavity layer and decay exponentially on a similar length scale inside the DBRs. The internal layer interfaces are indicated by the black line as a guide for the eye. Fig. 5.1 (b) shows the acoustic reflectivity (solid line) and the dispersion (dashed line) close to the first stop band. One

[1] Even in intermediate cases a good reflectivity can be reached anyway by increasing the number of doublelayers.

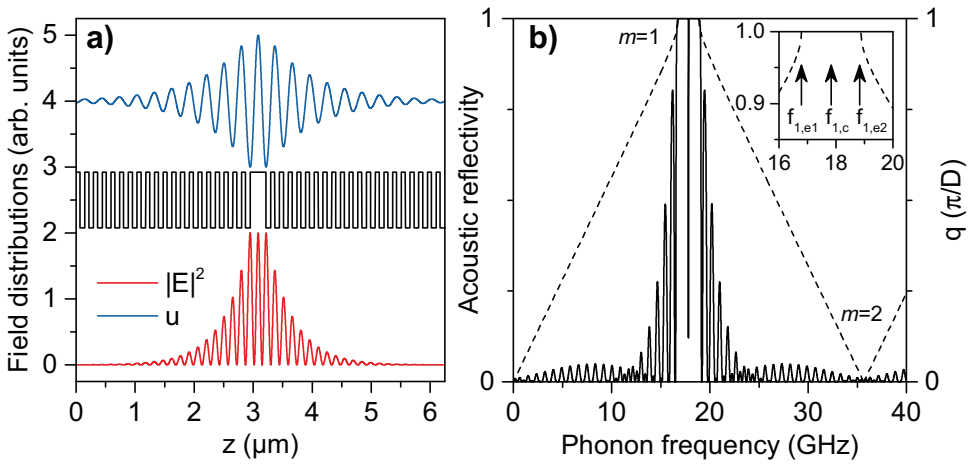

Figure 5.1: Optomechanical microcavity resonator. Panel (a): Electric field (red) and displacement (blue) distribution of the first photonic and phononic cavity modes, respectively. The black curve indicates the layer interfaces. Panel (b): Acoustic reflectivity (solid line) and phonon dispersion (dashed curve) in the microcavity. The inset indicates the three acoustic resonances close to the stop band with arrows.

can identify the broad stop band with a high reflectivity and the dip inside associated with the ground mode plotted in Fig. 5.1 (a). The stop band spans across the same frequencies where gaps occur in the dispersion. However, please note that the first zone-center stop band (m=2) at 35 GHz completely vanishes, since the DBRs are optimized for zone-edge modes. Towards the gap, the dispersion flattens and its derivative approaches zero right at the edges (see section 8.1 for more details about the calculations). Here, the density of states is increased and the group velocity vanishes. Therefore, wave packets with these frequencies will stay in the cavity much longer.

Two types of resonances need to be distinguished: on the one hand, localized *cavity modes* at frequencies $f_{m,\mathrm{c}}$ in the center of the stop bands. These are the standard resonances that are introduced by and confined to the cavity layer. On the other hand, there are long-lived *DBR modes* appearing at the higher and the lower energetic flanks of the stop bands at $f_{m,\mathrm{e1}}$ and $f_{m,\mathrm{e2}}$, respectively. These resonances are not localized, but slowly propagate through the structure due to the reduced group velocity. Arrows indicate the spectral position of the discussed modes in the inset in Fig. 5.1 (b).

Please note that in the center of the cavity spacer, where usually the active medium is located, the displacement field of the acoustic cavity modes possesses an anti-node and the strain - as its spatial derivative - consequently vanishes [cf. the field distribution for u plotted in Fig. 5.1 (a)]. Cavity modes do not strain the center of the cavity and therefore barely interact with an active medium placed there. Therefore, most probably slowly propagating DBR modes rather than the cavity mode are responsible for the long-lived

oscillations observed in the previous chapter.

5.2 Planar Microcavity QW Laser and Experimental Setup

The studied VCSEL consists of a planar microcavity. Its DBRs are made of alternating 58 nm wide $Al_{0.2}Ga_{0.8}As$ and 67 nm wide AlAs layers, corresponding to an optical $\lambda/4$-thickness for a wavelength of 870 nm. The bottom and top DBRs are made from 27 and 23 doublelayers, respectively. A $\lambda/2$-cavity layer made from AlAs is sandwiched in between. The cavity mode is located at about 840 nm and its optical Q-factor is found by micro-photoluminescence to be $\sim 10^4$ at a temperature of 10 K.

Three sets of 12 nm wide GaAs QWs serve as the active medium of the sample. Each set consists of four QWs separated by 4 nm thick AlAs barriers. The first QW group is placed in the center of the cavity, while the other two are located at the light field anti-nodes inside the two innermost DBR layers adjacent to the cavity [cf. the inset in Fig. 5.2 (a)]. In the experiment, the temperature of the sample is varied from 180 K up to room temperature. Recording the QW PL from the side, where the microcavity does not affect the PL, reveals that the lowest order interband transition redshifts from about 1.45 eV (830 nm) at 180 K to 1.49 meV (855 nm) at room temperature. The linewidth increases from 2 meV (1.2 nm) to 12 meV (6.8 nm) in this temperature interval due to thermal broadening. The sample was grown on a (100)-orientated GaAs substrate, which was polished to a thickness of 30 µm. On the backside of the sample, a 100 nm thick aluminum film is deposited in order to generate acoustic pulses. The substrate is chosen to be rather thin to enable experiments at elevated temperatures. This is necessary, since the acoustic attenuation starts to increase above 50 K and especially high-frequency phonons are strongly suppressed [22].

Fig. 5.2 (b) presents the time-resolved pump-probe setup used to measure the impact of the acoustic resonances on the laser emission intensity. The main idea of the setup is to record the laser emission intensity after acoustic resonances have been excited. Amplified laser pulses originating from the RegA (an amplified modelocked Ti:Sapphire laser, see section 4.2) are split up with a ratio of 90/10. The higher intensity beam is guided over a variable linear delay stage onto the aluminum film on the back of the sample. The beam is loosely focused to a spot with a diameter of about 150 µm. In the following, this beam is labeled the pump beam and it is used to generate acoustic pulses. The second beam with lower intensity is labeled the probe-inducer beam. It is guided over a fixed delay with a length such that it arrives at the sample's front surface simultaneously with the acoustic pulse launched at the backside. This beam is focused to a spot with a diameter of about 25 µm and incident under an angle. Its purpose is to optically excite the QWs and trigger the laser emission if the threshold power is exceeded.

After the pulsed optical excitation, the laser will emit a short laser burst with a

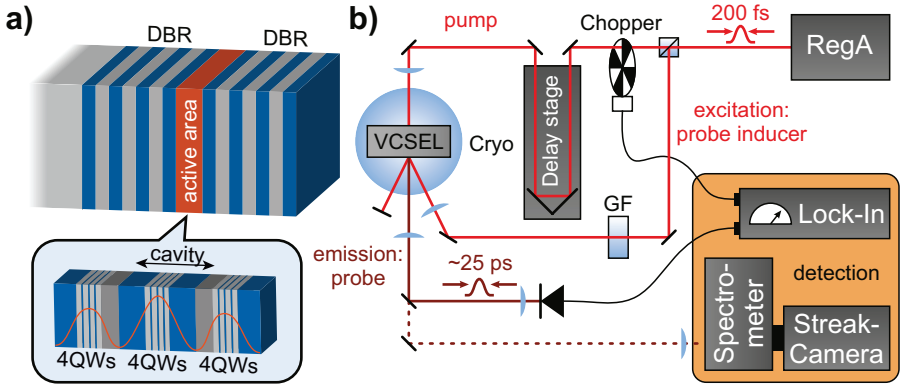

Figure 5.2: Sketch of the studied VCSEL and the experimental setup. Panel (a): Sketch of the VCSEL. The close-up shows the three sets of QWs serving as the laser gain material that are located at the three innermost light field anti-nodes. Panel (b): Experimental pump-probe setup to measure the interaction of acoustic and optical resonances. An amplified laser system (RegA) generates the acoustic pulses on the backside with the pump pulse and optically excites the VCSEL with the probe inducer pulse. The laser emission itself is considered the probe pulse. Each emitted pulse is detected time-integrated by a photodiode.

duration of about 20 ps. The interaction of the VCSEL with the acoustic resonances manifests itself in a modulation of the time-integrated intensity of each emitted laser pulse. The emission is collected with an angular aperture of 2° and forwarded to a photodiode, which measures the time-integrated intensity of the pulsed emission. To increase the sensitivity for intensity changes due to the acoustic pulse, a chopper is placed into the pump beam path and used as a reference for a Lock-In detector, to which also the signal of the photodiode is forwarded. The laser emission burst itself is considered the probe pulse, since its intensity contains the information about the interaction with the acoustic pulse. Its duration of ∼20 ps sets an upper limit to the time resolution of the setup, because the photodiode performs only time-integrated measurements. Therefore, the time resolution is considerably lower than in conventional pump-probe-experiments with femtosecond laser sources.

The emission of the laser can also be analyzed with a second detection comprising a spectrometer and a streak camera. In the spectrometer, the light is focused on and collected from a grating by two parabolic mirrors with a focal length of 50 cm. The grating has a lattice constant of 600 slits/mm, which results in a spectral resolution of 0.1 nm (∼0.17 meV in the near-infrared). The emission can either be recorded with energy and time resolution, if the two devices are used in a series, or with time resolution only, when the spectrometer is bypassed. This is often advantageous, because adding the spectrometer to the detection worsens the time resolution limit of the setup: the time

resolution of the streak-camera alone is 5 ps, while adding the spectrometer increases this limit to about 30 ps [2]. To obtain information about the active media unfiltered by the microcavity, the QW PL can also be collected from the side and then be evaluated by the spectrometer. The sample is placed in a bath cryostat, which allows to vary its temperature from cryogenic temperatures up to room temperature.

5.3 Experimental Results

The modulation of the laser emission due to the interaction with resonant phonons is presented here for two different temperatures. The sample is nominally designed to work at room temperature and can be operated down to temperatures of about 150 K. There is no spectral overlap between the QWs and the cavity mode for lower temperatures anymore, since the QWs are blueshifted more strongly than the cavity mode and their linewidth decreases significantly. In the following, the laser response is discussed for two scenarios: for a temperature of T=180 K, the QWs transitions are narrow and the detuning with respect to the cavity is relatively large; at room temperature, the QW linewidth is broad and the QWs are moreover in resonance with the cavity.

5.3.1 Emission Modulation at 180 K

Fig. 5.3 presents the results for the experiment at a temperature of T=180 K. In the inset in the bottom-right corner the QW PL and the position of the cavity mode for this temperature are indicated; the cavity mode is located at 1.470 eV, while the QWs are blueshifted with respect to the cavity mode at 1.496 eV. Since the linewidth of the QW transition is only 10 meV, the laser works quite inefficient. Nevertheless, the VCSEL is driven into the lasing regime by the probe-inducer and it is pumped at an excitation of about four times the laser threshold power. As a result, it emits short laser probe pulses. These are recorded with the streak camera alone. The inset in the bottom-left corner depicts such an emitted laser pulse. Its total duration comprising the build-up time and the decay is about 17 ps, which is also the time resolution of the pump-probe-setup. The small peak in the beginning is due to the optical excitation by the probe-inducer pulse. For the generation of the acoustic pulse a pump density of about 10 mJ/cm^2 is chosen.

The change of the time-integrated intensity of the pulsed emission $\Delta I(\tau)$ is normalized to the time-integrated intensity in absence of the acoustic pulse I_0. It is measured with the photodiode and presented in the main panel. The delay τ is chosen such that at τ=0 ps the acoustic pulse reaches the set of QWs that is buried in the innermost doublelayer of the bottom DBR. In the curve two distinct peaks can be recognized, one belongs to the incident acoustic pulse at τ=0 ps and one to the reflected pulse at

[2] In the experiments performed here, faster sweeping electronics than in the previous chapter were used.

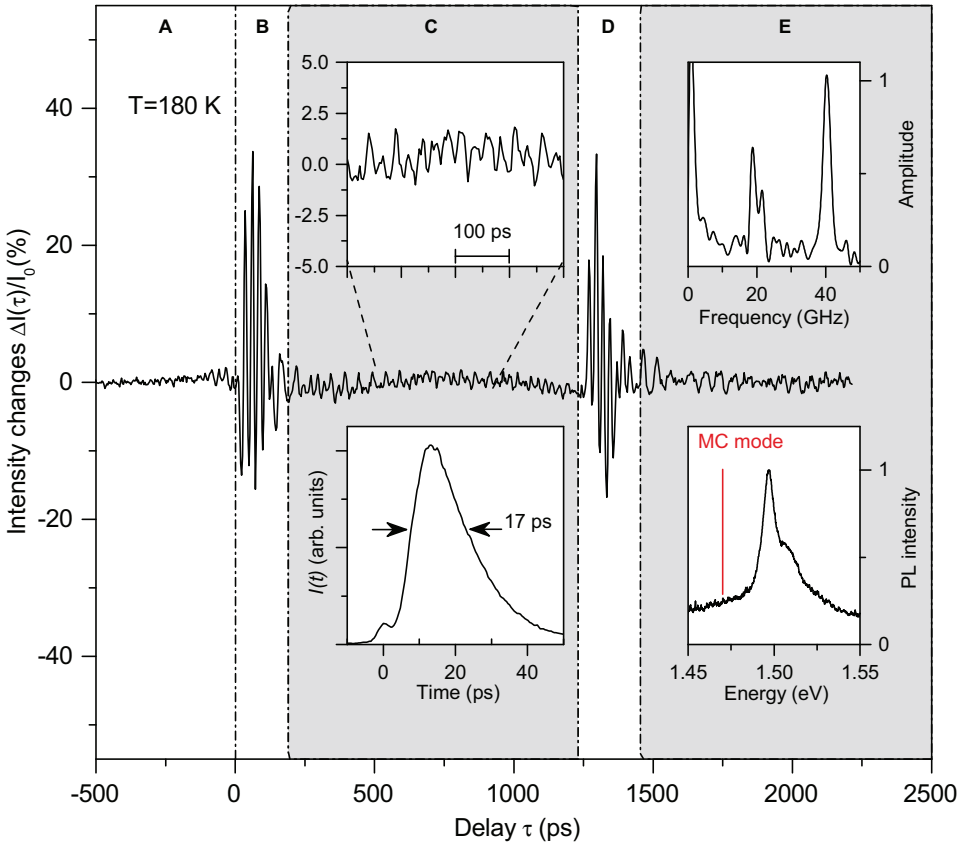

Figure 5.3: Laser emission modulation at a temperature of T=180 K. The main panel shows the pump-probe curve for the time-integrated and normalized laser emission modulation $\Delta I(\tau)/I_0$. The vertical lines divide the different temporal regions A-E. The insets show clockwise starting in the bottom right corner: a close up of the resonant oscillations in region C; their FFT spectrum; the QW PL recorded from the side and the position of the cavity mode; a time-resolved streak camera picture of the VCSEL emission after pulsed optical excitation.

t=1150 ps. Just like in the previous chapter, this temporal difference matches the time it takes the acoustic pulse to propagate from the central cavity region to the top surface of the sample, where its sign is flipped upon reflection, and back again. Each transit causes several peaks, because there are in total twelve QWs, which are distributed across the inner microcavity area. One can divide the pump-probe curve in five areas, which are defined by the position of the acoustic pulse and indicated by vertical lines: for delays τ <0 ps (region A), the acoustic pulse has not reached the QW closest to the substrate yet and no interaction with the gain material occurs; for 0 ps < τ < 180 ps (region B)

the main part of the acoustic pulse is resident in the inner cavity area where the QW sets are located; for 180 ps $< \tau <$ 1150 ps (region C), the acoustic pulse has left the cavity layer and travels back and forth through the top DBR; for 1150 ps $< \tau <$ 1450 ps (region D) the reflected acoustic pulse interacts with the QWs; and for higher delays (region E) the acoustic pulse leaves the microcavity into the direction of the substrate.

The highest modulation occurs in region B and D and reaches amplitudes of about 50 %. However, the interaction with the broadband acoustic pulse itself was extensively discussed in the previous chapter and is not of interest here, but the focus is laid on region C, when the initial acoustic pulse already passed the cavity and long-lived acoustic resonances have been excited. Here, one can see on top of a slightly bent background [3] a modulation with a rather small amplitude of about 2 % of the initial laser intensity (see the inset in the top-left corner). A Fast-Fourier-Transform of the signal in region C is performed to analyze if mechanical resonances are responsible for the observed laser emission modulation. The result is shown in the inset in the top-right corner and features two pronounced peaks. The first peak is actually a double peak centered at about 20 GHz, while the second single peak is located at 40 GHz.

Now these findings are compared with simulations to check if the frequencies belong to any acoustic resonances. To this end, the phonon dispersion in the DBRs is calculated (without including the QW and the barrier layers). The result is shown in Fig. 5.4 (a) and reveals that gaps open up at 20 GHz and 40 GHz; exactly at the frequencies, at which the long-lived modulation observed in the experiment takes place (see the inset in the top-right corner in Fig. 5.3). The open question is still, which kind of acoustic resonance is responsible for the long-lived oscillations, be it either DBR modes associated with slowly propagating phonons or confined cavity modes. The gap at the lower frequency at 20 GHz is the first zone-edge stop band (m=1). It is rather broad and has a width of about 1.9 GHz. The two DBR resonances appear at the lower and the higher energy flank at $f_{1,\mathrm{e1}}$=19.2 GHz and $f_{1,\mathrm{e2}}$=21.1 GHz, respectively. As discussed before in the previous chapter, the 'double magic coincidence' material pair AlAs/GaAs features optimized acoustic zone-edge stop bands for standard optical $\lambda/4$ DBRs. However, since a small amount of Al is added to the GaAs layers, the acoustic properties are slightly altered such that this optimization condition is not matched anymore. As a result, a very narrow zone-center gap (m=2) appears around 40 GHz with a width of only 0.3 GHz. Therefore, the two DBR modes at the flanks of the zone-center stop band $f_{2,\mathrm{e1}}$ and $f_{2,\mathrm{e1}}$ as well as the localized cavity mode $f_{2,\mathrm{c}}$ are spectrally very closely spaced.

The FFT of the emission intensity modulation shows two peaks for the zone-edge resonances at 20 GHz. These peaks appear at the position of the DBR modes at the flanks of the stop band at $f_{1,\mathrm{e1}}$ and $f_{1,\mathrm{e2}}$, respectively. The DBR modes play the dominant role and no peak in the center of the stop band at $f_{1,\mathrm{c}}$, where the confined cavity mode

[3] The background is not flat due to imperfections of the mechanical delay stage

is located, can be found. Since the QWs are distributed across the cavity and most of them are not located at anti-nodes of the strain field associated with the confined cavity mode, this behavior is rather surprising at a first glance. Most probably, the localized modes are suppressed because the acoustic resonances are excited remotely from the outside by the picosecond acoustic pulse. Cavity mode phonons need to be funneled into the microcavity through the narrow dip in the reflectivity. Its width is related to the acoustic Q-factor, which ultimately determines the build-up time of the cavity mode. Calculations show that Q ∼1000, corresponding to a build-up time of about 20 ns. Therefore, cavity mode phonons may play an important role for longer delay times.

Whether slowly propagating DBR modes or the confined cavity mode are responsible for the zone-center peak at 40 GHz, remains unclear. The frequency resolution of the FFT in the experiment is about 1 GHz, because the time window of the FFT has a duration of 1 ns. This resolution is too coarse to resolve the different closely spaced resonances in the narrow zone-center stop band.

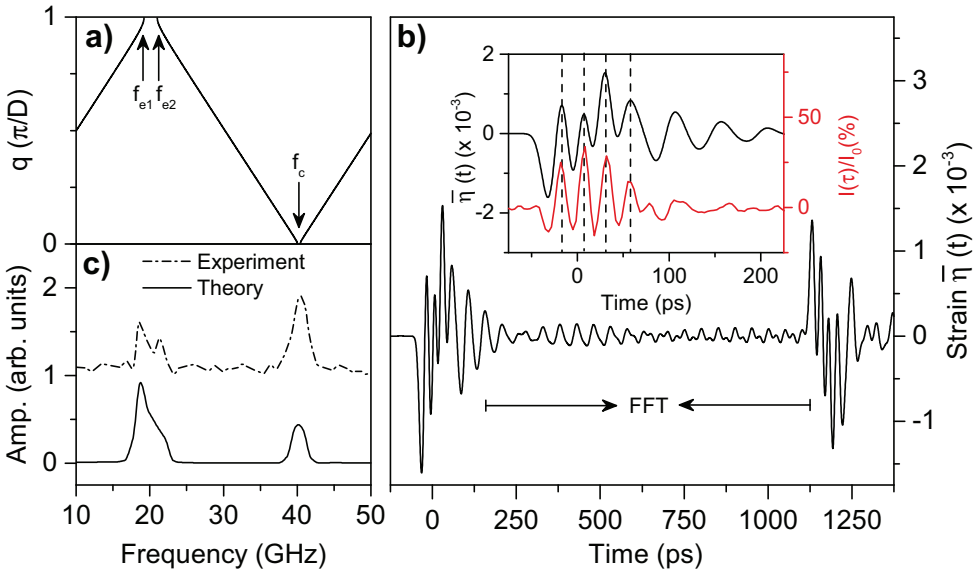

Figure 5.4: Theoretical analysis of the interplay between the acoustic resonances and the lasing process. Panel (a): Phonon dispersion in the VCSEL showing the broad zone-edge and the narrow zone-center stop band at 20 GHz and 40 GHz, respectively. Panel (b): Sum of the strain $\overline{\eta}(t)$ applied to all twelve QWs. Between the transits of the incident and the reflected pulse, the acoustic resonances lead to a non-vanishing net strain. The inset shows the dependence of the laser intensity modulation $\Delta I(\tau)/I_0$ (red curve) on the net strain, which is in first order approximation a linear function. Panel (c): FFT signals of the net strain and the measured laser intensity modulation in the time interval indicated by the arrows in panel (b). The two peaks at 20 GHz correspond well to the calculated DBR modes $f_{1,\mathrm{e1}}$ and $f_{1,\mathrm{e2}}$.

The acoustic resonances set up long-lived mechanical vibrations. The impact of the corresponding strain on the active medium can be treated in a much simpler way when QWs instead of QDs serve as the active medium. The QWs are homogeneously broadened; i.e., the excitons interact with each other and are not isolated like in the case of the QD ensemble. Consequently, there is no highly-excited off-resonant reservoir. In the words of the previous chapter, the shaking effect does not occur for QWs and only the adiabatic contribution needs to be considered. In the following, the laser emission modulation shall be linked to the temporal strain profile. However, the model presented in the previous chapter is not employed here, but a simpler relation will be deduced.

Several approximations are assumed. All QWs are assumed to couple equally to the light field, despite the slightly different amplitude of the light field at their positions. Moreover, the perturbation by the strain field is considered so small that in first order approximation (i) the optical gain modulation of an individual QW is proportional to the applied strain $\eta_i(t)$ and (ii) the lasing emission intensity modulation is a linear function of the gain modulation. Under this conditions, the net laser emission intensity modulation $\Delta I(\tau)/I_0$ is proportional to the sum of the strain applied to all twelve QWs $\overline{\eta}(t) = \sum \eta_i(t)$. In Fig. 5.4 (b) the calculated net strain $\overline{\eta}(t)$ is depicted. As the input displacement pulse, a Gaussian with a FWHM of 8 ps is chosen. This profile does not contain strong nonlinear features and high frequency components, because of the thin substrate and the elevated temperature higher than 50 K. One can clearly see that the strain does not average out, but a non-zero strain field remains. The time-axis is chosen such that at t=0 ps the acoustic pulse reaches the cavity layer center. Strain at times t <0 ps is due to the QWs that are incorporated in the bottom DBR. The inset shows the evolution of the calculated net strain $\overline{\eta}(t)$ and the laser emission modulation $\Delta I(\tau)/I_0$ when the acoustic pulse reaches the central cavity region. The comparison shows that the sequence and the phase of the oscillations match very well, which validates the assumptions made. Finally, the FFT is calculated for $\overline{\eta}(t)$ and $\Delta I(\tau)/I_0$ in the time interval between the incident and the reflected pulse indicated by the arrows (region C in Fig. 5.3). The results are presented in Fig. 5.4 (c) and demonstrate excellent agreement concerning the spectral positions. The relative amplitude is however not perfectly reproduced, which might be related to the phonon spectrum of the input displacement pulse assumed in the simulations. The analysis proves that for a large detuning between the QWs and the cavity mode, acoustic resonances can be exploited to achieve an adiabatic modulation of the laser emission due to spectral shifts of the gain material.

5.3.2 Emission Modulation at 295 K

A second experiment is performed at room temperature (T=295 K). The pump excitation is set to 10 mJ/cm^2 again. Fig. 5.5 presents the results for this temperature. The QWs are now much broader than at T=180 K and in resonance with the cavity mode. The

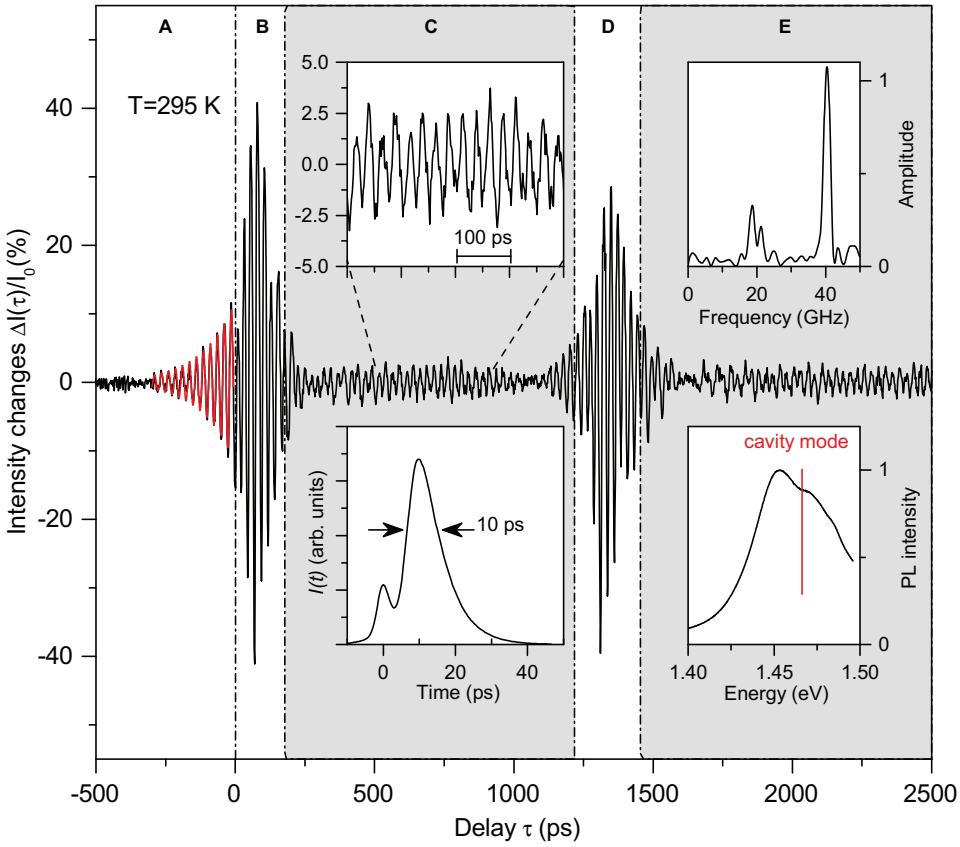

Figure 5.5: Same as for Fig. 5.3, but for a temperature of T=295 K. The most striking difference is the observation of a laser intensity modulation at delays τ <0 ps before the acoustic pulse reaches the gain material. An exponentially decaying oscillation (red curve) is fitted to the data to determine the characteristic length scale of the underlying interaction mechanism.

optical excitation is kept at about four times the lasing threshold, which decreases from 1,600 µJ/cm^2 at T=180 K to 600 µJ/cm^2 at room temperature due to the increased coupling. This improvement also results in a shorter duration of the laser's pulsed emission from 17 ps down to 10 ps, which improves the time resolution of the setup. Since the period of the resonant vibrations is only 25 ps in the case of the zone-center mode at 40 GHz, the oscillations were hardly visible in the previous experiment. This could be the possible reason why now much clearer fingerprints of the acoustic resonances are observed. This time, the amplitude of the oscillations in region C reaches 5 %, which is more than twice of the previous value.

However, the most striking new feature is that the acoustic pulse leads to an intensity

modulation without interacting with the QWs. This becomes obvious when looking at the signal in region A: oscillations with a maximum amplitude of 10 % are observed, which become the stronger, the closer the acoustic pulse advances towards the microcavity center. This modulation cannot be related to spectral shifts of the QWs, since the acoustic pulse has not reached any QWs for negative delays τ <-60 ps [cf. Fig. 5.4 (b)]. By fitting an exponentially decaying oscillation to the experimental curve (red curve in the main panel of Fig. 5.5), and multiplying the found decay constant of 125 ps with the averaged sound velocity in the layered structure of $\overline{v}$=5320 m/s, one obtains the characteristic length scale of 0.66 nm on which the interaction takes place. This value is very close to the penetration depth of the laser light field into the resonator of L_{DBR}=0.81 nm that can be calculated by Eq. (3.7). Obviously, there is a mechanism by which the acoustic pulse manipulates the optical cavity mode.

The interaction of a picosecond acoustic pulse with an optically passive device like a microcavity has been studied before [14]. In the experiments presented there, the reflectivity of a microcavity is monitored during the transit of a picosecond acoustic pulse through the structure. The spectral mode of the cavity is successively redshifted while the acoustic pulse is located in the bottom DBR. The amplitude of this redshift is proportional to the light field distribution at the position of the acoustic pulse and follows it steadily. Consequently, maximum shifts appear, whenever the pulse enters a new doublelayer [cf. Fig. 3.2]. After the acoustic pulse has passed the cavity spacer and enters the top DBR, the redshifts turn into blueshifts. These spectral shifts of the cavity mode are, on the one hand, related to displacements of the DBR layers exerted by the acoustic pulse. On the other hand, the refractive index will be slightly different in strained material. Both effects - one is proportional to the displacement $u(z,t)$, the other to the strain $\eta(z,t)$ - will modify the central stop band of the DBR, which also slightly affects the central cavity mode [cf. Eq. (3.9)]. These two effects are the basic mechanisms for the nanoscopy experiments performed in the third part of this thesis and they are discussed in detail in chapter 8. However, to verify whether the cavity mode is actually influenced by the acoustic pulse, the pulsed laser emission is recorded with the combination of spectrometer and streak-camera. In Fig. 5.6 the VCSEL emission for two different delays τ is presented energetically and temporally resolved. Two slightly different delays are chosen; on the left side a delay of τ=0 ps and on the right side a small negative delay of τ=-6.6 ps. In the case of τ=0 ps, there is a single emission peak at an energy of 1468 meV. If the delay is slightly smaller, one can observe two peaks: one at a slightly lower energy of 1467.5 meV and one approximately at the usual laser mode. However, from the findings of Ref. [14] one would expect a smooth shift of the cavity mode, whereas here the image indicates that there are two competing modes and the laser switches almost instantaneously from one to the other within 20 ps. Unfortunately, the separation between the two modes and the switching time tackle the resolution limits of the setup and the images are rather pixelated; these numbers should

therefore be considered as rough estimates.

The detailed analysis of the optical mode distribution in a laser is quite complex. Many mechanisms like carrier-carrier repulsion, current spreading, spatial hole-burning and thermal effects govern the spatial gain distribution, which determines the operated optical modes. For high excitation powers, all these mechanism make a VCSEL lase in various higher order transverse modes [38]. These modes might instantaneously be switched on when the acoustic pulse breaks the DBR symmetry. Since the detailed analysis of the optical mode distribution is a large scale effort, the discussion is restricted to these quantitative considerations at this point.

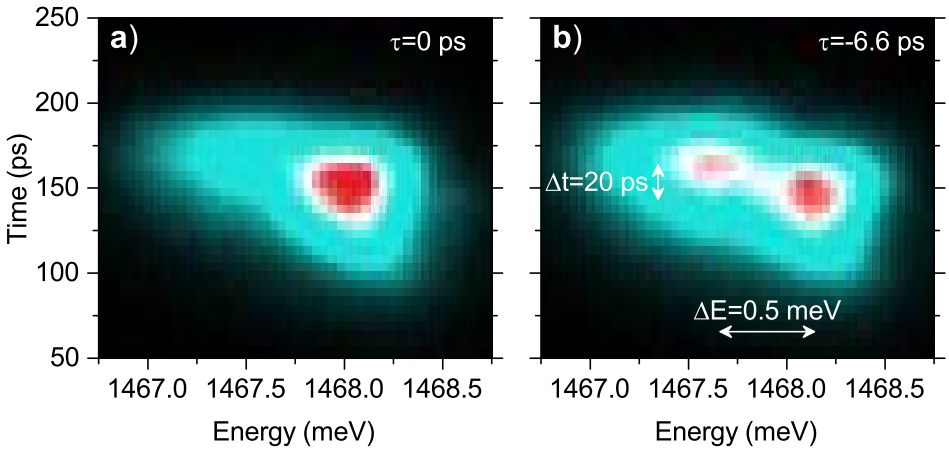

Figure 5.6: Energetically and time-resolved laser emission pulse. Panel (a): Emission pulse for a delay of τ=0 ps, showing a single peak at 1468 meV. Panel (b): Emission pulse for a slight negativ delay of τ=-6.6 ps. The emission occurs also at a second energy of 1467.5 meV and the switching from the lower into the higher energetic mode occurs within 20 ps.

In this chapter, the different possibilities the resonator offers for the modulation of the laser emission by picosecond ultrasonics were presented. The most important observation was that the excitation of phononic resonances supported by the microcavity led to a significant modulation of the laser emission with frequencies of up to 40 GHz, even at room temperature. The lifetime of these resonances was shown to be longer than 1 ns and ultimately given by the acoustic Q-factor. Calculations show that the Q-factor is on the order of ∼1000, which predicts a phonon lifetime of about 20 ns. In the present experiment, DBR modes at the flanks of the acoustic stop bands associated with slowly propagating phonons were responsible for the modulation. The reason for this is most probably that the acoustic resonances were excited by a broadband picosecond acoustic pulse that had been injected from the outside. The confined cavity mode phonons could

not build up in the cavity during the experimentally observed time interval due to the high acoustic Q-factor.

For a large detuning between the QW and the cavity mode (T=180 K), mostly spectral shifts of the gain material modified the laser intensity. The laser intensity was shown to adiabatically follow the net strain applied to all twelve QWs. In an inhomogeneously broadened QD ensemble also the shaking effect plays an important role. If such an ensemble is shaken due to resonant phonons, there will be one red- and one blueshift per period. Each of these shifts will deoccupy QDs adjacent to the spectral hole; i.e. there will be a laser amplification occurring at twice the frequency of the acoustic resonances [134]. Please note that in the experiments presented in the previous chapter, the time resolution of the streak-camera of 25 ps did not allow one to monitor such a fast response with a frequency of 2×∼20 GHz. Therefore, only the adiabatic contribution of the interaction between the laser and the resonant phonons was recorded.

If the detuning is small (T=295 K), also small perturbations of the resonator led to an efficient laser emission modulation. This is most probably related to a manipulation of the competing optical modes in the VCSEL.

In the following chapter, the influence of different pump schemes, namely optical and electrical excitation, will be discussed. Commercially used VCSELs are usually electrically excited and therefore the promising results obtained so far will be demonstrated also for this kind of laser.

Chapter 6

Emission Modulation of Micropillar Lasers

The two previous chapters analyzed the role of the active medium and of the resonator for an emission modulation by picosecond ultrasonics. The last remaining laser constituent that has not been discussed yet is the pump; so far, only optically excited VCSELs have been studied. However, for most applications electrically driven VCSELs are used and it is highly desired to achieve an efficient laser modulation also for this excitation scheme.

Here, two groups of very similar lasers are studied where the only striking difference in the design is that one is electrically and the other optically pumped. The comparison of their response to a picosecond acoustic pulse allows one to find out if electrically and optically pumped lasers behave fundamentally different, or, whether the results obtained in the previous chapters are also applicable to electrically driven VCSELs. Applying an electrical field might be obstructive and prevent an efficient laser modulation: if, for example, the energy band structure is tilted, charge carriers may tunnel out of the heterostructures serving as the active medium [92]. This leads to a shorter lifetime of electrons in off-resonant QDs and might significantly lower the efficiency of the shaking effect. Electrical pumping requires further sample processing. In planar VCSELs, the charge carriers need to be guided from the p- and n-contacts into a small volume inside the gain material to ensure a low laser threshold. Usually, this is achieved with the help of lateral apertures, which are fabricated by selective oxidation. These oxide masks prevent current spreading and can either be located on the front facet [57] or buried in the sample close to the active area [52].

However, there is no need to guide the charge carriers if planar VSCELs are processed further into three dimensional micrometer-sized objects like micropillars, for example. Pillars with a diameter of only a few micrometer do not only easily guide the charge carriers, but they also confine the light field in all directions to the so-called photonic mode volume. In state-of-the-art micropillars with a Q-factor of up to 150,000 [97],

high photon lifetimes and mode volumes with dimensions comparable with the photon wavelength are obtained. These conditions are the prerequisite for the observation of **c**avity-**q**uantum-**e**lectron-**d**ynamics effects (cQED), which is the reason why micropillars have attracted huge interest in the recent years. Early experiments dealt with an enhancement of the spontaneous emission of single or an ensemble of QDs due to the Purcell effect[48, 114]. Highly indistinguishable single photon sources were realized later by single QD placed in microcavities [104, 41]. Finally, also electrically driven lasers based on micropillars are noteworthy, since they offer a record low threshold [96] or demonstrate electrically driven polariton lasing [106]. Micropillars have been studied here instead of planar VCSELs with oxide masks because of the prospective applications in combination with picosecond ultrasonics. These are for example single-photon-emitters triggered by acoustic pulses, or QD position measurements with nanometer resolution [37].

In this chapter, electrically and optically pumped micropillar lasers are subjected to experiments with picosecond ultrasonics. The leading questions are (i) if it is possible to modulate the laser emission from an electrically pumped VCSEL and (ii) if the modulation is fundamentally different from the one of a similar optically excited laser. Another interesting aspect is that micropillars host acoustic eigenvibrations due to their geometric shape along with the usual microcavity modes (DBR and cavity resonances) discussed in the previous chapter. The question, which modes will play the dominant role in the response of the laser, will be answered as well. The chapter is structured as follows: in the first section, the studied micropillar VCSELs and the employed experimental setup are described. Afterwards, the laser emission modulation of electrically pumped micropillar lasers is presented. The results are evaluated with regard to the involved acoustic resonances both analytically and numerically by finite-element-simulations and were published in Ref. [33]. In the following section, the laser emission modulation of optically pumped micropillar lasers is presented and, finally, in the last short section compared with the response of the electrically driven VCSELs.

6.1 Micropillar Lasers and Experimental Setup

All studied micropillars are fabricated from AlAs/GaAs-based planar microcavities. In the case of the *optically* pumped micropillars, the thickness of the AlAs and GaAs layers in the DBRs are 74 nm and 69 nm, respectively. The top DBR is the output coupler and consists of 26 doublelayers, while the bottom DBR serves as the high reflector and is composed of 33 doublelayers. In between the two reflectors, a 266 nm thick λ-cavity layer made from GaAs is sandwiched. At its center, an ensemble of $Al_{0.09}Ga_{0.55}In_{0.36}As$ QDs with a density of 2^9-4^9 cm^{-2} serves as the active medium. Compared to the commonly used InGaAs QDs, the added Al compound yields shorter emission wavelengths. A sample characterization was performed in the group of Christian Schneider in Würzburg. Photoluminescence measurements on a nominally identical QD ensemble grown under

the same conditions show that the lowest electronic transitions are centered at 1.426 eV (870 nm) with a FWHM of 40 meV (25 nm).

Micropillars with radii ranging from 1.5 µm to 7.5 µm were etched out of this planar microcavity. The cavity mode depends on the position on the wafer due to a slight wedge shape of the layers and also on the diameter of the micropillar. Rough sidewalls yield another photon loss channel that becomes the more important, the smaller the micropillar's diameter is [95]. Consequently, the Q-factor increases from 1,500 for a radius of 1.5 µm to 70,000 for a radius of 7.5 µm. An SEM image of a micropillar laser from this sample has been shown above in Fig. 3.3 (c). The substrate of the sample is polished down to 220 µm and a 100 nm thick Al film is deposited on the sample's backside for the generation of acoustic pulses.

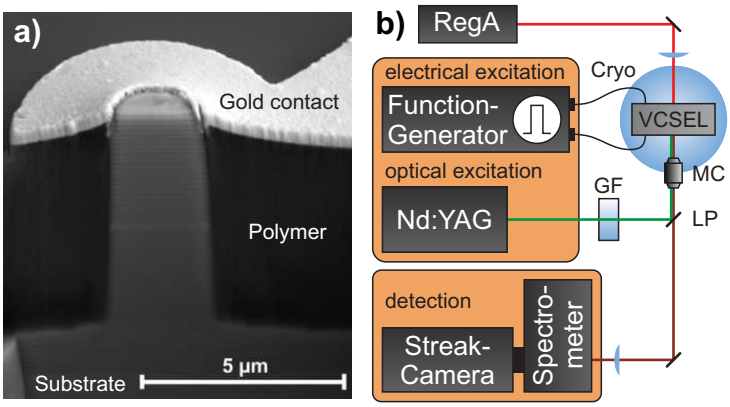

Figure 6.1: Experimental setup to measure the lasing emission from optically and electrically excited micropillars. Panel (a): Cross-section of an electrically pumped micropillar laser with a radius of 1.25 µm. The ring-shaped gold contact on the top is propped by a polymer [95]. Panel (b): Sketch of the experiment. The acoustic pulses are created by the RegA, while the micropillar lasers can either be excited electrically by a function generator or optically by a Nd:YAG laser. The optional excitation laser is focused on single micropillars by a 20 x microscope objective (MC), which is also used to collect the emission. The emission is separated from the excitation beam by a long pass (LP) and forwarded to the detection comprising a spectrometer and a streak camera.

An SEM image of a typical electrically driven micropillar laser is shown in Fig. 6.1 (a) [95]. The underlying microcavity structure of the *electrically* pumped VCSELs studied here is very similar to the one of the optically excited micropillar laser: the DBRs consist of slightly less doublelayers, namely 23 and 27 periods in the bottom and top reflector, respectively. The layer thickness of the AlAs and GaAs layers are 77 nm and 68 nm. Again, a λ-cavity is introduced by a GaAs spacer with a thickness of 297 nm. The active medium is an ensemble of $In_{0.3}Ga_{0.7}As$ QDs. No PL measurements were

recorded, but the growth parameters for this ensemble were almost identical to the ones for the ensemble presented previously in chapter 4. Due to the high standardization and reproducibility of the growth process, the characteristics of the two QD ensembles are therefore most probably similar; as a rough estimation one can assume the energy of the lowest electronic transition to be close to 1350 meV (918 nm) with a FWHM on the order of 10 meV (7 nm). This means that the QDs in the optically excited micropillar (at 870 nm) are about 50 nm blueshifted due to the added aluminum compound.

The microcavity has to be doped in order to turn it into a diode and enable an electric excitation (cf. section 3.2). Therefore, the substrate and the bottom DBR are n-doped by Silicon atoms with a concentration that is gradually decreased from 3×10^{18} cm^{-3} in the substrate to 1×10^{18} cm^{-3} close the cavity. The top DBR is p-doped by the implementation of Carbon atoms with a concentration that increases from 1×10^{18} cm^{-3} close to the cavity to 2×10^{19} cm^{-3} at the top surface. An additional δ-doping with a concentration of 1×10^{12} cm^{-2} at the internal AlAs/GaAs interfaces optimizes the conductivity. This doping is only applied to interfaces at which the photonic field possesses a node to prevent light absorption from charge carriers [16]. The sample is grown on a GaAs substrate, that is thinned down to a thickness of 100 µm and at the backside the mandatory aluminum film is deposited again. While an electric contact to the substrate can easily be established with the help of this aluminum film, the situation on the front side is more complicated and requires further processing. After the etching process, the sample is planarized by filling the gaps between the micropillars with a polymer (BCB). The polymer props a gold ring which is deposited on the top of the micropillar and encloses its top facet [cf. the SEM image in Fig. 6.1 (a)]. This gold ring serves as the p-contact.

Fig. 6.1 (b) depicts the two slightly different experimental setups employed for the study of electrically and optically pumped micropillar lasers. In both cases, the acoustic pulse is generated by an amplified laser system (RegA), that is focused onto the aluminum film to a spot with a diameter of 150 µm. The laser emission is collected with a microscope objective with a twenty-fold magnification and a working distance of 2 cm. Since aligning the microscope to a single micropillar requires some fine adjustment, the microscope objective is mounted on a nano-positioner. For the analysis of the laser emission, the same combination of spectrometer and streak camera like described in section 5.2 is used. Longer time windows (∼10 ns) are observed with the streak camera in this experiment and therefore the sweep electrodes are operated with the slow electronics offering a maximum time resolution of 25 ps. This is nevertheless not a real drawback, because spectral rather than temporal resolution will be important this time. Another grating with 1200 slits/mm is installed in the spectrometer to increase the spectral at the cost of the temporal resolution such that the setup ends up with lower limits of 0.05 nm (∼0.09 meV) and 50 ps, respectively. The experiments are performed at cryogenic temperatures around 8 K. Due to the short working distance of the microscope

objective, the samples need to be placed in a flow-cryostat, where they are mounted on a cold finger.

Optically excited micropillar lasers, on the one hand, are pumped with the same pulsed Nd:YAG laser as presented in section 4.2. The laser is synchronized with the RegA and its beam is focused with the microscope objective onto the micropillar to a spot with a diameter of approximately 8 µm. An interference low-pass filter is used to bring this beam on the same beam path like the laser emission and steer it into the microscope objective. The electrically driven lasers, on the other hand, are connected to a function generator. The repetition rate of the function generator is synchronized with the RegA as well. Rectangular electrical pulses, whose amplitude and duration are adjustable, are used for the excitation. Please note that usually the laser emission is recorded during a time window of about ten nanoseconds after the injection of the acoustic pulse. In order not to saturate the streak-camera, the laser is supposed to emit light only during this time and the duration of the electrical pulses has to be chosen accordingly (∼25 ns). The function generator produces notable spikes for such short pulses ('Gibbs phenomenon'). This spikes may damage the VCSEL permanently and one needs to adjust the amplitude very carefully.

6.2 Electrically Pumped Micropillar VCSELs

The laser emission response on the impact of a picosecond acoustic pulse is measured for several electrically driven VCSELs. From among the many studied VCSELs, three representative lasers are discussed here because they show a remarkably different behavior despite were very similar or even identical nominal growth parameters.

6.2.1 Experimental Results

All lasers show a modulation of the emission in terms of intensity I and central emission wavelength λ_c, but the modulation amplitude and the frequency spectrum is often strikingly different. The time- and energy-resolved laser emission modulation for the three selected VCSELs is shown in the streak-camera images in Fig. 6.2. The emission is recorded for a time interval of 15 ns, which starts 2.5 ns before the acoustic pulse reaches the VCSELs at t=0 ns. First, the modulation of the central wavelength $\lambda_c(t)$ that is found by

$$\lambda_c(t) = \sum_{\lambda} \frac{I(\lambda, t)\lambda}{\lambda} \tag{6.1}$$

is discussed. This computing allows to find the central emission wavelength with a very high precision higher than the nominal resolution value (that is related to the possibility to distinguish two distinct peaks). In the streak-camera images this weighted mean is indicated by the thick black lines. For all of the three VCSELs, oscillations of the

emission wavelength with a similar amplitude of about ∼0.03 nm are observed. However, the frequency spectrum depicted on the right side of Fig. 6.2 looks very different. The symbols represent data points while solid lines are b-splines that serve as guides for the eyes. In the case of VCSEL E1 with a diameter of d=3 µm, three peaks at f_0=0.18 GHz, f_1=0.47 GHz, and f_2=0.77 GHz appear with an amplitude gradually decreasing in this order. The corresponding oscillations fade after 5 ns. The spectrum of VCSEL E2 with d=4 µm possesses several peaks, from which a dominant peak appears at f=0.9 GHz. The corresponding time evolution shows a rather irregular behavior. After t=5 ns one can see that more or less harmonic oscillations corresponding to the dominant peak remain. This trend towards a single frequency peak continues for VCSEL E3, whose diameter is again d=3 µm. In the first 4 ns after the arrival time of the acoustic pulse also an irregular modulation takes place, which is followed by a very clear and well pronounced harmonic oscillation with a quality factor exceeding 10. This is reflected well by the spectrum that shows a single peak at f=1.24 GHz.

The spectrally integrated intensity modulation of the streak camera images is plotted in Fig. 6.3 (a). The intensity change $\Delta I(t)$ is normalized to the unperturbed intensity I_0. One can see that also the relative intensity modulation for the three lasers looks very different. The first laser VCSEL E1, whose wavelength is only slowly modulated, is lasing with almost constant intensity. Only shortly after the injection of the acoustic pulse at t=2 ns a dip of 10 % with a duration of 1 ns is observed. In the case of VCSEL E2, the irregular shaking occuring from t=0 ns to t=5 ns is accompanied by a huge intensity modulation. The laser emission is most of the time quenched and the intensity drops by up to 40 %. The harmonic oscillations of $\lambda_c(t)$ starting afterwards are not translated into an intensity modulation at a first glance. Nevertheless, there is a distinct peak at f=0.90 GHz in the frequency spectrum of the intensity modulation plotted in Fig. 6.3 (b) besides several smaller peaks at lower frequencies. For VCSEL E3 the intensity modulation clearly resembles the shifts of the wavelength. In the time interval from t=0 ns to t=4 ns, the intensity is irregularly modulated, while afterwards harmonic oscillations with a frequency of 1.24 GHz and an amplitude of about 10 % are observed. The frequency spectrum possesses again a single well pronounced peak.

6.2.2 Theoretical Analysis

The observed frequencies do not correspond to any phononic resonances of the microcavities. These are supposed to appear at frequencies higher than 20 GHz for the AlAs/GaAs layer thicknesses of the DBRs. Obviously, the vibrations must arise from the shape of the micropillars. The picosecond strain pulses arriving at the foot of the micropillar excite its mechanical eigenmodes. Motion in the growth direction along the axis of the pillar (z-direction) modifies the layer thicknesses of the cavity layer and the DBR layers such that the cavity mode is modulated. This becomes observable in a modulation of the emission wavelength $\lambda_c(t)$. Strain tensor components η_{ij} independent from whether

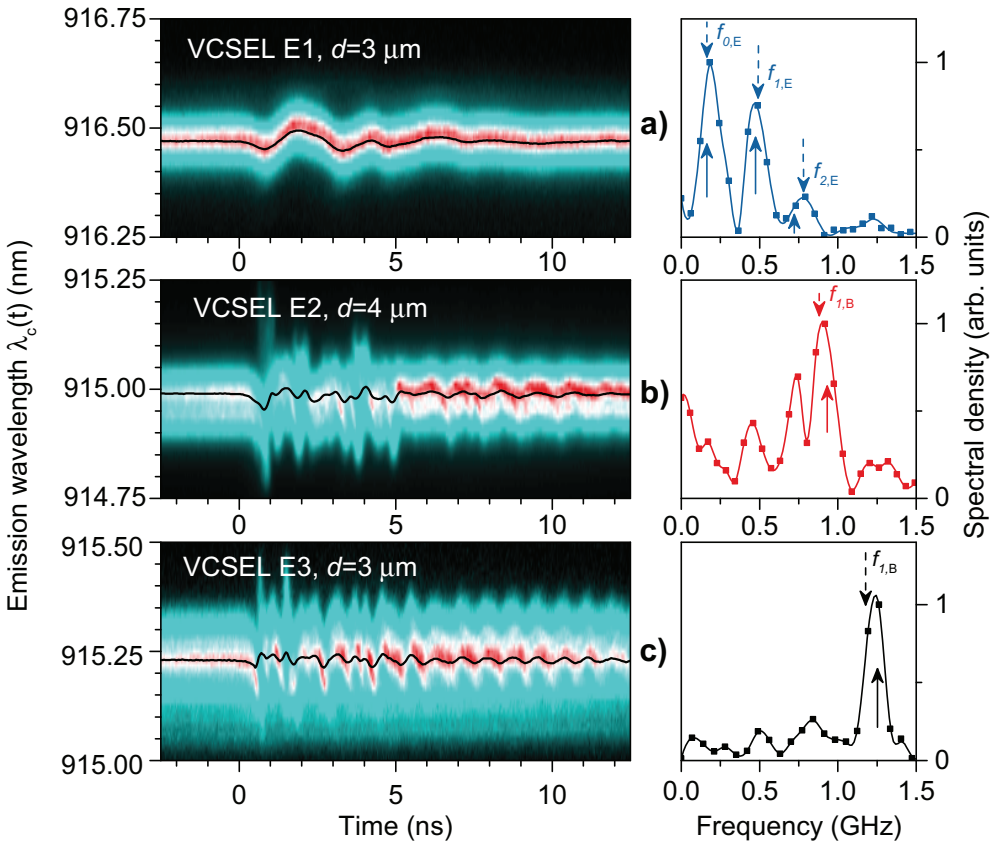

Figure 6.2: Laser emission modulation for the three studied electrically driven VCSEL. Left: Streak camera images. Red color corresponds to high and black to low intensity. The solid black line shows the evolution of the central emission wavelength $\lambda_c(t)$. Right: FFT spectra of $\lambda_c(t)$. The arrows indicate the numerically (solid arrows) and analytically (dashed lines) calculated frequencies of the extensional and breathing modes.

they lead to uniaxial (diagonal components) or shear (off-diagonal) deformations both modify the dielectric function of the layers, which also results in a modulation of $\lambda_c(t)$. Moreover, the strain my vary the electronic energies in the QDs (cf. chapter 4) leading to the observed emission intensity modulation.

The first step in the analysis is to numerically calculate the mechanical eigenmodes of the micropillar. This simulation is done by the finite-element program *COMSOL*. In the simulations, the micropillars are modeled by uniform pillars composed of an AlAs/GaAs alloy. The material parameters of the alloy are obtained from the ones of AlAs and GaAs, which are weighted by their respective content in the sample. The important mechanical quantities are Young's modulus Y=84.34 GPa, the sound velocity v=5219 m/s, the mass

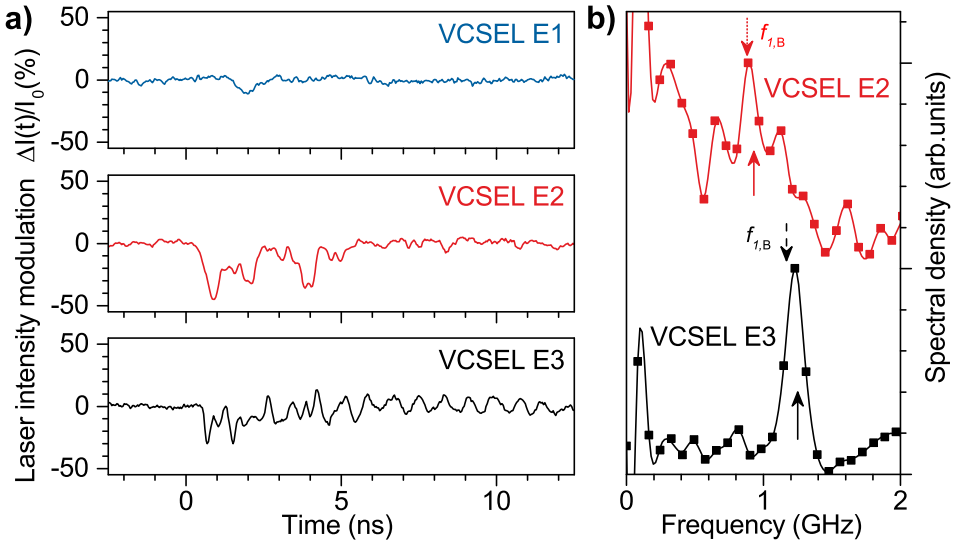

Figure 6.3: Laser intensity modulation for the three studied electrically driven VCSELs. Panel (a): Relative intensity modulation $\Delta I(t)/I_0$ integrated over the whole emission spectrum. Panel (b): The spectra of the two VCSEL for which an efficient modulation is observed. The arrows indicate the numerically (solid arrows) and analytically (dashed arrows) calculated frequencies of the breathing modes.

density ρ=4.5 g/cm^3, and Poission's ratio ν=0.34. The treatment of the micropillar as a monolithic block is only valid for phonons with wavelengths much longer than the layer thicknesses. The weighted average for the different elastic parameters is generally not valid, but a rule of mixture needs to be applied. In layered structures, there are different rules of mixture for loads along or perpendicular to the growth direction [8]. These rules also predict an upper and a lower limit for the elastic properties. However, due to the almost equal content of AlAs and GaAs in the micropillar and the very similar elastic coefficients (Y_{GaAs}=85.9 GPa and Y_{AlAs}=83.5 GPa as well as ν_{GaAs}=0.34 and ν_{AlAs}=0.34 [1]), the upper and lower limit are both almost identical to the weighted mean. The bottom ends of the micropillars are immobile attached to the GaAs substrate. The surrounding polymer and the gold ring contacts on the top are not included, because the acoustic impedance of AlAs and GaAs are about ten times higher than the one of BCB [78].

Fig. 6.4 illustrates the result for a micropillar with a diameter of d=3 µm and a height of h=7.5 µm that equals the nominal thickness of the planar microcavity fabricated in the first place. The first three mechanical eigenmodes appear at f=0.16 GHz, f=0.47 GHz, and f=0.72 GHz. These frequencies match the three peaks in the spectrum of the wavelength modulation $\lambda_c(t)$ of VCSEL E1 very well [cf. Fig. 6.2 (a)]. In the images, red volume represents parts of the pillar where the displacement of the eigenmode is large,

while blue volumes stay fixed. The displacement distribution of the first mode shows movement only along the micropillar axis in the z-direction; the bottom of the micropillar is fixed, because it is bound to the substrate, while the displacement amplitude is increasing steadily towards the top of the micropillar. In the case of the other modes, the distribution is more complex and the displacement also depends on the radial distance from the axis of the pillar. In the case of the second and third eigenmode, one and two additional nodes appear as blue volumes in the center of the micropillar, respectively. For the fourth eigenmode at f=1.25 GHz no such statement can be made, because the field distribution looks highly irregular.

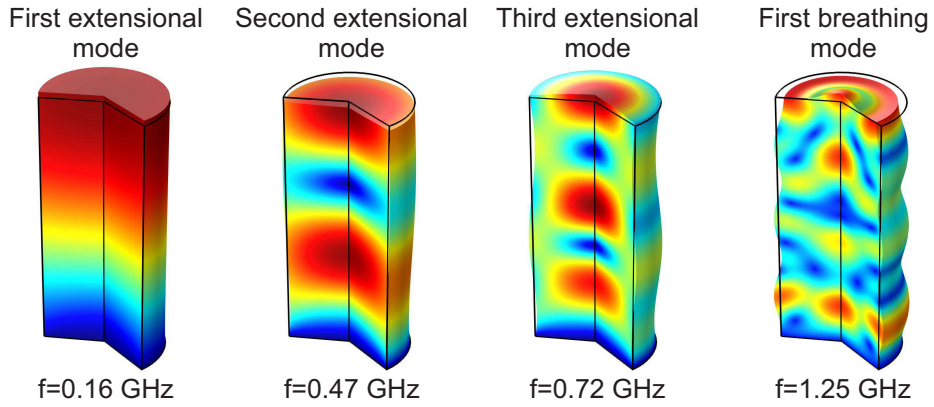

Figure 6.4: Finite-element simulations of the first four mechanical eigenmodes of a pillar with a diameter of d=3 µm and a height of 7.5 µm made from an AlAs/GaAs alloy. Red color indicates volume with a large displacement, while blue volume remains fixed. The comparison with analytical calculations allows to assign the numerical solutions to the extensional and breathing modes.

In the next step, the numerically calculated frequencies shall be compared with the two classes of vibrational modes hosted by micropillars, namely extensional and breathing eigenmodes. An analytical expression can be obtained for pillars, whose height is large compared to the diameter $h \gg d$. Extensional modes are eigenvibrations in which the height of the pillar is alternating and where the motion is exclusively along the z-axis. If one end of the pillar is fixed, the ground mode possesses one displacement node at the foot of the pillar. For each higher order, one further node inside the pillar is added. The frequencies of the n-th order extensional mode is given by

$$f_{n,\mathrm{E}} = \frac{v}{2h}(n + 1/2), \tag{6.2}$$

where $n = 0, 1, 2, \ldots$ [68]. Breathing modes describe vibrations of the pillar during which the diameter d is periodically changed. For free-floating pillars (e.g. for nanorods in a solution [56]), the motion is only along the radius and there is no motion along the axis

in z-direction. The displacement field is in this case radial-symmetric and possesses a node at the axis. The displacement gradually increases towards the sidewalls. For each higher breathing mode order, an additional 'node-ring' at a fixed distance from the axis appears. The frequencies of the n-th order breathing modes can be found via

$$f_{n,\mathrm{B}} = \frac{\tau_n v}{\pi d} \tag{6.3}$$

with $n = 1, 2, 3, \ldots$. Here, τ_n is a dimensionless parameter on the order of $\sim$1. It is given by the n-th root of an implicit equation involving Bessel functions of the first kind J_0 and J_1, which mirror the symmetry of the pillar, and Poisson's ratio ν [68]:

$$\tau_n J_0(\tau) = \frac{1-2\nu}{1-\nu} J_1(\tau). \tag{6.4}$$

In the last step, the analytically obtained frequencies for the various eigenmodes will be compared with the numerically calculated eigenfrequencies. In the FFT spectrum of $\lambda_\mathrm{c}(t)$ for VCSEL E1 shown in Fig. 6.2 (a), the analytically calculated values for the three first extensional modes $f_{0,\mathrm{E}}$, $f_{1,\mathrm{E}}$, and $f_{2,\mathrm{E}}$ are sketched by dashed arrows along with the first three numerically obtained eigenfrequencies indicated by the solid arrows. Moreover, the analytically found breathing ground mode $f_{1,\mathrm{B}}$ (dashed arrow) and the fourth numerically obtained frequency (solid arrow) are plotted in the FFT spectra of $\lambda_\mathrm{c}(t)$ for VCSEL E2 and VCSEL E3 [cf. Fig. 6.2 (b) and Fig. 6.2 (c), respectively]. One can see that the analytically and the numerically obtained frequency match very well.

This agreement proves that the analytical approach is indeed correct, although the diameter is on the same order as the height of the micropillar. Moreover, the numerically found frequencies can be attributed to breathing or extensional modes, which is not very obvious when looking at the displacement distribution alone. Especially the identification of the breathing mode in Fig. 6.4 is difficult, because the displacement distribution looks very different from the predicted shape due to the fixed foot of the micropillar. The validity of this classification has further been proven by varying the height and diameter of the micropillar in the simulations. The frequencies properly show the linear dependence on h^{-1} and d^{-1}, respectively. Moreover, the calculated eigenmodes match the peaks in the FFT spectra of $\lambda_\mathrm{c}(t)$ very well. From these findings one can conclude that the response of the different VCSELs is governed by the mechanical eigenmodes of the micropillars.

While extensional modes very efficiently modulate the emission wavelength $\lambda_\mathrm{c}(t)$, their signatures are barely found in the FFT spectra of the intensity modulation $\Delta I(t)/I_0$ in Fig. 6.3 (b). One possible reason is related to the different frequencies of the two classes of mechanical eigenmodes. The interaction of a mechanical strain field with an inhomogeneously broadened QD ensemble can be well understood by the model presented in chapter 4. Further theoretical studies are performed in Ref. [134]. With their help the frequency dependence of the transient lasing modulation due to the shaking effect

can be understand. The simulations in this work show that the efficiency peaks at a certain frequency; the period of the mechanical vibrations must be higher than the exciton lifetime but for very high frequencies the electrons cannot follow the dynamics of the strain field anymore and the shaking efficiency drops. From this point of view, the extensional modes are too slow to dynamically increase the number of QDs contributing to the laser. They still might yield an adiabatic response, which however, does not seem to affect the lasing intensity strongly. The frequency of the breathing mode is about 1 GHz, such that the period of the oscillations is shorter than the lifetime of excitons in InGaAs QDs, i.e. $f_{1,\mathrm{B}}^{-1}$ <1.5 ns [cf. Fig. 4.3 (b)].

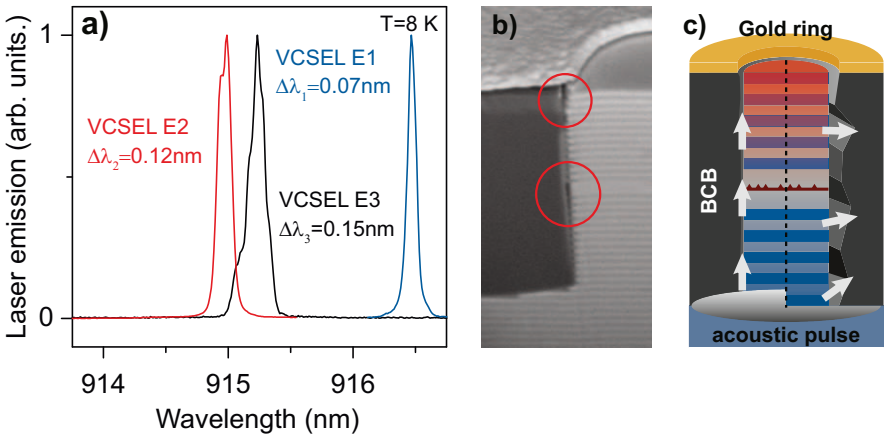

Figure 6.5: Excitation scheme of extensional and breathing acoustic modes. Panel (a): Laser emission spectra. The linewidth allows to assess the Q-factor, which is determined by the sidewall quality. Panel (b): Cross-sectional SEM image of a micropillar. The red circles indicate gaps between the micropillar and the surrounding polymer. The occurrence of such gaps might be related to the sidewall quality. Panel (c): Relation between the contact of micropillar and polymer and the acoustic modes. Good contact (left side) allows the acoustic pulse traveling in the polymer to grab the micropillar and start longitudinal motion. Bad contact (right side) leads to gaps between the polymer and the walls, at which the acoustic pulse is scattered and radial motions might be launched.

An open question is still why the acoustic pulse starts different classes of mechanical eigenmodes in the studied VCSELs. The spectrum of excited modes does not depend on the diameter of the studied micropillars: VCSEL E1 with d=3 µm features extensional modes only; a mixed spectrum of various modes is excited in VCSEL E2 with d=4 µm; finally, in VCSEL E3 with again d=3 µm the first breathing mode dominates the wavelength and intensity modulation spectra. Obviously, the different response on the acoustic pulse is not connected to the nominal geometry of the micropillars. The most delicate step during the fabrication is the etching process during which the mi-

cropillars are shaped out of the initially planar microcavity. Although achieving high quality sidewalls becomes feasible nowadays [97], the roughness still slightly differs from micropillar to micropillar. The sidewall quality strongly influences the Q-factor of the micropillar cavity and can therefore be assessed from the linewidth of the laser emission. Fig. 6.5 (a) shows the spectra of the laser emission for the three studied VCSELs in absence of the acoustic pulse. VCSEL E1 features the narrowest line with a width of $\Delta\lambda$=0.07 nm, while the lines of VCSEL E2 and VCSEL E3 are significantly broader with a FWHM of $\Delta\lambda$=0.12 nm and $\Delta\lambda$=0.15 nm, respectively. On a qualitative level one can deduce that VCSEL E1 features the best, VCSEL E2 a moderate and VCSEL E3 the worst sidewall quality.

The roughness might affect the way the polymer used to fill the gaps between the micropillars sticks to the walls. Fig. 6.5 (b) shows a SEM images of a cross-sectional cut of a micropillar. The two red circles indicate gaps between the polymer (BCB) and the micropillar, where the polymer does not cover the walls. It might be that not the micropillars themselves determine which acoustic modes are excited, but the polymer environment.

In Fig. 6.5 (c) a micropillar with a good (left) and a bad contact (right) with the polymer environment is sketched. If the contact is good, acoustic pulses propagating through the polymer next to the micropillar may induce longitudinal motion, since the polymer grabs the micropillar. Thereby, extensional modes may be started. The damping of these modes is however supposed to be rather pronounced because of the strong leaking into the substrate. Indeed, the extensional modes started in VCSEL E1 decay after only a few periods. In the case of a good contact also radial modes are not expected to possesses a long lifetime, because they couple strongly to the polymer.

If in contrast there are huge gaps between the polymer and the micropillar, the acoustic pulse coming from the substrate is scattered at these locations. Such scattering process might excite modes that do not reflect the symmetry of the acoustic pulse, i.e. modes with motion not only along the z-direction. Moreover, a freestanding micropillar is also able to perform long-lived radial vibrations, since the contact to the polymer is weak and axial oscillations probably do not leak very strongly into the substrate.

In electrically pumped micropillar lasers the emission is modulated due to nanomechanical eigenmodes of the micropillar, which are started by picosecond acoustic pulses. No unambiguous signatures of neither the picosecond acoustic pulse itself passing through the QD layer nor of phononic resonances due to the DBRs were found [1]. In fact, it will be demonstrated in chapter 10 that in general picosecond acoustic pulses may enter micropillars, but phonons with a frequency above ∼40 GHz are not observed inside. The modulation can well be explained by the extensional and breathing modes of the

[1] The emission was also recorded with a shorter streak camera time window of 2 ns providing a time resolution of 25 ps for a verification

micropillar. Its acoustic environment, namely its contact to the surrounding polymer, seem to determine which modes are excited. In the following section, the lasing emission of freestanding optically pumped micropillar lasers will be investigated. The comparison of the results will be used to evaluate if the response of electrically and optically pumped lasers to picosecond acoustic pulses is fundamentally different.

6.3 Optically Pumped Micropillar VCSELs

Two optically pumped micropillars VCSEL O1 and VCSEL O2 with diameters of d=3 µm and d=5 µm, respectively, are investigated. These representative lasers are chosen here, since their feature pronounced long-lived oscillations. The lasers are optically excited by 23 ns long laser pulses and the emission is recorded in a 10 ns long time window. The trigger signal for the excitation laser is chosen such that the maximum excitation intensity overlaps with the center of the recorded time interval. The excitation density in this maximum is chosen to be about three times the laser threshold. The left side of Fig. 6.6 shows the laser emission recorded by the spectrometer-streak camera-combination. As expected, VCSEL O1 possesses a broader emission linewidth than VCSEL O2 due to the thinner diameter and consequently lower Q-factor. At t=0 ns, the acoustic pulse reaches the micropillars and like for electrically driven VCSELs, a pronounced modulation of the central emission wavelength $\lambda_c(t)$ (black line) takes place. Please note that the slight redshift of the emission wavelength is probably related to a temperature increase of the laser due to the optical excitation.

In VCSEL O1 rather irregular oscillations persist during the whole recorded time range. Compared to the wavelength shifts in the polymer-surrounded electrically driven VCSELs, the maximum shift is about doubled here to 0.07 nm. The time it takes the acoustic pulse to travel twice through the top DBR is about 1.45 ns. The two salient bipolar features centered at t=0.25 ns and t=1.35 ns are therefore probably related to the transit of the acoustic pulse through the central cavity layer. For the analysis of the oscillations appearing later on, a FFT is performed for t >0 ns. The result is shown on the right side of Fig. 6.6 (a). A series of peaks with an equidistant splitting is found. Such a spectrum is expected for the extensional modes of a micropillar [cf. Eq. (6.2)]. These are calculated for the nominal parameters of the micropillar, which are h=8.7 µm and v=5243 m/s. The dashed arrows indicate their frequencies starting from $f_{2,\mathrm{E}}$ to $f_{8,\mathrm{E}}$, which agree well with the several experimentally found frequencies. The breathing mode of VCSEL O1 is supposed to appear at $f_{1,\mathrm{B}}$=1.25 GHz and almost coincides with the fourth extensional mode $f_{4,\mathrm{E}}$=1.31 GHz. However, the FFT spectrum shows only a minor peak there so obviously the breathing mode does not play an important role here.

The response of VCSEL O2 looks very similar at a first glance. The evolution of $\lambda_c(t)$ also exhibits two pronounced leading features. The first bipolar feature at t=0.4 ns is associated with the transit of the acoustic pulse through the central cavity layer. After

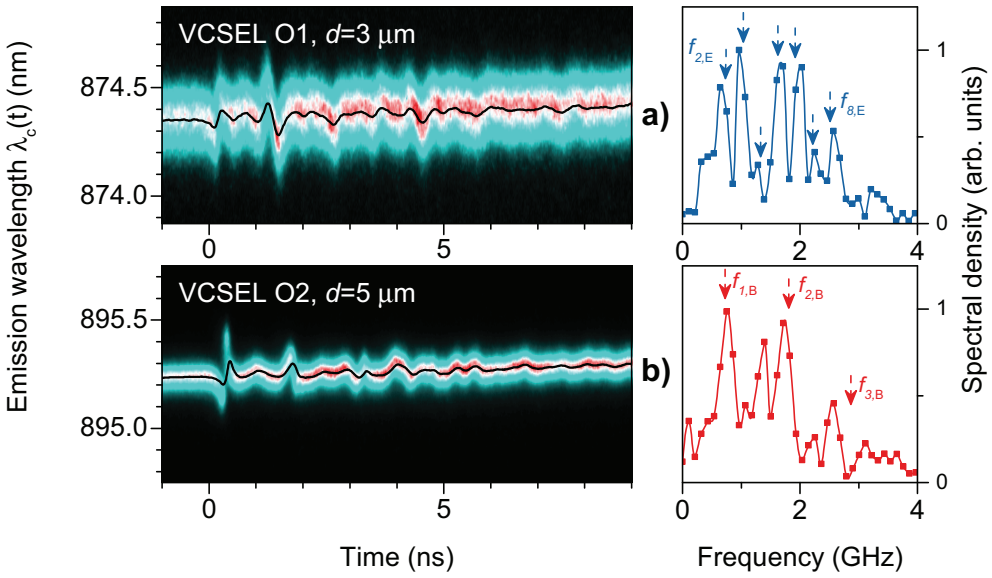

Figure 6.6: Laser emission modulation for the two studied optically pumped VCSELs. Left: Streak camera images. Red color corresponds to high and black to low intensity. The solid black line shows the evolution of the central emission wavelength $\lambda_c(t)$. Right: FFT spectra of $\lambda_c(t)$. The arrows indicate the analytically calculated frequencies of the extensional modes.

the reflection from the top surface, a second big shift is observed at t=1.8 ns. The temporal difference between the two passages is larger than in VCSEL O1; i.e. the top DBR is thicker. This is probably due to the wedge shape of sample, since VCSEL O1 and VCSEL O2 are located at different spots on the wafer. After the acoustic pulse has left the QD layer for t >1.8 ns, VCSEL O2 is vibrating with its nanomechanical eigenmodes. In the FFT spectrum only four peaks appear, from which the first at 0.75 GHz, the third at 1.72 GHz, and the fourth at 2.58 GHz form an almost equally spaced series, while the second peak appears in between at 1.40 GHz. At first, the series of peaks (peak one, three, and four) is examined. The spacing between these peaks is 0.97 GHz (peak one and three) and 0.86 GHz (peak three and four), which is about three times the spacing between adjacent extensional modes. Therefore, breathing modes are considered to be responsible for the found modulation of $\lambda_c(t)$: the dashed arrows show the frequencies of the first three calculated radial modes. Good agreement is achieved between the experimentally found peak for the first breathing mode at $f_{1,B}$=0.75 GHz. For the higher order modes at $f_{2,B}$=1.81 GHz and $f_{3,B}$=2.86 GHz, respectively, this agreement worsens. Most probably, the analytical expression is not a good approximation for VCSEL O2 anymore, because the diameter and the height of the pillar are almost the same. Moreover, the numerically calculated mode distributions in Fig. 6.4 deviate the

more from the analytical solution, the higher the order. While the motion is exclusively in the z-direction in the case of the first extensional mode (like the analytical solution predicts), the higher orders involve also evermore radial motion. The agreement between the analytically calculated and numerically found modes is consequently expected to worsen for higher orders.

Finally, the second peak in the FFT spectrum at f=1.4 GHz is not related to any radial mode and associated with some not further contemplated longitudinal motion.

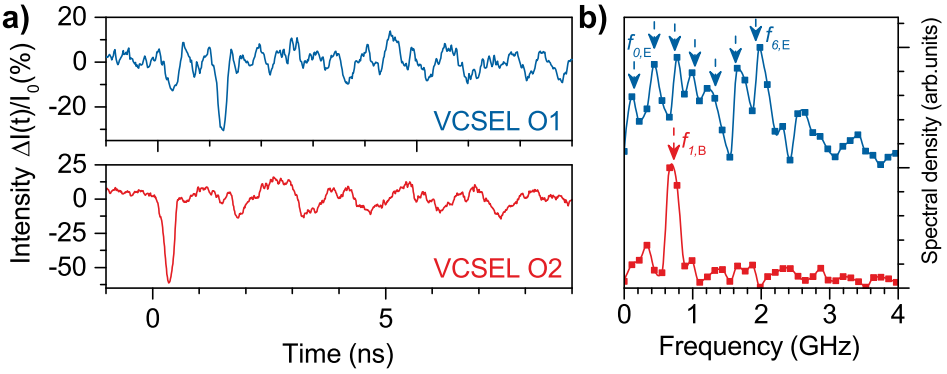

Figure 6.7: Laser intensity modulation for the two studied optically pumped VCSELs. Panel (a): Relative intensity modulation $\Delta I(t)/I_0$ integrated over the whole emission spectrum. Panel (b): FFT spectra of the found intensity modulation. The arrow indicates the analytically calculated frequencies of the extensional and breathing modes.

The relative modulation of the spectrally integrated intensity $\Delta I(t)/I_0$ is plotted in Fig. 6.7 (a). In VCSEL O1, the two transits of the acoustic pulse can be clearly identified by the two drops at t=0.25 ns and t=1.35 ns. Afterwards, the emission is modulated with a maximum amplitude of about 15 % throughout the whole recorded time window. The FFT spectrum of the intensity modulation and the wavelength shifts of VCSEL O1 look very similar [see Fig. 6.7 (b) and the right side of Fig. 6.6 (a)]. Again, a frequency comb of many equidistant peaks appears that can be assigned to the extensional modes (dashed arrows). Unlike in the case of the electrically pumped VCSEL E1, also low frequency components like $f_{0,\mathrm{E}}$=0.15 GHz and $f_{1,\mathrm{E}}$=0.45 GHz yield a small but non-zero contribution.

In VCSEL O2 the first transit of the acoustic pulse leads to a massive drop of the lasing efficiency by 60 %, while the reflected acoustic pulse is barely recognizable. Apparently, the whole acoustic energy is converted into eigenvibrations of the micropillar. This hypothesis goes well along with the fact that a harmonic oscillation of the lasing emission sets in at t ∼2 ns. This harmonic oscillation has an amplitude of about 10 % and a frequency of 0.72 GHz, which corresponds to the first breathing mode $f_{1,\mathrm{B}}$. The other two breathing modes that were observed in the FFT spectrum for $\lambda_\mathrm{c}(t)$ are not found

here.

Just like in the case of electrically pumped VCSELs, different classes of mechanical modes are excited here, although there is no surrounding polymer that influences the acoustic environment. In the case of freestanding micropillars, the acoustic environment should be basically the same. However, the sample was initially fabricated for cQED experiments without involving picosecond ultrasonics. Therefore, the substrate was not thinned down and polished and there was no aluminum film deposited on its backside. In general, picosecond acoustic pulses can be generated without the aluminum film. A femtosecond laser can be focused on semiconductor structures and create a picosecond acoustic pulse, given that the absorption length is sufficiently short (∼10 nm). For GaAs/AlAs, this requires wavelength in the near-UV (∼400 nm) [103]. With the femtosecond laser system at hand that emits at 800 nm, these wavelengths are easily accessible by **s**econd **h**armonic **g**eneration (SHG). The drawback of this scheme is that the generation of the acoustic pulse with high power laser pulses is accompanied by the excitation of electron-hole-pairs. These can feed the laser and strongly influence the lasing emission. It would be hard to distinguish the effects originating from strain and from free charge carriers. In contrast, having an aluminum film on the backside allows to spatially separate the studied structures from the generation area of the acoustic pulse. Therefore, the metal film is mandatory if the laser emission modulation due to coherent phonons shall be assessed.

Depositing the aluminum film on the sample backside was rather challenging, because the micropillars on the front were already carved out. Usually the samples are glued with the front facet to a holder while the substrate is polished and the metal film is deposited. In order to protect the micropillars from the glue, a thin cover made from photoresist was spin coated on the sample. Fig. 6.8 (a) shows a microscope image from an intact micropillar array with different radii under this protective cover. After the substrate had been thinned and the metal film had been fabricated, the photoresist was removed in an acetone ultrasound bath. In most of the spots, the micropillars survived this treatment and only little remnants of the photoresist were found [cf. Fig. 6.8(b)]. Some areas are unfortunately permanently damaged: either by stains of photoresist that could not be removed or because the micropillars were broken and completely destroyed. Fig. 6.8 (c) depicts such an area, where the damage is quite noticeable. The procedure of adding and removing the photoresist cover was carried out and the images were taken by the group of Horst Fiedler from the TU Dortmund university.

The micropillars are selected by two criteria during the experiments. First, images from the sample surface are obtained with the same microscope objective that is also used to collect the emission in order to select an undamaged micropillar array. Unfortunately, these images do not have the same optical quality (in terms of magnification, contrast, lighting, resolution) like the ones obtained during the preparation process shown in Fig. 6.8 and it is hard to say whether individual micropillars are really undam-

aged. When an undamaged array is found, the micropillars with the narrowest linewidth (which often goes hand in hand with a low laser threshold) among those who feature the proper mode distribution expected from Eq. (3.10) is chosen. This approach guarantees that the micropillar is not broken but does not ensure that the micropillar is not covered by small amounts of remaining photoresist. These stains might influence the mechanical properties of the micropillars and determine, which eigenmodes are excited by the acoustic pulse.

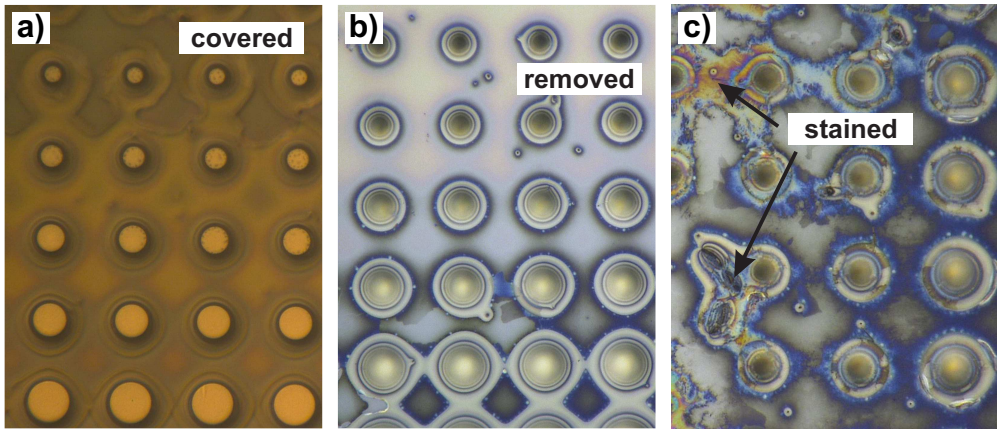

Figure 6.8: Top views of micropillars during the substrate polishing process. Panel (a): photoresist covered micropillars. Panel (b): Micropillars after the resist has been removed in an acetone ultrasound bath. Panel (c): Some areas remain stained and even destroyed micropillars are observed.

6.4 Comparison between Electrically and Optically Pumped VCSELs

The comparison of the results for electrically and optically driven micropillars revealed that both lasers behave basically in the same way. Either extensional, breathing, or a mixture of both nanomechanical modes were excited, which leds to a modulation of the emission wavelength and intensity. While the modulation of the emission wavelength did not depend on the frequency of the vibration, the intensity modulation was more efficient for frequencies, whose period is approximately in the same order or shorter than the lifetime of the electrons; i.e. $f > \sim 1$ GHz. Especially in VCSEL E1, where only the lowest order extensional modes were vibrating, the intensity modulation was almost negligible. The strongest intensity quenching by a factor of about 50% was observed in the optically and electrically pumped VCSELs shortly after the injection of the acoustic pulse into the micropillars. At least in the case of the optically pumped VCSELs, these

drops could unambiguously be assigned to the transit of the acoustic pulse through the QD layer. The long-lived nanomechanical vibrations also resulted in both cases in remarkable harmonic intensity modulations with amplitudes of up to 15 %.

The most noteworthy difference between the freestanding optically excited and the polymer-surrounded electrically driven VCSELs was the number of simultaneously excited modes. While in VCSEL E1 only three extensional modes were vibrating at a time, up to eight extensional modes were simultaneously excited in VCSEL O1 [2]. Most probably, higher order modes are strongly damped in electrically driven VCSELs because of the contact with the polymer.

The experiments showed that the response of a micropillar laser is not so much determined by the pumping scheme but by its acoustical environment. The spectrum of the excited modes appears rather unpredictable beforehand and even nominally identical micropillars showed a totally different response to the acoustic excitation. This sensitivity towards the acoustic environment might also turn out to be an advantage: in the case of electrically pumped micropillars for example, the found modulation might be useful for the characterization of the contact between the polymer and the micropillar, for which otherwise X-ray images or cross-sectional cuts are required.

[2] This observation holds also true for the many not shown electrically and optically pumped VCSELs

Chapter 7

Conclusion and Outlook

Picosecond ultrasonics were used in this part of the thesis for the emission modulation of VCSELs. Lasers with various designs were studied with the intention to find out how different realizations of the basic laser components can be exploited for an ultrafast and efficient laser emission modulation.

Planar microcavity lasers with an inhomogeneously broadened QD ensemble, on the one hand, and groups of homogeneously broadened QWs, on the other hand, were studied. The different choice of the active medium strongly influences the interaction with coherent phonons. In the case of the homogeneously broadened QWs, the picosecond acoustic pulse modulated the detuning with respect to the cavity mode, which in turn influenced the laser efficiency. The optical gain depends nonlinearly on this detuning and strong amplifications and quenchings of the emission intensity were found, when the initial detuning was decreased or increased, respectively. The experiments have shown that the perturbation is adiabatic and the laser intensity evolution could be linked to the time profile of the applied strain; if the strain is small enough ($\sim 10^{-4}$), an even linear relation was found.

The research showed that a more complex interplay needs to be considered for the inhomogeneously broadened QD ensemble. Most of the QDs trap the electrons in states off-resonant with the cavity and therefore form an highly excited reservoir. This becomes accessible for the light field when applying strain. A theoretical model for the QD laser including the coherent phonon perturbation was developed, to evaluate, if this off-resonant reservoir needs to be accounted for or if the QDs basically behave like the QWs. To validate the model, experiments were performed, in which the relative emission modulation was recorded for various detunings and pump powers. The curves showed an up to tenfold amplification and almost complete quenching of the laser emission on picosecond timescales. These findings were well reproduced by the model. The relative contribution of the adiabatic response and the transient shaking effect that were indistinguishable in the experiment could be investigated separately by the model. The analysis showed that even for a vanishing initial detuning, a net intensity increase by

almost 50 % is achieved when applying fast mechanical vibrations. This finding proved that transient effects indeed play an important role in inhomogeneously broadened gain materials and can be exploited for an ultrafast intensity amplification of VCSELs.

Planar microcavities with mechanical resonances emerging from the DBRs and moreover micropillar resonators with additional nanomechanical eigenmodes due to the pillar geometry were studied as laser resonators. The injection of the picosecond acoustic pulse launched the acoustic eigenvibrations in the experiments. In planar microcavities, the transit of the acoustic pulse through the active area could well be monitored. Moreover, long-lived resonances associated with the acoustic stop band edges of the DBRs were excited. These eigenvibrations led to a remarkable modulation of the laser intensity with frequencies of up to 40 GHz, an amplitude of 10 %, and a lifetime longer than 1 ns, even at room temperature. This fast modulation can unfortunately not be used as a direct way to modulate lasers in a controlled manner, since the vibrations cannot be switched on and off at will. Nevertheless, the experiment proved that in principle VCSELs can be operated faster than in present commercial technology, which relies on a modulation of the pump current. In micropillar VCSELs only the nanomechanical extensional and breathing eigenmodes with frequencies below 10 GHz were excited by the acoustic pulse. Whether radial or longitudinal motion was started, crucially depended on the contact of the micropillar with its acoustic environment. No fingerprints of DBR modes with higher frequencies were found. It will be shown later in chapter 10 that not the limited time resolution of the streak camera prevented the detection of these faster modes, but that there is a cut-off frequency for phonons that may enter micropillars. For the perspective of a fast and efficient laser modulation, planar microcavity structures are definitely favorable, since the microcavity modes are faster and the spectrum of excited modes is much more deterministic.

The pump excitation scheme was shown not to directly influence the response of micropillar VCSELs to picosecond acoustic pulses. However, in electrically pumped VCSELs less nanomechanical modes than in freestanding micropillars were excited, likely due to the polymer surrounding. Further experiments with planar lasers should be conducted to prove that electrical pumped VCSEL can not only be modulated by micropillar eigenmodes, but also by the faster vibrations supported by the DBRs.

There are several ideas for future experiments to refine the design of VCSELs in order to add more functionality to the emission modulation. In this thesis, only the intrinsic ability of the optical mirrors to reflect phonons was exploited so far. The frequencies of the acoustic resonances were predetermined by the wavelength of the optical mode. One way to enhance the VCSEL design is to incorporate a DBR structure into the resonator, which is dedicated exclusively to phonons. In the proposed new design, the λ-cavity spacer of the optical cavity is replaced by a finer structure; this consists of two purely acoustic DBRs and one acoustic cavity spacer and forms a complete acoustic microcavity on its own. The layer thicknesses of the acoustic DBRs have to be much shorter than

the photonic wavelength (∼5 nm), such that the acoustic microcavity can be treated as a uniform layer with an averaged refractive index for the confined light field. The length of the whole acoustic microcavity sandwiched between the thick optical DBRs must sum up to an optical λ-cavity; the acoustic cavity spacer sandwiched between the two thin acoustic DBRs must be equal to an 3/2-λ-cavity for phonons. In the center of the structure, the light field intensity possesses an anti-node, while the displacement possesses a node (and the strain field consequently an anti-node). The coupling of heterostructures to photons and phonons is simultaneously optimized at this position. By choosing the layer thicknesses of the acoustic DBRs, the phononic resonances can be tailored independent from the optical properties. In structures made from AlAs/GaAs, phonons with frequencies of up to 1 THz can be confined inside an optical λ-cavity for near-infrared light [129], which would allow a much faster laser modulation than observed in this thesis up to now.

In future experiments it can be possible to selectively excite phonons with a single frequency instead of broad band picosecond acoustic pulses. This is useful when any kind of acoustic resonances shall be addressed. The metal film featuring a short optical absorption length needs to be replaced by a superlattice made from one absorbing and one transparent material [137]. In the superlattice, only the opaque material will be heated up and expand, such that the periodicity of the superlattice is imprinted onto the spatial displacement distribution. The repetition rate of the excitation laser needs to match the frequency of the phonon with the wavelength that corresponds to this periodicity.

Electrically pumped optomechanical resonators bear huge potential for new electrically driven sources of coherent sound radiation - the so-called sasers. The stimulated emission of phonons is mediated by the active medium, for example a single QD: every time an electron-hole pair recombines due to lasing, phonons with a spectrum defined by the length scale of the QD are emitted [135]. The acoustic mirrors can be designed to reflected these phonons back at the QD. Arriving at the QD, the phonons trigger the recombination of the next electron-hole-pair due to lasing, given that the QD is initially detuned from the cavity. This way, each passage of phonons through the gain materiel would create more phonons and a stable acoustic field may build up. Electrically pumped sasers with these frequencies would be useful for ultrasound imaging techniques able to resolve nanometer-scaled objects.

Last but not least, single-photon sources that are acoustically driven with GHz frequencies should be mentioned as an outlook. Single QDs might be shifted in and out of resonance with a cavity mode by resonant acoustic vibrations. Every time the strain field establishes resonance, the QD emits a photon due to the Purcell effect. Thereby a train of identical single photons is generated. This can be realized for example in micropillars, which offer a high indistinguishability of 99 % and an extraction efficiency of 66 % [41].

Part III

Nanoscopy of Semiconductor Heterostructures

Introduction

The term nanoscopy refers to an imaging/metrology technique that allows for measurements with nanometer accuracy. In the previous part of the thesis, it was shown that this is the length scale for most components of VCSELs: the heterostructures serving as the active medium, namely QWs and QDs, are nanometer-sized objects and so is the thickness of the layers forming microcavities for visible to near-infrared light. Deviations from the nominal thicknesses by only a few nanometer strongly affect the efficiency of such a laser; either via a detuning or misplacement of the active medium with regard to the photonic mode's energy or light field anti-nodes, respectively. Also for other photonic devices an exact knowledge of the geometry is important to assess their performance, in particular for challenging applications that require to reach the strong coupling regime [113].

Nowadays, there are many suitable nanoscopy methods and one can choose the most fitting for the desired task. If surfaces shall be mapped, one may use atomic force microscopy. This technique provides surface reliefs with nanometer precision [15]. Another possibility to image surfaces is to use scanning electron microscopes (SEM). Modern scanning electron microscopes offer nanometer precision and below [64]. If also depth information is required, one may cut the sample and image its cross-section by SEM. Although the sample is destroyed, this approach is the often the most practical way to go owing to the relatively straight forward operation and the easy to interpret data. However, sometimes cross-sectional cuts are not available or would damage the sample so much that the structure of the specimen is lost, for example in the case of biological cells. In this case, one has to rely on non-invasive methods. Among these methods X-ray imaging and ellipsometry are most prominent. Both of these methods suffer from drawbacks, which restrict their versatility. X-ray imaging is based on interpreting an interference pattern that requires different electronic densities in the various layers for a good contrast. Structures composed of materials with a similar electron density appear as uniform blocks. Moreover, X-ray imaging is very sensitive to the interface quality [139]. If non-lattice matched materials are grown on top of each other and the interface quality is bad, the interference signal might blur out. Ellipsometry is another powerful tool for the metrology of layered structures. Here, the polarization change of light being

transmitted through and reflected from the specimen is recorded for various angles and wavelengths. From the obtained information and with knowledge of the optical properties of the sample, the underlying structure can be recalculated. This technique is widely used during the growth of layered structured by MBE. Usually, each new layer is characterized right after its growth and its thickness is used as the only unknown parameter to fit the calculations to the recorded data. If a multilayered structure is investigated for which no information is available beforehand, several layer thicknesses are unknown and enter the model as free parameters. The solution becomes the more ambiguous, the more layer thickness need to be determined, and ultimately the method fails.

Another non-invasive nanoscopy method with depth resolution is ultrasound imaging. This technique is the technological standard for in-vivo investigation in medical applications. The sound wave is generated by piezoelectric transducers. Similar to surface acoustic waves, the frequency of the applied voltage determines the frequencies of the sound wave. The sound wave is send into the specimen and focused either by an acoustic lens or by beam shaping at the desired depth. Echoes of the incoming sound wave originate from everywhere where the acoustic impedance is changing. These echoes are recorded by the same electrical transducers used for the generation process [27]. For standard medical investigation, phonon frequencies up to 50 MHz are employed. The highest spatial resolution for more advanced research, e.g. for the investigation of single cells, is achieved by acoustic microscopes with a maximum phonon frequency of 2 GHz [17]. These phonons allow to reach an accuracy of a few micrometers, depending on the exact sound velocity inside the specimen.

For the characterization of nanometer-scaled photonic devices one has to employ sub-THz phonons with shorter wavelengths. Picosecond ultrasonics provide the only suitable framework for the generation of coherent phonons with such frequencies, since piezoelectric transducers reach their technological limit around 30 GHz [108, 67]. Indeed, picosecond ultrasonics have been extensively used for the 3D-imaging of biological cells [36, 101, 39], nano-crystals [61], and for the characterization of thin films [77]. The technique has recently left the scientific stage and is now commercially offered by the french company *Menapic*.

In order to resolve the arrival times of echoes originating from internal interfaces with a distance on the order of nanometers, the detection must provide a sufficient temporal resolution. The necessary resolution is determined by the speed of sound and in the order of picoseconds for most materials. Most electronics are not fast enough to work with signals so short and another detection scheme has to be employed. The first pioneering work on picosecond ultrasonics from 1986 has already presented a way to optically detect acoustic pulses with sub-picosecond laser pulses [128]. The idea is to record the reflectivity of the sample: every acoustic echo arriving at the surface locally changes the optical properties and therefore modulates the intensity of the reflection originating from there. However, the reflectivity modulation depends on a lot of param-

eters, among these are for example the penetration depth of the chosen probe wavelength and the coupling between the mechanical strain and the refractive index. Especially for light that is weakly absorbed by the structure and also reaches buried layers, it is not straight forward to interpret the reflectivity modulation. Often, a sophisticated theoretical analysis is required to understand the signals and deduce information about the layer thicknesses. There are nevertheless specially designed strain detectors, which can be used to minimize this effort and to obtain the strain profile relatively easily.

This part of the thesis focuses on nanoscopy experiments involving picosecond ultrasonics and an all-optical sound detection scheme. It starts with chapter 8, where the fundamental theory about acousto-optical interactions is revised. A method is presented to calculate the reflectivity modulation of a photonic device while a picosecond acoustic pulse propagates inside. With this theoretical background in mind, an ultrafast and efficient strain detector is presented and analyzed in chapter 9. This strain detector is based on a single QW made from cubic GaN, which is able to map the strain profile passing through. In chapter 10, the method of acoustic nanoscopy is expanded to an acousto-optical nanoscopy. The idea is not to characterize the studied structure with the help of acoustic echoes arriving at a certain position, but with the help of a deeply-penetrating light field. A probe wavelength is chosen, which reaches all buried layer junctions, such that a reflected beam originates from every internal interface. While the acoustic pulse propagates through the specimen, it sequentially passes each layer and thereby modulates the reflection originating from there. A unique interference pattern is recorded, that can be used to reconstruct the underlying light field distribution. The calculations do not only yield the light field distribution itself, but also automatically provide the layer thicknesses based on Maxwell's equations. The chapter starts with detailing the theoretical background of the acousto-optical nanoscopy and afterwards the method is applied to a slow-light mode of an AlAs/GaAs micropillar resonator.

Chapter 8

Acousto-Optic Interactions

Already in the first successful experiment with picosecond ultrasonics in 1986, the picosecond short acoustic pulses were detected with pulsed lasers [128]. An optical detection scheme is quite natural, because the generation process of the acoustic pulses, on the one hand, already involves sub-picosecond laser pulses, which, on the other hand, also provide a sufficient time resolution. Usually, nanoscopy experiments with picosecond acoustic pulses are all-optically realized in time-resolved pump-probe setups; the pump beam is used to generate the acoustic pulse and the reflection of the probe beam from the sample is recorded to monitor its propagation.

By tuning the employed laser wavelength either into the absorption or transparency region of the acoustic medium, the acoustic pulse is probed at the surface only or also tracked inside volume material, respectively. In the early experiments following the initial demonstration, the reflectivity modulation of bulk materials was observed. The profile shows a characteristic oscillation pattern originating from the dynamic interference of two parts of the probe beam. One part is reflected from the surface of the sample and the other from the depth of the material: here, a part of the light transmitted through the surface is reflected from the acoustic pulse, where the optical properties are locally perturbed due to the mechanical strain. While the acoustic pulse is propagating towards or back from the sample surface, the phase difference between these two beams is alternating and the so-called coherent Brillouin-oscillations are observed. From their frequency information about the refractive index and the sound velocity of the studied volume material is deduced [127].

Coming from these rather simple beginnings, picosecond ultrasonics were used for the nanoscopy of more complex devices. Often layered planar photonic devices with layer thicknesses down to a few nanometers were investigated, whose reflectivity exhibits strong modulations when the probe wavelength is close to an optical resonance [131]. In such layered structures also the acoustic pulse propagation is more complicated and any proper theoretical treatment of the acousto-optical interactions must include the acoustic reflections (and multireflections) originating from the internal interfaces. In

recent years, a comprehensive theoretical description has been developed for the propagation of picosecond acoustic pulses through and their optical detection in planar layered structures [80].

Before addressing the results of the nanoscopy experiments presented in this part of the thesis, the basic theory is shortly outlined in this chapter. At first, the transfer-matrix method is introduced, which allows to determine the acoustic and optic properties of the studied structure. These are the reflectivity and the field distributions for phononic and photonic modes. Moreover, the temporal displacement and strain profile at every position inside the structure after the injection of an arbitrary acoustic pulse can be calculated by this method. In the second section, the different mechanisms by which the acoustic pulse perturbs the optical properties of a photonic device are discussed. These are namely (i) the photoelastic effect that links mechanical strain to a modulation of the refractive index and (ii) the interface displacement, which relates the movement of internal interfaces to a characteristic interference pattern. Finally, these two mechanisms are included as a perturbation in the optical transfer-matrix of the sample to calculate the reflectivity modulation in the presence of an acoustic pulse.

8.1 Transfer-Matrix Method

The transfer-matrix method is a powerful tool to easily calculate electric or acoustic field distributions inside layered structures. In the following, the transfer-matrix method is presented for optics, but the concept can very easily be transferred to acoustics by substituting photon characteristics with their phononic counterparts, e.g. speed of light with sound velocity. In the transfer-matrix approach, light or acoustic pulses are decomposed into their frequency spectrum and each frequency is treated independently. Consider the structure shown in Fig. 8.1 (a) that consists of N layers, which are denoted by an index $j = 1, 2, \ldots, N$ starting from the front surface. Two semi-infinite layers - labeled i for initial and f for final - enclose the structure. In each layer, the electric field $E_{j,\omega}(z)$ can be written as a superposition of a right- and a left traveling wave

$$E_{j,\omega}(z) = E^{+}_{j,\omega} \exp\left[i\left(k_{j,\omega} z - i\omega t\right)\right] + E^{-}_{j,\omega} \exp\left[-i\left(k_{j,\omega} z + i\omega t\right)\right], \tag{8.1}$$

where the wavevector equals $k_{j,\omega} = \frac{n_j \omega}{c}$ and n_j is the refractive index in the j-th layer. The time dependence as well as the index ω will in the following be omitted for simplicity. The amplitudes of the two counter-propagating plane waves E^{+}_{j} and E^{-}_{j} are stored in a two component vector $\vec{E}_j$ that is assigned to every layer. The initializing amplitudes at the left side of the front surface are given by $\vec{E}_i = \left(E^{+}_{i}, E^{-}_{i}\right)^{\mathrm{T}} = \left(1, r\left(\omega\right)\right)^{\mathrm{T}}$; i.e. the amplitude of the incident electric wave is normalized to 1, while the structure's complex reflection coefficient $r(\omega)$ determines the amplitude and phase of the reflected wave. A 2×2 interface matrix $I_{j \to j+1}$ links the amplitudes on the left and on the right side of the

interface between the layers j and $j+1$ with each other

$$\begin{pmatrix} E_{j+1}^{+} \\ E_{j+1}^{-} \end{pmatrix} = \underbrace{\frac{1}{2}\begin{pmatrix} 1+\frac{n_j}{n_{j+1}} & 1-\frac{n_j}{n_{j+1}} \\ 1-\frac{n_j}{n_{j+1}} & 1+\frac{n_j}{n_{j+1}} \end{pmatrix}}_{=I_{j\to j+1}} \begin{pmatrix} E_{j}^{+} \\ E_{j}^{-} \end{pmatrix}. \tag{8.2}$$

The entries reflect the Fresnel equations for light of perpendicular incidence. The propagation through a layer j is accounted for by a propagation matrix P_j given by

$$P_j = \begin{pmatrix} \exp\left(+i\varphi_j(\omega)\right) & 0 \\ 0 & \exp\left(-i\varphi_j(\omega)\right) \end{pmatrix}, \tag{8.3}$$

which basically appends a phase $\varphi_j(\omega) = \frac{d_j n_j}{c}\omega$ to the plane waves, where d_j is the thickness of the layer. Every planar layered structure can be described by a transfer-matrix M that is a product of interface and propagation matrices. This matrix links the electric field on the front surface with the final one on the other side of the structure that is given by $\vec{E}_f = (t(\omega), 0)^{\mathrm{T}}$, where $t(\omega)$ is the transmission coefficient. The structure transfer-matrix M is defined by

$$\begin{pmatrix} t(\omega) \\ 0 \end{pmatrix} = \underbrace{I_{N\to f} P_N \left(\prod_{j=1}^{N-1} I_{j\to j+1} P_j\right) I_{i\to 1}}_{=M^{-1}} \begin{pmatrix} 1 \\ r(\omega) \end{pmatrix}. \tag{8.4}$$

From these linear equations, one can easily deduce the complex reflection and transmission coefficients $r(\omega) = \frac{M_{21}}{M_{11}}$ and $t(\omega) = \frac{1}{M_{11}}$, respectively, as well as the total reflectivity $R(\omega) = |r(\omega)|^2$ and transmissivity $T(\omega) = 1 - R(\omega)$. The field distribution for each frequency inside the structure can be recalculated from the amplitudes stored in $\vec{E}_j$. In the case of periodic structures like DBRs, the transfer-matrix can be used to calculate the dispersion of the folded wavevector of light $q(\omega)$. For an infinite superlattice with layer thicknesses d_{A} and d_{B} one finds via the Floquet theorem

$$\cos(qD) = \cos\left(\omega\frac{d_{\mathrm{A}}n_{\mathrm{A}}}{c}\right)\cos\left(\omega\frac{d_{\mathrm{B}}n_{\mathrm{B}}}{c}\right) - \frac{1+\delta^2}{2\delta}\sin\left(\omega\frac{d_{\mathrm{A}}n_{\mathrm{A}}}{c}\right)\sin\left(\omega\frac{d_{\mathrm{B}}n_{\mathrm{B}}}{c}\right), \tag{8.5}$$

where $D = d_{\mathrm{A}} + d_{\mathrm{B}}$ is the superlattice periodicity and $\delta = \frac{n_{\mathrm{A}}}{n_{\mathrm{B}}}$ [122]. An example for the dispersion inside a superlattice is discussed in detail in chapter 5.

So far, transfer-matrices are only used to calculate static features. The method can be expanded for the simulation of temporal displacement field profiles $u(z,t)$ or electric field profiles $E(z,t)$ at any position inside the structure after the injection of an arbitrary input pulse. For any position z, one can introduce a matrix $T(z)$ that links the final

electric field $\vec{E}_f$ with the amplitudes at the position z

$$\begin{pmatrix} \widetilde{s}^{+}(z,\omega) \\ \widetilde{s}^{-}(z,\omega) \end{pmatrix} = T(z) \begin{pmatrix} t(\omega) \\ 0 \end{pmatrix} \tag{8.6}$$

and yields the so-called scattering states $\widetilde{s}(z,\omega) = \widetilde{s}^{+}(z,\omega) + \widetilde{s}^{-}(z,\omega)$ [63]. These scattering states form a complete and orthogonal set of eigenfunctions for the layered structure [45]. The temporal evolution of an input pulse $E(z, t = 0)$ can be calculated in the basis of the scattering states via

$$E(z,t) = \int d\omega g(\omega) \widetilde{s}(z,\omega) \exp(i\omega t). \tag{8.7}$$

Here, $g(\omega)$ is the scalar product of the input pulse $E(z, t = 0)$ with the orthogonal set of basis functions $s(z,\omega)$ that the scattering states form. It is important to stress that this calculation becomes really easy if the light pulse is initially located far away from the structure, because $g(\omega)$ can very well be approximated by the spatial Fourier-transform $\widetilde{E}(k)$ of the input pulse in this case: $g(\omega) \approx \widetilde{E}(k(\omega))$.

All considerations can be applied to acoustics one-to-one by substituting (i) the electric field by the displacement $E \rightarrow u$, (ii) the speed of light by the sound velocity in the phase accumulation for the layers $\varphi(\omega) = \frac{dn}{c}\omega \rightarrow \frac{d}{v}\omega$, and (iii) the refractive index by the acoustic impedance in the interface matrices $n \rightarrow Z$. When the strain profile $\eta(z,t)$ shall be found, the displacement profile $u(z,t)$ needs to be numerically derived with respect to z and therefore must be calculated for at least two positions.

In the nanoscopy experiments performed in this part of the thesis, the transit of acoustic pulses through photonic devices is tracked by monitoring the optical reflectivity $R(t)$ with a femtosecond laser. The presented transfer-matrix method allows one to calculate the spatio-temporal strain and displacement profiles $\eta(z,t)$ and $u(z,t)$ of the injected acoustic pulse. The next section will explain, how these profiles can be included in a perturbed optical transfer-matrix to obtain the time-depended optical reflectivity $R(t)$. The mechanisms by which the acoustic pulse alters the optical properties of the studied structures are reviewed to this purpose at first.

8.2 Photoelasticity and Interface Displacement

The photoelastic effect couples the strain in a medium to a change of the index of refraction. In strained crystals, there are manifold physical origins of this effect like shifts of the electronic band structure, new orientations of electronic atom shells, or piezo-electricity. The most prominent application is related to the fact that strain may turn optically isotropic materials anisotropic and therefore makes birefringence occur. From studying the birefringence pattern of structures, one can measure the internal strain distribution of complex geometries.

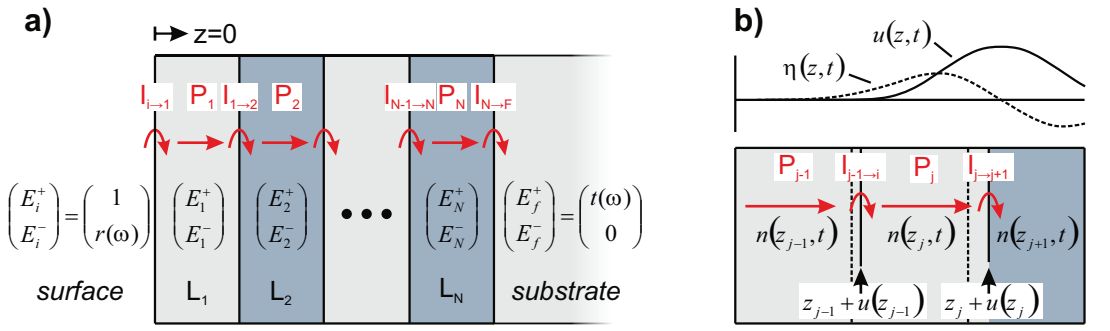

Figure 8.1: Transfer-matrix method. Panel (a): Transfer-matrix in an unperturbed multilayered structure. The electric field is incident on the left side and transferred to the right side by a successive multiplication with propagation and interface matrices. Panel (b): Calculation of a transfer-matrix including a picosecond acoustic pulse as a perturbation. Each layer is sub-divided into several grid points, which must be so closely spaced that they can spatially raster the evolution of the strain $\eta(z,t)$ and displacement $u(z,t)$. The refractive index and the position of each grid point is manipulated by the strain and displacement field.

The dielectric function is given by a second rank 3×3 tensor ϵ in anisotropic materials. The relation between the change of the dielectric tensor for photons with a given energy E in presence of mechanical strain is described by the phenomenological fourth rank photoelastic tensor $p(E)$

$$\Delta\left(\frac{1}{\epsilon(E)}\right)_{ij} = \sum_{ijkl} p_{ijkl}(E)\eta_{kl}. \tag{8.8}$$

The number of independent entries of $p(E)$ is reduced in crystals due to symmetries. In the zinc-blende crystals GaAs/AlAs and Al/GaN studied here, only 3 non-vanishing independent components remain [138]. These semiconductors are moreover optically isotropic and thus ϵ becomes a scalar. The number of indices in Eq. (8.8) is further reduced because the acoustic pulse does only exert uniaxial strain along one direction, such that only η_{zz} needs to be considered. For these conditions, one photoelastic coefficient $p(E)$ is sufficient to describe the change of the refractive index. However, the detailed dispersion of $p(E)$ is generally not even for this most simple case available for the whole range of studied photon energies.

Here, the optical reflectivity of semiconductors is probed with photon energies close to the band gap, where the photoelastic effect mainly originates from shifts of the electronic band structure. The change of the complex index of refraction $\tilde{n} = n + i\kappa$ can well be

approximated in this spectral range by

$$\Delta\widetilde{n} = \frac{\partial\widetilde{n}}{\partial E}\frac{\partial E}{\partial \eta}\eta = \underbrace{\left(\frac{\partial n}{\partial E} + i\frac{\partial \kappa}{\partial E}\right)\frac{\partial E}{\partial \eta}}_{=p(E)}\eta, \tag{8.9}$$

where $\frac{\partial E}{\partial \eta}$ is the deformation potential for electrons and holes [cf. Eq. (4.1)], while $\frac{\partial n}{\partial E}$ and $\frac{\partial \kappa}{\partial E}$ are the dispersions of the refractive index n and the optical extinction coefficient κ, respectively [12]. These two dispersions fully determine the dependence of the photoelastic coefficient $p(E)$ on the photon energy, since the deformation potential is constant.

The acoustic pulse may manipulate the refractive index in a homogeneous bulk medium at its momentary position. This local perturbation becomes observable in the optical reflectivity $R(t)$, if the probe wavelength can penetrate through the medium to the position of the acoustic pulse; i.e. the acoustic pulse can be observed only within the optical absorption length. The presence of the acoustic pulse manifests itself in the coherent Brillouin-oscillations mentioned in the introduction, which appear due to the interference of the reflection originating from the front surface and from the acoustic pulse. Whether their interference is constructive or deconstructive, depends on the distance of the acoustic pulse from the surface. While the acoustic pulse propagates towards or back from the surface, $R(t)$ therefore oscillates with a frequency given by

$$f_B = \frac{2v}{\lambda}\sqrt{n^2 - \sin(\theta)}. \tag{8.10}$$

In this equation, θ is the incident angle of the probe light wave on the sample surface. The same equation can be derived from the momentum conversation, when one assumes that an incident photon with vacuum wavelength λ is back-scattered from a phonon with a frequency of f. In a homogenous bulk material, these harmonic oscillations - plus an envelope defined by the absorption length - are the only modulation of $R(t)$.

In layered structures, another contribution that is related to a displacement of material interfaces needs to be taken into account. The optical reflectivity $R(t)$ is determined by the intensity of the beam being reflected by the whole structure. This beam is composed of all the beams being reflected from the numerous interfaces of the structure, either originating from the surface or from the internal interfaces. The acoustic pulse moves an interface when passing it. Its displacement is translated into a phase shift of the reflection originating from there with respect to all other unperturbed reflected beams. This phase shift becomes observable in the total reflectivity $R(t)$ due to a modulation of the interference terms. The resulting modulation of the reflectivity depends on many things, for example on the position of the moved interface, its dielectric function contrast, and the phase difference of its reflection relative to the numerous others reflected beams. Regarding the last point, one has to mention that in many cases the most dominant interference term is the one between the reflection from the surface and the moved

interface. Please note that in optical resonators the reflectivity modulation $R(t)$ is also accompanied with a modulation of the photonic resonances, as described in chapter 5 and chapter 6.

Both acousto-optical mechanisms (photoelasticity and the interface displacement effect) can be included in an optical transfer-matrix for the numerical simulation of $R(t)$. To this end, the different layers of the studied photonic device are divided into a smaller sub-grid, such that the distance between the grid points is short enough to sample the dynamics of the acoustic pulse. This depends on the highest occuring phonon frequency and typically requires an accuracy of $\sim$0.1 nm. The scheme is illustrated in Fig. 8.1 (b): to each grid point j at a position $z_j(t)$, a propagation matrix $P_j(t)$ and an interface matrix $I_{j\to j+1}(t)$ is assigned. These matrices include the perturbation induced by the acoustic pulse. The phase $\varphi_j(t)$ in the propagation matrix $P_j(t)$ is given by

$$\varphi_j(t) = \frac{[z_{j+1}(t) - z_j(t)]\, n_j(t)}{c}\omega, \tag{8.11}$$

where the initial position of the sampling point z_j^0 and the initial refractive index n_j^0 are modulated via $z_j(t) = z_j^0 + u(z_j^0, t)$ and $n_j(t) = n_j^0 + p(E)\eta(z_j^0, t)$, respectively. The interface matrix from one grid point to the next $I_{j\to j+1}(t)$ becomes time-dependent by inserting $n_j(t)$ and $n_{j+1}(t)$. Please mind that it is important to catch the internal material interfaces with a grid point for a proper description of the interface displacement effect. Therefore, it is advantageous not to take equidistant sampling points, say every 1 nm, but to strictly assign a sampling point to every material interface. The complete perturbed transfer-matrix is obtained from multiplying the grid matrices $P_j(t)$ and $I_{j\to j+1}(t)$ in the same manner as in Eq. (8.4).

In general, both acousto-optical mechanism lead to a modulation of $R(t)$ in layered structures because strain (responsible for the photoelastic effect) and displacement (leads to the interface displacement effect) are mutually dependent on each other and one of them does not occur without the other. In the following, it will be shown that it is possible to tailor the experiment such that one of the two acousto-optical mechanisms becomes the dominant contribution. If this is achieved, the response of $R(t)$ couples exclusively to either the mechanical strain or to the displacement and the two mechanisms do not interfere with each other. Often, this makes the found response more unambiguous and much easier to interpret.

In the next chapter, a single QW made from cubic GaN serves as an ultrafast and efficient detector for strain. This is achieved by choosing an optical probe wavelength where the dispersion is particularly steep, which goes hand in hand with a high photoelastic coupling constant $p(E)$. On the opposite, the interface displacement effect governs the reflectivity modulation when the dispersion is flat, for example, if the photon energy is in the transparency region far enough from any resonance. Under these circumstances,

one can deduce useful information about the positions of the internal interfaces from the reflectivity modulation. In chapter 10, this idea is elaborated in more detail and used for the acousto-optical nanoscopy of a micropillar resonator.

Chapter 9

Cubic GaN Single Quantum Wells as Ultrafast Strain Detectors

One key element of nanoscopy experiments with picosecond ultrasonics is the detection of the acoustic echoes, from whose arrival times information about a hidden or buried structure are obtained. There are several criteria the detection scheme must meet in order to conserve the high spatio-temporal resolution that the picosecond acoustic pulses provide. First of all, the strain pulse needs to be detected in a small volume or area. In a bulk-like material, the presence of the acoustic pulse becomes visible in the reflectivity modulation as coherent Brillouin-oscillations, but these yield no straight forward information on where the acoustic pulse is actually located. Therefore, it is important that only a limited volume is sensitive to the strain pulse. Ideally, the detector is able to raster the profile of the acoustic pulse passing through. This requires volume thickness in the propagation direction on the order of nanometers. The second important point is that the detector material must respond to strain on a picosecond timescale not to lose the high temporal accuracy of the acoustic pulses.

There are several realizations for a detection scheme that fulfill these requirements. One idea is to electrically detect sound. The approach is based on p-n-junctions or Schottky diodes, where the transit of picosecond acoustic pulses through the depletion zones leads to a measurable current [29, 85]. In this scenario, the depletion zone is the limited volume. Only signal rise times longer than 30 ps have been reported so far, because the bandwidth of the employed read-out electronics was below 12.5 GHz [85]. Besides the electronics, also the capacitance and inductance of the diodes need to be improved to make the all-electrical detection of sub-THz phonons become feasible. A second strategy is an all-optical detection. This can be achieved by monitoring the reflectivity of the studied sample by probe lasers, like discussed in the previous chapter. In order to define a fixed detection volume, one can rely on a laser with a short absorption length and detect the acoustic pulse near the surface of bulk-like materials [128, 10].

When also depth information is required, one relies on thin buried layers. In order to achieve a good spatial resolution in this case, the layers must be as thin as possible and therefore most commonly QW structures are used nowadays [81, 85]. The transit of the acoustic pulse through these thin layers can be tracked due to the interface displacement and the photoelastic mechanism. Since the barriers enclosing the QW have higher band edges per design, their electronic resonances and also the dispersion of the refractive index are significantly different. Given that the probe wavelength is chosen properly, the photoelastic mechanism in the QW may exceed the one of the adjacent barriers by orders of magnitude. All-optical detection schemes often rely on photoelasticity for that reason [10]. Another rarely employed approach is based on recording spectral shifts of the PL of heterostructures, while an acoustic pulse passes through. This method requires fast real-time detection devices like streak cameras, which are often not available, though [108, 2].

If one compares the electrical and optical approaches, one finds that both schemes have their advantages. An all-electrical detection does not require picosecond-laser radiation, which is a big plus when the sound waves are generated electrically. Even with the fastest electronics, the thickness of the detection layer puts an upper limit to the best possible spatial resolution; the thinner the layer, the faster the resolution. From all electrical detection schemes, Schottky diodes offer the best spatial resolution. The thickness of their depletion zone is about 50 nm to 150 nm, depending on the applied forward-bias [85]. Optical detection schemes easily beat this value, with optical absorption lengths and QW thicknesses in the range of a few nanometers. Moreover, the generation of picosecond acoustic pulses already requires sub-picosecond lasers anyway such that this is the naturally preferred detection scheme in most nanoscopy experiments.

In this chapter, a single QW made from AlN/GaN is shown to be an efficient and ultrafast optical strain detector when using UV light. The GaN QW is operated with UV light, while conventional QWs made from Si or GaAs, for example, are most sensitive for near-infrared light. This shorter optical wavelength does not result in a better spatial resolution of the nanoscopy, because the accuracy is determined by the spatial extent of the acoustic pulse. However, it is useful to work with UV light if one wants to restrict the sound detection to an area close beneath the surface. In most semiconductors the absorption length of UV light is orders of magnitude shorter compared to near-infrared light. In this case, the probe light does not reach buried interfaces, where the transit of the acoustic pulse might yield unwanted artifacts in the reflectivity modulations.

The group of III-nitrides crystallize either in the stable hexagonal wurtzite phase or in the metastable cubic zinc blende phase. Multiple QWs made from **h**exagonal AlN/GaN (h-AlN/h-GaN) were already used for the detection and generation of coherent THz phonons by exploiting the strong piezoelectricity of the wurtzite phase [116]. Here, the **c**ubic phase of AlN/GaN (c-AlN/c-GaN) that lacks any piezoelectricity is studied. The

main advantage of the cubic phase compared to the hexagonal phase is related to the possibility to grow heterostructures, in which the intrinsic strain is not accompanied by built-in electric fields. These internal fields separate electrons and holes and prevent them from recombining. In GaN/AlN QDs for example, the recombination rate was found to be two orders of magnitude slower in the wurtzite than in the zinc blende phase [112]. Another plus of the cubic phase is that it can be integrated into Si or GaAs based structures.

Recent experiments with bulk c-GaN and UV light have shown coherent Brillouin-oscillations, which suggests that the photoelastic coupling in the material is in principle sufficient for an optical detection scheme [84]. The experiments performed here shall validate whether it is possible to optically resolve short acoustic pulse with c-GaN QWs; i.e., if the optical response of the c-GaN QW on the acoustic pulse can be separated from the one of the neighboring c-AlN barriers and c-GaN buffer layers.

In the first section, the studied QWs are shortly described along with the experimental setup used to record its optical reflectivity during the transit of an acoustic pulse. The obtained reflectivity modulation for two QWs with different barrier heights is presented afterwards. In addition, transfer-matrix simulations are performed to model the reflectivity modulation. The strength of the photoelastic coupling constant is extracted from the simulation to evaluate the potential of c-GaN QWs for ultrafast strain detection. Many of the presented results have been published in Ref. [31].

9.1 Single c-GaN QWs and Experimental Setup

The hexagonal wurtzite and the cubic zinc blende crystal structure of group III-nitrides are both grown by MBE. The growth of the metastable zinc blende phase is for GaN only possible in a very narrow window of processing parameters and enforced by using an almost lattice matched 3C-SiC substrate. An optimization of the growth is possible by monitoring the amount of excess Ga during the growth and adjusting the flux accordingly. By doing so, a minimal surface roughness of 2.5 nm was achieved in the fabrication of c-GaN bulk layers [107]. It should not be concealed that owing to the lattice constant mismatch of many cubic III-Nitrides, the growth of heterostructures is troublesome up to now. The interface quality often suffers from a high roughness, which cannot be annealed by further increasing the substrate temperature, because at some point the metastable phase breaks up. In c-AlN/GaN superlattices for example, broad intersubband transition are observed as a result of the inhomogeneities [75]. More details on the growth process of GaN/AlN-based heterostructures can be found in Ref. [6].

The studied QW structures are provided by the group of D. J. As from the University of Paderborn. A SEM image is shown in Fig. 9.1 (a). The samples are grown on a (100)-Si substrate, which was polished down to a thickness of 90 µm. Onto the backside, a 100 nm aluminum film for the acoustic pulse generation is vapor deposited. The substrate

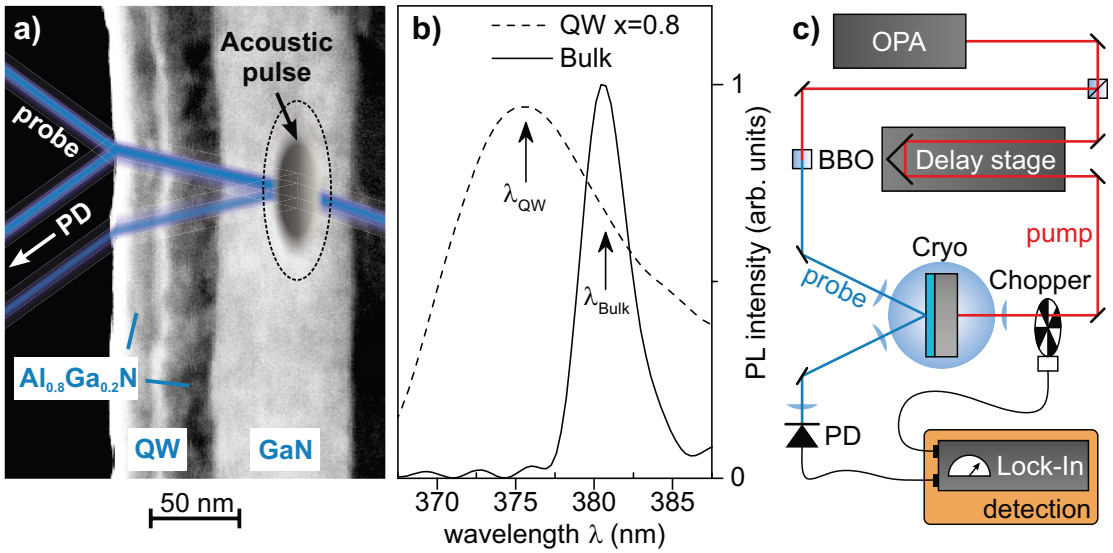

Figure 9.1: Experimental setup and sample characterization. Panel (a): SEM image of the sample showing from right to left: the SiC substrate, the c-GaN buffer layer, and the QW structure comprising the c-$Al_xGa_{1-x}N$ barriers and the c-GaN QW itself. Illustrations of the probe beam and the acoustic pulse are sketched in the top. Panel (b): Photoluminescence spectra of the QW with $x = 0.8$ and of bulk c-GaN recorded at cryogenic temperatures. The confinement energy can be deduced from the central wavelengths λ_{QW} and λ_{Bulk}. Panel (c): Experimental pump-probe setup. The probe beam is frequency-doubled in a BBO crystal and detected by a Photodiode (PD).

is followed by a 10 µm thick 3C-SiC layer. On top, the actual sample structure is grown: it consists of a 80 nm c-GaN buffer layer and two 35 nm thick c-$Al_xGa_{1-x}N$ barriers, which sandwich the c-GaN QW with a thickness of d_{QW}=10 nm. The layer thicknesses were determined from the SEM images recorded by the group of Horst Fiedler from the TU Dortmund university. Two samples with different barrier heights are studied, where the Al content is $x = 0.1$ and $x = 0.8$. The PL spectrum of the sample with $x = 0.8$ was recorded at a temperature of T=15 K by the group of D. As. It is shown in Fig. 9.1 (b) as the dashed line together with the PL from a reference c-GaN bulk sample plotted as the solid line. The bulk layer emits at a central wavelength of λ_{Bulk}=380 nm, while the peak of the QW is slightly blueshifted at λ_{QW}=375 nm. This blueshift corresponds to a confinement energy of E_C=45 meV. The PL of the QW is extended further towards longer wavelengths, which is probably related to defect states at the layer interfaces. It is therefore hard to deduce the FWHM of the electronic QW transition from the PL.

The time-resolved pump probe setup used to measure the reflectivity modulation $R(t)$ due to the interaction of the acoustic pulse with the c-GaN QW is shown in Fig. 9.1 (c). Both the pump beam and the probe beam are generated by an amplified laser system

(Light Conversion: Pharos) with a central wavelength of 1030 nm, a pulse duration of 100 fs, and a repetition rate of 30 kHz. These laser pulses are forwarded to an **o**ptical **p**arametric **a**mplifier (OPA, Light Conversion: Orpheus), which allows to select a wavelength from 630 nm to 2600 nm. The energy per pulse after the OPA is about 15 µJ. The OPA output is divided into the pump beam and the probe beam by a 50/50-beam splitter. The pump beam is guided over a variable linear delay line to the backside of the sample, where it is focused to a spot with a diameter of about 100 µm to launch the acoustic pulse. The sample is placed in a flow cryostat and cooled down to a temperature of ∼40 K to prevent a strong attenuation of the created coherent phonons. Since the nonlinear acoustic coefficients are rather weak in Si, the profile of the acoustic pulse is assumed to be preserved during the transit through the substrate [54]. The probe beam is used to detect the acoustic pulse in the QW. To maximize the photoelastic coupling, the wavelength needs to be tuned to a spectral region, where the dispersion slope of the complex index of refraction is steep; i.e., close to the absorption edge [cf. Eq. (8.9)]. The probe beam is therefore frequency-doubled in an optically nonlinear **b**eta **b**arium **b**orate **c**rystal (BBO) to transfer it into the near ultra violet, where the electronic transitions of the c-GaN QW are located. It is incident under an angle of θ_1=40° on the sample surface. One 10 cm lens focuses the probe beam to a spot with a diameter of 25 µm and a second 10 cm lens collects the reflection from the surface. The intensity of the probe beam is measured by a UV-enhanced Si Photodiode with a working range from 350 nm to 1100 nm. To increase the sensitivity towards the acoustic pulse, its output is forwarded to a Lock-In detector, which is referenced to a mechanical chopper placed in the pump beam path.

9.2 Measured and Simulated Reflectivity Modulation

At first the results obtained for the sample with the low barriers, $x = 0.1$, are discussed. The reflectivity change $\Delta R(\tau)$ is normalized to the reflectivity R_0 in absence of the acoustic pulse and recorded for three different probe wavelengths λ close to the absorption edge of the QW and the bulk layer. The results are obtained for a pump excitation density of about W_0∼4 mJ/cm^2 and presented in Fig. 9.2 (a). At a delay of τ=0 ps, the acoustic pulse reaches the top surface of the sample. For delays between -40 ps≤τ≤40 ps an almost symmetrical oscillatory behavior is observed. For a wavelength of λ=380 nm, there are two pronounced peaks appearing at ∼±30 ps, which enclose the oscillations. When the wavelength is decreased in 5 nm steps to 370 nm, the amplitude of these oscillations increases, while the relative height of the two outer peaks shrinks. A FFT is performed to analyze the frequencies of the observed oscillations. The results are shown in Fig. 9.2 (b) and possess several broad peaks. The peaks with the highest frequency are indicated by arrows and wander from 112 GHz for λ=380 nm to 118 GHz for λ=370 nm. These peaks match well the frequency f_B of the coherent

Brillouin-oscillations for pure c-GaN, which are calculated by Eq. (8.10). With the sound velocity v_{GaN}=6950 m/s, n=2.7 for the used λ, and θ=40°, one obtains f_B=99 GHz and f_B=103 GHz for λ=370 nm and λ=380 nm , respectively [84]. Most probably this 13 % deviation is due to the altered value for the sound velocity in the c-GaN/$Al_{0.1}Ga_{0.9}N$ heterostructure compared to bulk c-GaN.

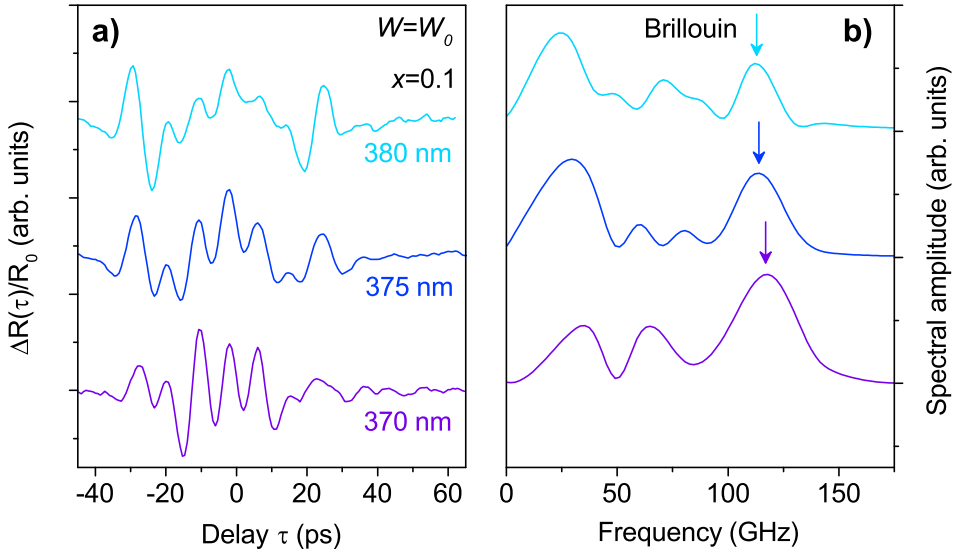

Figure 9.2: Reflectivity modulation for the QW with $x = 0.1$. Panel (a): Temporal profile of the relative reflectivity modulation $\Delta R(\tau)/R_0$ for three different probe wavelengths λ and a pump excitation of W_0∼4 mJ/cm^2. Panel (b): The FFT shows that the main part of the signal originates from coherent Brillouin-oscillations (marked by the arrow).

The only sharp features that could possibly be related to the QW are the two pronounced peaks at ∼±30 ps. If one takes their temporal separation and multiplies it with v_{GaN}, one finds that the acoustic pulse travels a distance of about 350 nm. This difference corresponds very well to twice the distance through the whole structure from the interface between the SiC-substrate and the c-GaN buffer layer to the surface. Obviously, these peaks are related to a displacement of this interface. There are actually no fingerprints in the signal that can be related to the shallow c-GaN QW. This is not very surprising, because for $x = 0.1$ the elastic and optical properties of the $Al_xGa_{1-x}N$ barriers and the c-GaN bulk and QW layer are quite similar and the sample can be treated as a homogeneous block made from a material with parameters close to GaN. Therefore, the detailed analysis of $\Delta R(\tau)$ that would also involve the interface displacement effect will not be pursued any further for $x = 0.1$.

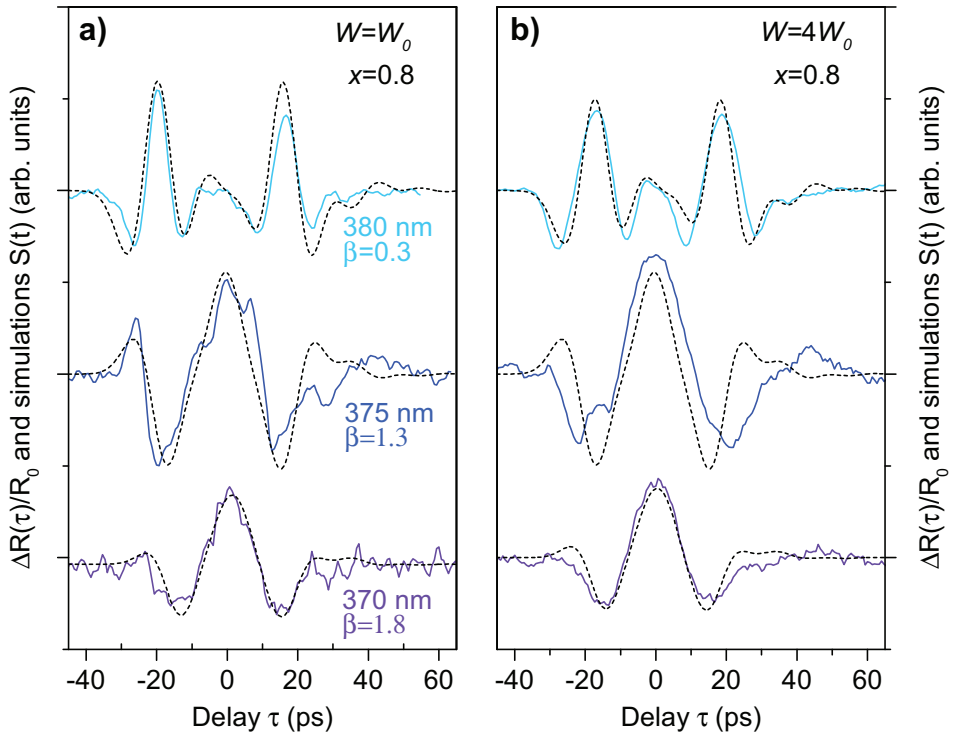

Figure 9.3: Reflectivity modulation for the QW with $x = 0.8$. Three different probe wavelengths λ were experimentally studied (colored solid lines) and modeled by a simulations based on a perturbed transfer-matrix (dashed lines). The β-factor states the relative photoelastic coupling strength of the c-GaN QW and bulk layer. Panel (a): Reflectivity modulation for a medium optical pump excitation of $W_0 \sim 4$ mJ/cm^2. Panel (b): Reflectivity modulation for a higher pump excitation of $4\,W_0$. The higher acoustic nonlinearities lead to a broadening of the peaks.

The same experiments are repeated for the second sample with a higher Al content of $x = 0.8$ in the barriers. Again, three wavelengths λ are used and moreover, two different pump densities, W_0 and $4\,W_0$ were studied. The results for the lower and the higher pump density are shown in Fig. 9.3 (a) and Fig. 9.3 (b), respectively, as the colored solid lines. The relative reflectivity modulation $\Delta R(\tau)/R_0$ does not show the coherent Brillouin-oscillations anymore and the peaks in the FFT are strongly suppressed. This time, the spectral components are not analyzed and the FFT is not shown. Instead, the reflectivity profile shall be reproduced by a perturbed transfer-matrix directly in the time domain. First of all, the reflectivity modulation is described in more detail, though.

For the shortest wavelength of λ=370 nm [cf. the lower curves in Fig. 9.3 (a) and Fig. 9.3 (b)], the reflectivity modulation has a simple shape, with a maximum at τ=0 ps and two neighboring dips with about half the amplitude. This shape is typical for a

picosecond acoustic pulse that is detected by a thin layer so close to the surface that the incoming and the reflected acoustic pulse overlap inside the layer [81, 2]. The details of the shape will be discussed further below in the context of the transfer-matrix simulations to come. It will be shown that the response is attributed to the photoelastic interaction of the acoustic pulse with the c-GaN QW. The approximate extension of the electronic wavefunction in the QW yields the time resolution limit of $d_{\mathrm{QW}}/v_{\mathrm{GaN}}\approx$1.4 ps, which is short enough to resolve the main features of the strain pulse. The total duration of the signal including the dips is about 50 ps.

When the probe wavelength is increased to λ=375 nm, the shape remains basically the same [cf. the middle curves in Fig. 9.3 (a) and Fig. 9.3 (b)]. The same central peak is observed, but compared to the previous case, there are additional peaks appearing earlier at τ=-30 ps and lasting longer until τ=-35 ps. Apparently, the acoustic pulse is detected for this probe wavelength also in layers, where the acoustic pulse arrives earlier and leaves later, namely the layers that are buried deeper beneath the surface. One possible explanation might be a longer optical penetration depth for the increased λ. This could be due to a smaller absorption of either the c-$Al_{0.8}Ga_{0.2}N$ barriers or of the c-GaN QW. However, the barriers on the one hand start to absorb only wavelengths shorter than 300 nm [140], while the thin QW on the other hand only absorbs a small fraction of the incident light [20]. Another possible reason might be that the photoelastic coupling constant $p(E)$ of the bulk layer becomes stronger, the closer the wavelength approaches its resonance at λ_{Bulk}=380 nm. Having the linear relation between $p(E)$ and the dispersion slope of the complex refractive index in mind, this assumption seems quite natural.

Indeed, for a wavelength of λ=380 nm, the QW becomes transparent and the central peak at τ=0 completely vanishes, while the outer peaks associated with the bulk layer become more pronounced. The signal looks strongly different compared to the previous cases. If one compares the signals with the same probe wavelength but different pump excitation density in Fig. 9.3 (a) and Fig. 9.3 (b), one finds that (i) the noise decreases and (ii) the peaks get broader and smear out with higher pump intensity; see the missing peaks at $\tau = \pm$30 ps for λ=375 nm, for example. The nonlinear acoustic propagation seems to play a more important role for the higher pump excitation leading to longer acoustic pulses.

In the following, the measured reflectivity modulation is subjected to a rigid theoretical study based on a perturbed transfer-matrix approach. This transfer-matrix contains the interface-displacement effect and the photoelastic contribution in the manner it is described in the previous chapter. Both effects generally depend on the probe wavelength and might explain the found behavior. The aim is to elucidate whether the different dispersions of the photoelastic coupling constants in the c-GaN QW and the bulk layer lead to the strong wavelength dependence. If this assumption can be verified, it is proven that (i) the QW is indeed able to detect strain pulses and (ii) that the response can be

separated from the one of adjacent GaN layers, when the probe wavelength is chosen properly. Although the strong λ-dependence close to the absorption edge already indicates that this question can most probably be answered positively, the first step in the analysis is to exclude that the interface displacement is the driving contribution. Afterwards, the photoelastic contributions of the bulk layer and the QW will be compared to find out at which probe wavelength the QW detects strain the best and the contrast between QW and bulk is the highest.

The photoelastic coupling in the QW is neglected in the calculations at first. This is done, because the dispersion is known in bulk c-GaN only, but not for the QW [46]. Although these simulations will likely not be able to reproduce the experimental findings, they will give a first insight into the relative contribution of the photoelastic effect and the interface displacement. Due to the small nonlinear coefficients of the Si substrate, the displacement pulse is modeled by a Gaussian with an amplitude of 50 pm, while the unknown temporal FWHM is set to 12 ps for the best agreement with the experimental results. This duration is only slightly higher than the one of the acoustic pulse injected from the metal film into the substrate, which is about 10 ps [cf. Fig. 2.4 (a)]. For the sound velocities, v_{GaN}=6950 m/s and v_{AlN}=10,500 m/s are found, in accordance with Ref. [84] and Ref. [136], respectively. The mass densities for the calculation of the acoustic impedance are also taken from the latter reference. The dispersion of the complex index of refraction for GaN and AlN is deduced from the data in Ref. [51]. For the band gap deformation potentials a_{GaN}=-7 eV and a_{AlN}=-10 eV are chosen based on the theoretical predication in Ref. [99]. All material parameters of the $\mathrm{Al}_x\mathrm{Ga}_{1-x}\mathrm{N}$ alloy are assumed to be the mean of the pure materials weighted by x, except for the complex index of refraction, for which Ref. [119] provides information. The interface between the SiC substrate and the c-GaN buffer layer is not included, because the reflection originating from there needs to pass twice through the 100 nm thick absorbing c-GaN layer and is therefore rather weak when arriving back at the front surface.

Fig. 9.4 (a) shows the simulated reflectivity modulation $S(t)$ obtained with a perturbed transfer-matrix that includes either the photoelastic effect in the barriers and the c-GaN bulk layer (solid line) or the displacement effect (dashed line). The direct comparison reveals that the photoelastic contribution exceeds the interface displacement for all three studied wavelengths even without the QW. One can see that the photoelastic coupling in the bulk-layer is stronger, the closer the probe wavelength is to the resonance at λ_{Bulk}=380 nm, because here the rise of absorption leads to a steep slope of the extinction coefficient κ. The dispersion of the real part is rather flat here, but the imaginary part obviously compensates for this [cf. Fig. 9.4 (b)]. While the acoustic pulse passes through the c-GaN bulk layer, the photoelastic contribution leads to coherent Brillouin-oscillations. However, there are not many full periods observed, because the layer is thin compared to the optical wavelength in the medium. A phase jump occurs, when the acoustic pulse reaches the surface at τ=0 ps and is reflected. The photoelastic

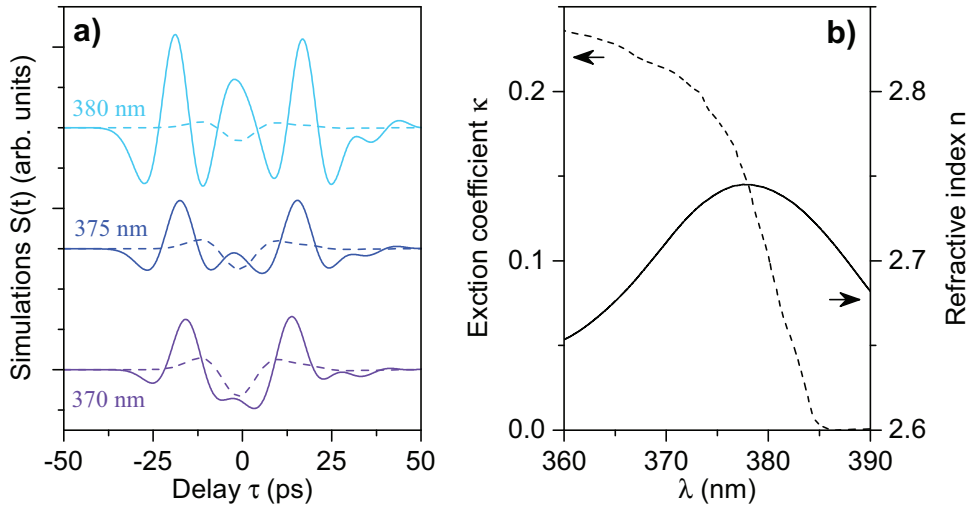

Figure 9.4: Calculated reflectivity modulation $S(t)$. Panel (a): Simulations taking the photoelastic effect in the bulk and barrier layers (solid line) or the interface displacement (dashed line) contribution into account. Panel (b): Dispersion of the refractive index n (solid line) and the extinction coefficient κ (dashed line) for bulk c-GaN deduced from Ref. [51]. The data was initially recorded at room temperature and is presented here with a shifted x-axis to account for the temperature drift.

contribution of the barrier layers is negligible, because the barriers are transparent and the dispersion is flat.

The reflectivity change due to interface displacements possesses a different shape. One can see a shape very similar to the one observed in the experiments for λ=370 nm, but with a flipped sign: a symmetric profile with a central dip centered at τ=0 ps flanked by two peaks with half the amplitude. For all three wavelengths the basic shape of the reflectivity modulation stays the same, while the amplitude subsequently increases the shorter the wavelength becomes. For the shortest wavelength of λ=370 nm the photoelastic contribution and the displacement effect have a comparable amplitude.

Two statements can be made from the analysis. First, the photoelastic effect contributes to the reflectivity modulation $S(t)$ for all three studied wavelengths and the response cannot be described by the displacement effect alone. This is especially the case for λ=380 nm, where the c-GaN bulk layer is resonant and the displacement effect is minimum, but holds also true for the other studied wavelengths. Second, the sum of the simulated reflectivity modulations due to photoelasticity and interface displacement does not match the measured reflectivity modulation $\Delta R(t)/R_0$ for λ=370 nm and λ=375 nm [cf. lower and middle curves in Fig. 9.3]. This leads one to the main conclusion of this chapter: at these wavelengths, there must be a significant photoelastic

contribution of the QW that the model lacks so far. In the next step, the QW is therefore included in the simulations $S(t)$ and its photoelastic coupling constant $p(E)$ is used to fit the results to the experimental curves.

Without detailed knowledge of the optical properties of the QW, the dispersion of n and κ is here assumed to be identical to the one in bulk c-GaN, but shifted by the confinement energy E_C=45 meV of the QW. The slope is additionally multiplied by a real scalar α, which is used as a fitting parameter in the following, such that for the photoelastic coupling constant

$$p(E) = \alpha \left(\frac{\partial \widetilde{n}(E - E_C)}{\partial E} \frac{\partial E}{\partial \eta} \eta \right) \tag{9.1}$$

results. This is of course a rather poor approximation, since in general the complex dielectric function needs to be calculated from the Kramers-Kronig relation. This calculation is based on the electronic band structure, which must include the higher order quantized electronic states in heterostructures [72]. Practically this means for example, that in a QW the extinction coefficient is assumed to rise faster than in bulk material, because higher order electronic transitions come into play that have no equivalent in the bulk material. Moreover, the linewidths of the transitions in heterostructures are often broader than in bulk materials, such that many resonances are smeared out. The detailed analysis of the dielectric function in the QW involves a large theoretical effort, which is beyond the scope of this thesis and there is no experimental literature available. Therefore, the presented approach of a shifted dispersion is used for simplicity as a starting point for the fitting procedure. Please note that α might also account for a slightly different deformation potential in the QW compared to the bulk material. Straining the QW varies its thickness and might also influence the electronic level structure (more information is found in section 4.1). When ultimately α is found for a given wavelength, the photoelastic coupling constants in the c-GaN bulk layer and the QW are compared. This helps to assess, if the QW can detect strain exclusively despite of the c-GaN bulk layer being close. To this end, the ratio of the photoelastic constants $\beta(E)$ will be calculated

$$\beta(E) = \left| \frac{\alpha \left(\partial \widetilde{n}(E - E_C) \right) / \left(\partial E \right)}{\left(\partial \widetilde{n}(E) \right) / \left(\partial E \right)} \right|. \tag{9.2}$$

The simulations comprising all contributions are plotted together with the measured curves in Fig. 9.3 as black dashed lines. For a wavelength of λ=370 nm, excellent agreement between experiment and theory is achieved. Including the QW yields the proper shape with the correct width. Besides this, also the faint shoulder at τ=-24 ps, which is only found for the small pump density W_0 shown in Fig. 9.3 (a), is reproduced. The response is almost completely governed by the photoelastic contribution of the QW. The shape of $S(t)$ is proportional to the strain applied to the thin layer close beneath

the surface. First, the leading compressive part of the strain pulse passes the QW and leads to the small dip at τ=-14 ps, followed by the tensile part, which causes the peak around τ=0 ps. Since the QW is located close to the surface, the trailing part of the incident and the leading part of the reflected acoustic pulse overlap. Since the sign of the strain is flipped during the reflections, both are tensile and interfere constructively, which doubles the amplitude of the central peak. Finally, the passage of the trailing compressive part of the reflected acoustic pulse is responsible for the second small dip at τ=14 ps. The wavelength of the probe laser is on the higher energy flank of the QW resonance at λ_{QW}=375 nm. Nevertheless, the higher electronic energies seem not to influence the photoelastic coupling constant strongly and only a small refining via α=1.5 is necessary, which corresponds to β=1.8. Indeed, the QW is more sensitive than the bulk layer, although the real part of the bulk dispersion is fairly steep for this wavelength as well.

When the probe wavelength is increased to λ=375 nm, the agreement worsens a little bit, but is still reasonable. The simulated curve includes the additional peaks at τ=-26 ps due to the bulk layer becoming more sensitive to strain now. Also the following broad dip and the central peak are correctly reproduced. There are however deviations: the width of the central peak does not fit very well, and the asymmetric behavior of the experimental curve after the reflection of the acoustic pulse at the surface is not observed in the simulations. The counterpart of the peak at τ=-26 ps is completely missing in the experiment, which points to a very rough sample surface where no regular acoustic reflection takes place. For best agreement, the contribution of the QW has to be scaled down to α=0.5. There are many possible explanations for this large correction; one is for example that the QW transitions are inhomogeneously broadened and this is translated into a smeared-out dielectric function with smaller slope. The wavelength is now on resonance with the QW and the relative photoelastic coupling strength is found to be β=1.3. Still, the biggest part of the response is due to the QW, mostly because of the steep increase of κ.

This situation changes, when the wavelength is increased further to λ=380 nm. The QW becomes transparent, while the bulk layer is resonant. The shape of the reflectivity modulation shows two large peaks associated with Brillouin-oscillations in the bulk layer at $\tau = \pm 18$ ps, which is well reproduced by the model. The coupling strength of the QW needs again to be slightly decreased by a factor of α=0.7. The response is not very sensitive to α, since the contribution of the bulk layer governs the reflectivity modulation. The comparison between QW and bulk shows that β=0.3 and consequently the signal looks very similar to the one in Fig. 9.4 (a) calculated without the QW at all. Again, there are deviations between experiment and simulation, namely the asymmetry between incident and reflected pulse that is only observed in the experiment. The SEM images used for the layer thickness characterization presented in Fig. 9.1 (a) show that the surface of the sample is often not very plain and that the interfaces of the various layers

are bent. It is quite conceivable that the acoustic pulse is reflected under an angle and experiences other layer thicknesses on its way back through the structure, which explains the asymmetry of the signals.

When comparing the calculations with the experimental data obtained for the high pump excitation in Fig. 9.3 (b), one finds that the simulations produce peaks non-existent in the experiment, for example in the case of λ=375 nm. Furthermore, many peaks are too narrow. This gives strong support to the assumption that the acoustic pulse for the higher pump density is actually longer than assumed, which might cause peaks to broaden or completely smear out. However, the broader peaks cannot be reproduced by simply increasing the width of the input Gaussian displacement pulse. Nonlinear acoustic propagation apparently plays a more important role than considered so far and a correct treatment with the Korteweg-de-Vries-Burgers would be the next logical step. Nonetheless, this theoretical modeling is not performed here because it would require a lot of effort and bring only limited new understanding.

Another shortcoming is the unknown precise extension of the electron wave function of the QW. Its penetration depth into the barriers might stretch the photoelastic contribution of the QW. Moreover, the refractive index and sound velocity in the strained barrier layers are unknown. Because of the lattice mismatch between GaN and $Al_xGa_{1-x}N$ of $\sim$3 % [109], the internal strain is assumed to be on the same order - at least right at the interfaces - and therefore exceeds the strain exerted by the acoustic pulse by one order of magnitude. The impact of the static strain on the optical and mechanical properties can strongly influence the reflectivity modulation.

This chapter showed that a c-GaN QW is an efficient detector for ultrashort acoustic pulses, provided that the QW is enclosed by barriers with different optical properties. In the present case, the strain pulse could only be mapped in the QW with high barriers (x=0.8). The detection mechanism is based on the photoelastic effect and the response of the QW could well be separated from the one of an adjacent c-GaN bulk layer by choosing a proper wavelength: the photon energy needs to be on resonance with the electronic transitions in the QW, but away from the fundamental band edge in the bulk material; i.e. for wavelengths λ <375 nm for the studied QW. The theoretical limit for the time resolution of the QW is given by its thickness and found to be d_{QW}/v_{GaN} $\sim$1.4 ps, but the acoustic pulse did not contain features short enough for a verification. The experiments were supported by a theoretical analysis based on a perturbed transfer-matrix method. This analysis allowed to rule out that the displacement effect is responsible for the strong λ-dependence in the experiments. Ultimately, the relative strength of the photoelastic coupling constant in the QW and the bulk layer could be obtained from fitting the simulations to the experimental data, in order to find the most suitable optical wavelength for the detection of strain waves.

Chapter 10

Acousto-Optical Nanoscopy in an AlAs/GaAs Micropillar

The previous chapter presented a method to detect ultrafast acoustic pulses by optical means. Acoustic nanoscopy experiments might not compulsorily involve optics in the future, because the echoes can in principle be detected electrically [85] and there is also an increasing effort to generate short acoustic pulses without using sub-picosecond lasers. The most promising results were obtained, on the one hand, for SAWs either by Fourier-synthesis of many harmonics [108] or by confined 2D-electron gases [111], and, on the other hand, for bulk waves by electrically tilted Wannier-Stark ladders in superlattices [49, 50, 79]. Purely acoustic nanoscopy experiments rely on a mismatch of the acoustic impedances of the numerous materials forming the structure under study. Many material systems commonly used in photonics provide a sufficient acoustic contrast, for example 1.25 for Si/SiO_2, 1.2 for GaAs/AlAs, or 1.35 for GaN/AlN, such that this is not a very severe fundamental restriction. The acoustic nanoscopy is in most cases absolutely sufficient if one is interested in a characterization of layer thicknesses in photonic devices alone.

Here, a new acousto-optical nanoscopy method is proposed that comes into play when also information about the light field distribution inside a photonic device shall be obtained. The basic idea is sketched in Fig. 10.1: a deeply-penetrating laser beam is directed onto the studied structure and builds up the light field intensity sketched in red. The device imprints a unique spatial distribution onto the light field, which is exploited for the characterization of the underlying geometry. A picosecond acoustic pulse is injected into the sample and propagates along the z-direction towards the surface. During its passage, the optical reflectivity for the wavelength corresponding to the investigated light field distribution is tracked.

The acoustic pulse locally changes the optical properties of the device like described in chapter 8. This local perturbation leads to a modulation of the reflectivity, which can

be linked to the light field at the momentary position of the acoustic pulse. An easy and intuitive situation is for example, when the acoustic pulse is located at a node of the photonic field and the reflectivity modulation is consequently zero. However, in most cases the interpretation of the reflectivity modulation is not so straight forward. The difficulty arises from the complex light-sound interaction in photonic devices depending on many factors: (i) the width of the acoustic pulse, its phonon spectrum, and the phonon dispersion in the structure; (ii) the light field distribution itself; (iii) the different mechanisms of light-sound interaction, namely the photoelastic effect and the interface displacement.

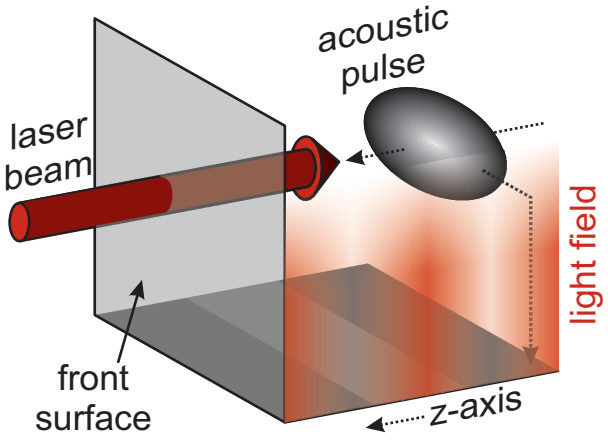

Figure 10.1: Sketch of the technique. A laser beam builds up a unique light field distribution (red) inside the structure, while an acoustic pulse simultaneously propagates along the z-axis. The acoustic pulse locally changes the optical properties at its momentary position, which is observable in the reflectivity of the laser beam.

The route to deduce unambiguous information about the light field from the reflectivity modulation is to eliminate the influence of the other parameters from the response. This can be achieved by tailoring the experimental conditions such that their influence is either negligible or can be treated in an easy analytical way. Upon achieving this, implicit information about the light field is obtained with this method, but up to now it is not possible to directly measure the distribution. However, this implicit information allow one to reconstruct the light field in a backwards-engineering process by an optical transfer-matrix; from this transfer-matrix the layer thicknesses of the underlying photonic structure can be retrieved.

The presented acousto-optical nanoscopy is very similar to the most commonly used approach for the characterization of layered photonic devices: the reflectivity spectrum is first measured and afterwards calculated by a transfer-matrix. The layer thicknesses can be deduced from the transfer-matrix, when fitting the simulated curve to the experimental data. The drawback of this method in complicated multilayered structures is that the reflectivity spectrum is an integrated measure determined by the whole structure [62]. Therefore, it offers ambiguous depth information. In contrast, the acousto-optical nanoscopy is able to probe the light field locally in a certain depth.

Since the 2000s, the so-called **n**ear **f**ield **s**canning **m**icroscopy (NSOM) technique has

been advanced further and further [102]. This technique allows one to directly measure the light field distribution. In contrast to the proposed acousto-optical nanoscopy, it does not rely on theoretical calculations based on Maxwell's equations (i.e., transfer-matrix calculations for layered planar structures). Instead, a probe tip is brought into the evanescent near-field of the studied optical mode and the radiation is either collected or scattered. Light field distributions of confined optical modes in photonic crystals [26] and microdisc resonators [65] have been mapped with a spatial accuracy of about 100 nm, defined by the size of the probe tip. The technique makes it also possible to track the transit of an ultrashort laser pulse through a fiber with high temporal and spatial resolution [11]. However, the light field can only be measured at the surface and no depth information is obtained.

In this chapter, the acousto-optical nanoscopy is presented as a new tool for the light field characterization with depth resolution. The first section elucidates the theoretical background of the technique. It describes how the reflectivity modulation induced by an acoustic pulse and the internal light field distribution can be linked. The potential of the method and the conditions under which it is successful are discussed with the help of simulations for a planar microcavity as an intuitive example. In the second section, the new technique is applied to an AlAs/GaAs micropillar, where a slow light mode associated with the first photonic stop band is exploited. These results have been published in Ref. [32].

10.1 Theoretical Background and Model Simulations

In chapter 8 the perturbed transfer-matrix method is presented, which allows one to determine how the optical properties of a photonic device change during the passage of an acoustic pulse. There was an extensive effort to find a closed analytical expression for the reflectivity modulation for arbitrary structures and acoustic pulse shapes [80]. This closed expression has to account for the photoelastic effect and the interface displacement and contains many parameters. Like mentioned in the introduction, these parameters comprise for example: the shape and duration of the acoustic pulse, the acoustic properties of the studied device, the internal light field distribution for the probed wavelength, the photoelastic coupling constants, and, of course, the geometry of the device itself. If one wants to obtain clear information about one of these quantities, the others must be known exactly (or must not have any influence on the reflectivity modulation). Obtaining all of these quantities unambiguously from a single reflectivity trace is not possible, because the simulations are strongly over-determined. In the following, a route is presented by which the response can be simplified until only the light field distribution and the layer thicknesses remain as sensitive parameters for the simulations.

First of all, one of the two acousto-optical interaction mechanisms is eliminated from

the response. Since the interface displacement and the corresponding reflectivity modulation cannot be suppressed, one has to minimize the photoelastic contribution. In the case of a non-polar semiconductor for a wavelength close to the band gap, the photoelastic coupling constant $p(E)$ can be described by Eq. (8.8). If one chooses a photon energy for which all materials in the investigated structure are transparent (κ=0) and the dispersion is flat, one can neglect the photoelastic contribution. It is furthermore helpful if the acoustic pulse does not contain phonons that fulfill the condition for Brillouin-oscillations stated in Eq. 8.10. Since this frequency is usually several tens of GHz, one possibility to get rid of these phonons is to work with acoustic pulses in the linear propagation regime, where no high-frequency phonons build up in the first place. Another idea is to use low-pass filters for phonons. Please note that in periodic structures also folded Brillouin-oscillations may appear. The phonon wavevector q has to fulfill

$$q = 2\left|k \pm mG\right|, \tag{10.1}$$

where k is the photon wavevector in the medium, G is the reciprocal lattice vector of the superlattice, and m is an integer. Therefore, it may be possible that also unavoidable low-frequency Brillouin-oscillations take place.

Once the photoelastic contribution becomes negligible, the relative reflectivity modulation $\Delta R(t)/R_0$ is only due to the interface displacement and can be described by

$$\frac{\Delta R(t)}{R_0} = -k_0 \mathrm{Im}\left[\sum_i \delta\epsilon(z_i)\frac{E^2(z_i)}{r}u(z_i,t)\right]. \tag{10.2}$$

In this equation, k_0 is the photon wavevector in vacuum and the sum runs over all interfaces denoted by i. Their positions and the contrast of the dielectric function are marked by z_i and $\delta\epsilon(z_i)$, respectively. Moreover, r is the complex reflection coefficient of the whole structure, and $E(z)$ is the light field distribution of the probed optical mode inside. This light field distribution $E(z)$ is complex, normalized, dimensionless, and obtained from a transfer-matrix calculation, which also yields r. The phase and amplitude is determined by the boundary condition for the top surface at $z = 0$ outside the sample, where the electric field has the form $E(z=0,t) = \exp(ikz) + r\exp(-ikz) = 1 + r$ [cf. Fig. 8.1 (a)]. For non-absorbing media, $\delta\epsilon(z)$ is real and one can see that the reflectivity modulation is actually a convolution of the acoustic pulse $u(z,t)$ with a quantity closely related to the optical light field distribution $\rho(z) = \mathrm{Im}\frac{E^2(z)}{r}$.

This convolution is evaluated at a discrete set of sampling points, namely the interfaces, whose weight is determined by the contrast of the dielectric function. If the spatial extent of the acoustic pulse is smaller than the distance between neighboring interfaces, one can in principle measure $\rho(z)$ at single interfaces. If the acoustic pulse is long enough to perturb several interfaces at a time, the response is more complicated. It is unfortunately not possible to directly calculate the real part of the electric field or the intensity from $\rho(z)$. Anyway, $\rho(z)$ reveals information about the light field, which

is very useful for its reconstruction. How this works in detail, will be discussed in the following with simulations performed for the example of a planar microcavity.

Consider a planar microcavity made from two DBRs with 30 periods of alternating AlAs/GaAs layers. The mirrors are optimized for an optical zone-edge stop band centered around 925 nm at cryogenic temperatures, which requires layer thicknesses of 78 nm and 66 nm for the AlAs and GaAs layers, respectively. These nominal layer thicknesses of the top and bottom DBR are multiplied by different scaling factors of $(1\pm x)$, respectively, to show the sensitivity of the proposed acousto-optic nanoscopy for devices with a slightly different depth profile. Between the bottom and top DBR, a 264 nm thick GaAs cavity layer spacer is sandwiched. Fig. 10.2 (a) shows the calculated reflectivity spectrum for two rather similar structures with $x = \pm 0.03$. The reflectivity spectrum does not depend strongly on whether the top DBR is the thick ($x > 0$, red curve) or the thin ($x < 0$, blue curve) one. The position and the width of the central stop band is not affected by the different sign of x and only in the sidebands there are some deviations. From these slight deviations it is hard to distinguish the two differently rescaled microcavities in the experiment. This example elucidates that the reflectivity spectrum is a measure with very limited depth conclusiveness.

However, for a wavelength of λ=830 nm close to the optical stop band [marked by the arrow in Fig. 10.2 (a)] the slightly different periodicity in the bottom and top DBR is translated into a significantly different light field distribution $|E(z)|^2$. There are two oscillatory components: the first one is a fast oscillatory component that is associated with the optical wavelength. Its frequency is the same in the bottom and top DBR and not affected by the layer thicknesses. The second contribution is a slowly varying envelope function, which is different in the top and bottom DBR. The wavevector of this envelope function is given by the mismatch of the wavevectors G and k associated with the DBR periodicity and the optical wavelength, respectively. The closer the probe wavelength is to the stop band, the smaller is this mismatch and the longer the period of the envelope function. When the mismatch finally approaches zero, the probed light field falls into the stop band and the oscillating envelope function degrades into a monotonous exponential decay. Since the probed wavelength is located on the higher energy side of the stop band, the envelope's periods are longer and the relative amplitudes are higher in the shrinked DBR with the blueshifted stop band; this is the top and bottom DBR for $x < 0$ (blue curve) and $x > 0$ (red curve), respectively.

These strong deviations of the light field distributions become visible when calculating the reflectivity modulation induced by the transit of a picosecond acoustic pulse. Fig. 10.2 (c) shows $\Delta R(t)/R_0$ calculated by Eq. (10.2), where a Gaussian displacement pulse with a FWHM of 90 ps is used as the input. At a time t=0, the maximum of the pulse is injected into the microcavity and continues towards the surface with a mean sound velocity of $\overline{v}$=5230 m/s until it reaches the top facet at $t\approx$1.75 ns. While it is propagating through the DBRs, pronounced oscillations of the reflectivity are observed.

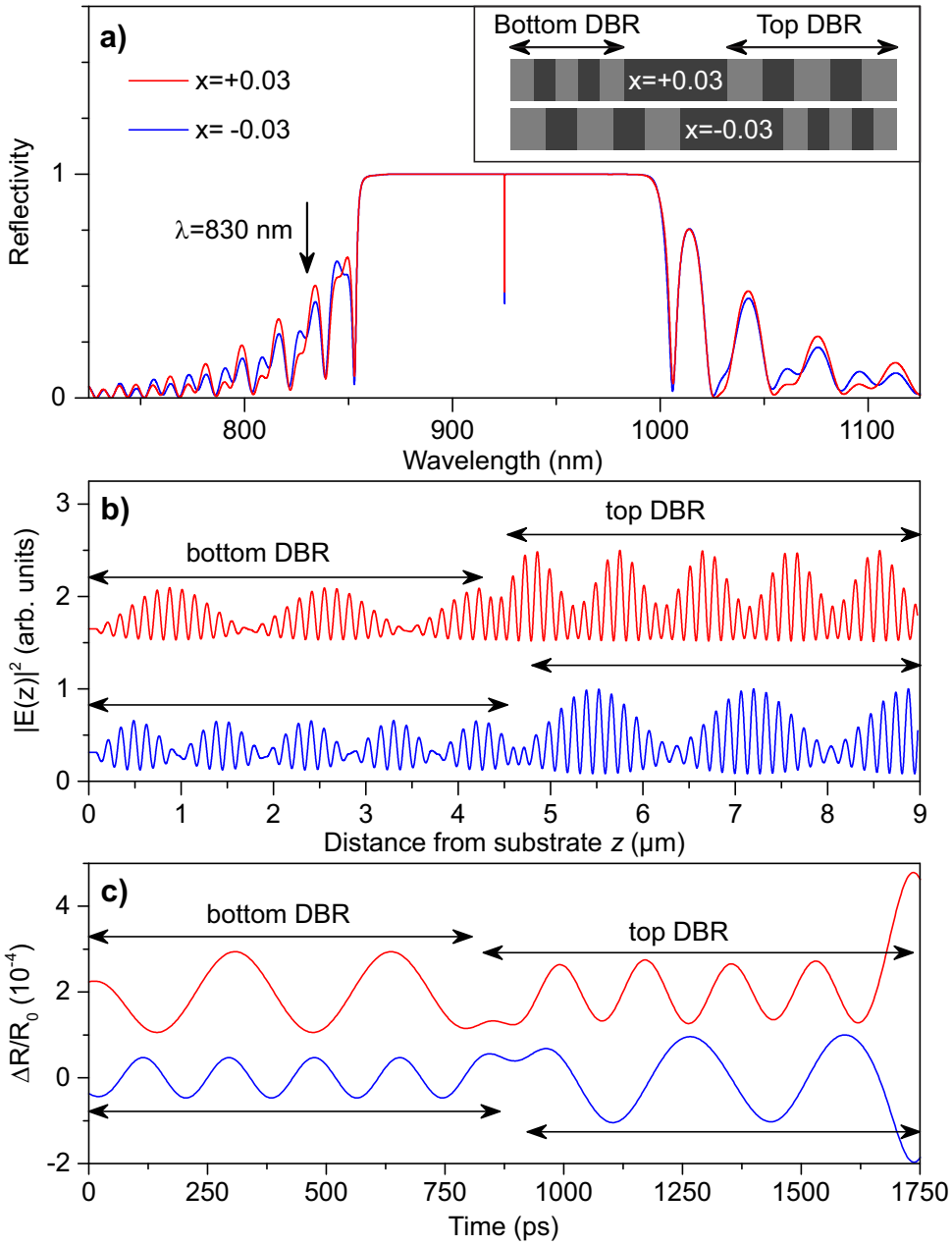

Figure 10.2: Simulated reflectivity modulation for two slightly differently rescaled planar microcavities with x=-0.03 (blue curves) and x=+0.03 (red curves). Panel (a): Calculated reflectivity spectra; the arrow marks the wavelength studied in the following. The inset illustrates the influence of x (not true to scale). Panel (b): Light field distributions $|E(z)|^2$ for the wavelength indicated in panel (a) for the two microcavities. Panel (c): Temporal reflectivity change during the transit of a Gaussian displacement pulse with a FWHM of 90 ps through the devices.

The periods of these oscillations (times the mean sound velocity $\overline{v}$) and of the envelope match very well. Moreover, the total amplitude of the reflectivity modulation is proportional to the contrast between the minima and maxima of the envelope function; i.e. in the shrinked DBR the reflectivity modulation occurs with a higher amplitude and at a smaller frequency. Note that the reflectivity modulation is not directly proportional to the light field intensity distribution, but there is a nontrivial phase difference determined by the reflection coefficient r, the width of the acoustic pulse, and for absorbing media, also the imaginary part of $\delta\epsilon(z)$. From these reflectivity modulations one can clearly differentiate the two microcavities, which was not possible from the bare reflectivity spectrum alone.

It is obviously necessary to select a probe wavelength λ, whose light field distribution is strongly controlled by the parameters of the photonic device such that small variations of these parameters lead to a significant change of the reflectivity modulation. Strong dependencies of the light field distributions on the device's geometry are usually found near optical resonances. In the case of microcavities, for example, one may pick a wavelengths close to the stop band. Furthermore, the method depends on the uniqueness of the light field distribution in the device under investigation. In other words: a given light field distribution can only arise from a certain geometry.

In practical experiments, one records the reflectivity modulation during the transit, calculates the reflectivity modulation, and fits the layer thicknesses in the transfer-matrix calculations for $E(z)$ until best agreement is achieved. To make this procedure successful, several conditions must be met: first, the contribution of the photoelastic effect must be negligible, otherwise Eq. (10.2) is not valid. Second, the simulations for the reflectivity modulation must not depend strongly on the shape and the duration of the acoustic pulse. Many experimental parameters that govern the acoustic pulse's profile like the optical energy density on the metal film transducer, the substrate temperature and thickness are only controllable within a certain range. Since moreover direct measurements of the displacement profile are usually not easy to perform, it is most important that the simulations are robust against variations of this profile and a rough estimation is sufficient.

The simulations presented above are performed for a Gaussian input with a duration of 90 ps. Assuming a Gaussian makes sense if nonlinear propagation is irrelevant, for example due to a thin substrate. The further the acoustic pulse enters the nonlinear propagation regime, the more does the shape of the displacement pulse differ from the initial Gaussian profile and the longer does the duration become. For acoustic shock waves, the strain is described by a N-profile [cf. Fig. 2.4 (a)] and the displacement can consequently be modeled by a parabola [90]. Even in the solitonic regime, a parabola is a quite good approximation for the displacement pulse without its high-frequency components. Fig. 10.3 (a) shows several displacement profiles, which will be studied in the following to examine the influence of the shape and the duration of the acoustic

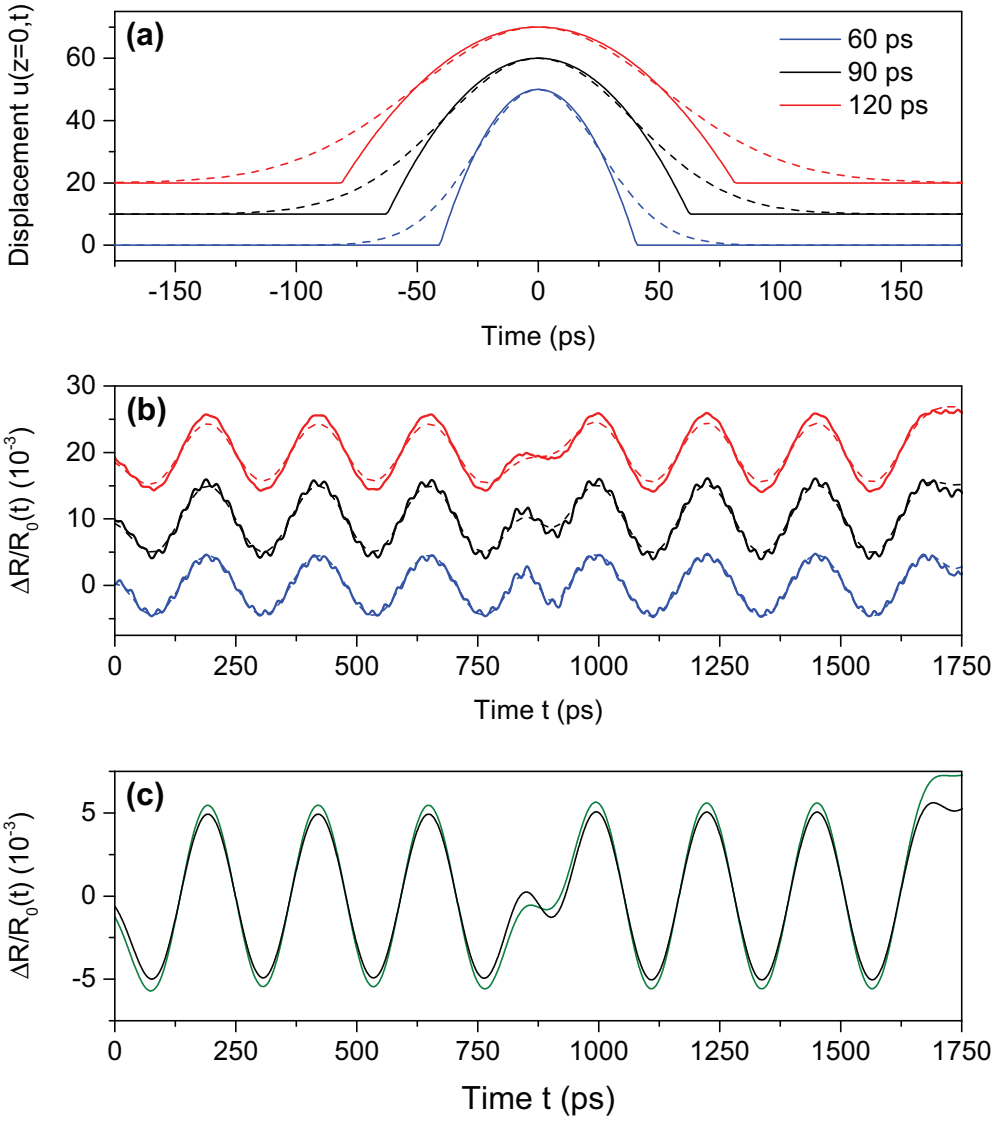

Figure 10.3: Validity of the model. Panel (a): Input displacement profiles $u(z = 0, t)$ for three different durations of the acoustic pulse. Either a nonlinear-shockwave pulse modeled by a parabola (solid curve) or a Gaussian (dashed curve) is assumed. Panel (b): Simulation of the reflectivity modulation for a symmetric microcavity (x=0.0) that is traversed by the acoustic pulses shown in panel (a). The calculations include the interface displacement and the photoelastic effect. Panel (c): Reflectivity modulation for the Gaussian with a FWHM of 90 ps with (black curve) and without (green curve) photoelasticity.

pulse on the response. On the one hand, shockwave-like parabola-shaped displacement profiles with three different FWHM (60 ps, 90 ps, and 120 ps) are chosen (solid curves). On the other hand, Gaussians with the same FWHM are employed (dashed curves). These rather long durations require nonlinear propagation to take place and usually these profiles therefore compulsorily contain high frequency phonons. Please note that the presented Gaussians or parabola-shaped displacement pulses can only be obtained by a combination of nonlinear propagation and phononic low-pass filters. How these phonon filters can be realized is explained further below.

This time, the reflectivity modulation is calculated for a symmetric microcavity (x=0) and the same wavelength of λ=830 nm like before. The simulations are not performed according to Eq. (10.2), but by a perturbed transfer-matrix including photoelasticity. The results are presented in Fig. 10.3 (b). The signals due to the parabola-shaped (solid curves) and the Gaussian (dashed curves) displacement pulses look almost the same. Because of the kinks at the front and the tail, the parabola-shaped pulses contain higher frequency components, which yield small additional fast oscillations. The response is also more or less independent of the duration of the acoustic pulse. The only notable deviations between curves with different durations occur at the transit of the acoustic pulse through the cavity layer at t=0.9 ns. Here, the phase jump of the optical field results in sharp peaks that become more and more smeared out the longer the acoustic pulse lasts.

Finally, the impact of photoelasticity is assessed. To this purpose, the full simulations with (black curve) and without (green curve) the photoelastic effect for the Gaussian with a FWHM of 90 ps are calculated. In Fig. 10.3 (c) one can see that the displacement effect dominates the total response. In the present case, this is achieved by choosing a wavelength of λ=830 nm for which the materials GaAs and AlAs are both (i) transparent and (ii) the derivative of the dispersion is minimum. The analysis proves that the conditions for a succesful acousto-optical nanoscopy are fulfilled with acoustic pulses without high-frequency components and by a proper choice of the probe wavelength.

This chapter will continue with applying the proposed technique to a real AlAs/GaAs micropillar resonator. The next section will shortly describe the acousto-optical nanoscopy setup before the results are demonstrated and discussed.

10.2 Acousto-Optical Nanoscopy of an AlAs/GaAs Micropillar

Fig. 10.4 (a) sketches the experiment used to perform an acousto-optical nanoscopy of single micropillars. The same array of freestanding AlAs/GaAs micropillars like in chapter 6 is used and a detailed description about its growth process, the growth parameters and its characteristics can be looked up in section 6.1. A time-resolved pump probe setup is employed, where the pump and probe beam are both generated by the RegA

[cf. section 4.2 for more details]. The RegA output is split by a 90/10 beam splitter. The beam with larger intensity is the pump beam and guided over a delay stage to the backside of the sample. Here, it is focused onto an aluminum film to a spot with a diameter of about 150 µm to generate the picosecond acoustic pulses. The excitation density is on the order of 10 mJ/cm^2. Combined with the 220 µm thick GaAs substrate this excitation density results in a relatively long acoustic pulse featuring strong nonlinearities arriving at the micropillar. To prevent a strong attenuation of the acoustic pulse during its transit through the substrate, the sample needs to be cooled down. It is placed in a flow cryostat and attached to a cold finger, whose temperature is kept at 8 K. Due to the laser irradiation and the loose mounting of the sample, which has to ensure access from the front and backside, the local temperature might be elevated. The probe beam with the lower intensity is used to build up the light field distribution, which will be exploited for the nanoscopy. The RegA's output is centered around 800 nm and has a spectral width of about 10 nm. These wavelengths fall into the high-energy flank of the first optical stop band of the micropillars, like illustrated in Fig. 10.4 (b) and the situation in the experiment and in the simulations presented in the previous section is expected to be quite comparable. The probe beam is focused onto the micropillars by a microscope objective to a spot with a diameter of about 15 µm. This is small enough to select a single micropillar from among the array, but so big that also the surface surrounding the micropillar's foot is illuminated. The reflection of the micropillar is collected by the same microscope objective and guided to a photodiode. To increase the sensitivity for the reflectivity change originating from the acoustic pulse, a lock-in detector is used together with a mechanical chopper that is placed in the pump beam path.

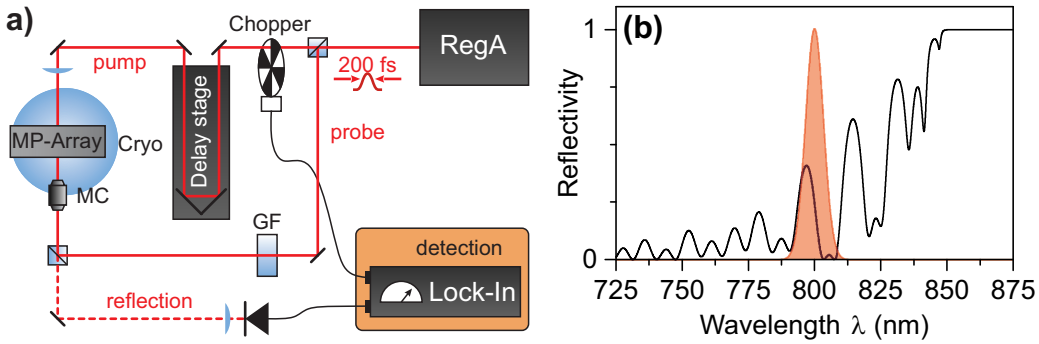

Figure 10.4: Acousto-optical nanoscopy setup. Panel (a): Overview of the time-resolved pump-probe setup. The pump beam generates the acoustic pulse and the probe beam detects the reflectivity modulation. Panel (b): Calculated reflectivity spectrum of the micropillar not accounting for the radial confinement (black) and probe laser spectrum (red area).

Fig. 10.5 (a) shows the measured reflectivity modulation $\Delta R(t)/R_0$ during the transit

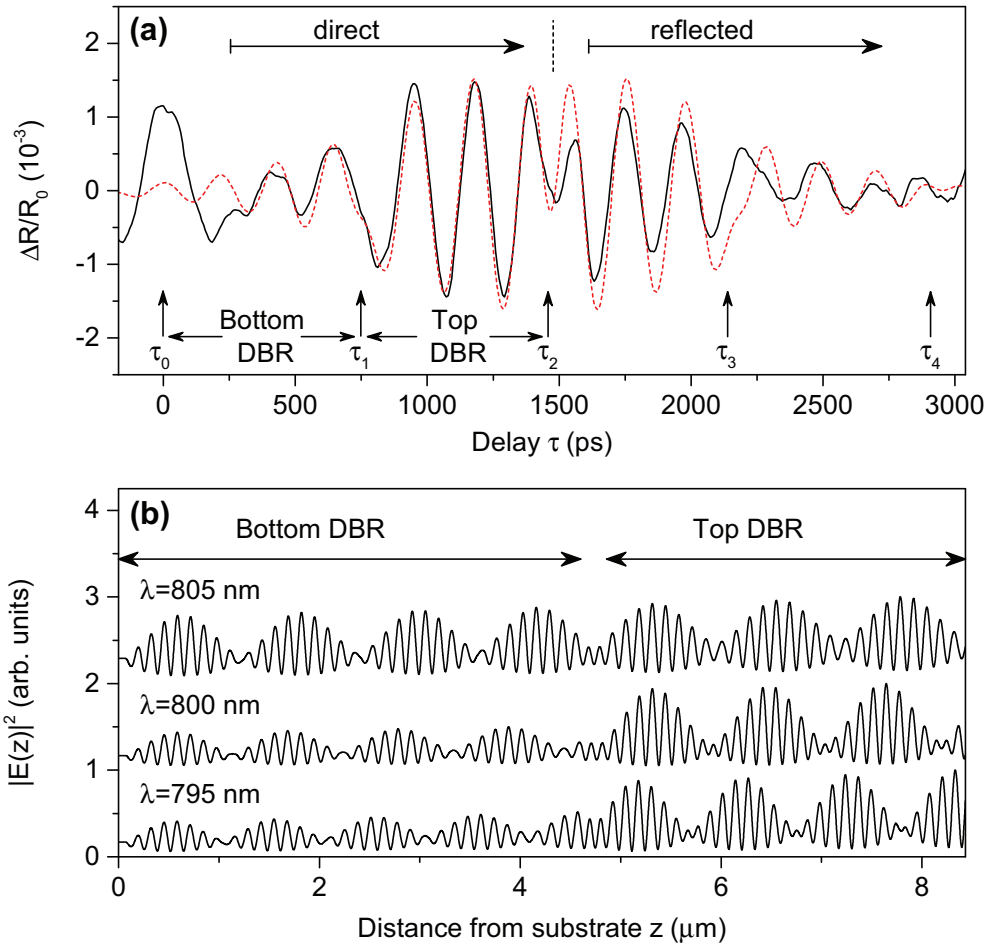

Figure 10.5: Acousto-optic nanoscopy in an AlAs/GaAs micropillar with a radius of 7.5 µm. Panel (a): Measured reflectivity modulation during the propagation of a picosecond acoustic pulse (solid black curve) and simulations yielding the best agreement (dashed red curve). The arrows indicate the delays at which the acoustic pulse leaves and/or enters a DBR. Panel (b): Light field distributions for three selected wavelengths from the probe laser spectrum that enter the simulation presented in panel (a).

of the acoustic pulse through a micropillar as a black curve. The signal was recorded for a micropillar with a radius of 7.5 µm, which is the maximum available radius from among the array. The acoustic pulse reaches the foot of the micropillar at a delay of τ_0=0 ps where a huge peak flanked by two smaller dips is observed. This feature appears, because the probe spot is larger than the micropillar's top facet even for the biggest radius and a part of the probe beam is reflected from the area surrounding the micropillar foot. The shape of this surface artifact will be explained further below. For

increasing delays τ, the acoustic pulse advances further from the foot towards the top of the micropillar. In the interval $\tau_0 < \tau < \tau_1$, the acoustic pulse is located in the bottom DBR. The reflectivity modulation undergoes pronounced oscillations and the experiment resembles the simulations performed in the previous section. The period of these oscillations cannot be obtained very well by a FFT, because only two full periods are recorded. The temporal separation between the two distinct maxima is however about 220 ± 6 ps . The accuracy of this quantity is limited by the step size of the delay stage rather than by the duration of the laser pulses, which is 200 fs and significantly shorter. At τ_1 the acoustic pulse reaches the central cavity layer and passes it within 50 ps. There are phase jumps in the light field distribution at the junctions of the two DBRs with the cavity layer [cf. Fig. 10.5 (b)] and a faint phase jump is also observed in the reflectivity modulation. Afterwards, the acoustic pulse enters the top DBR. Stronger oscillations appear that persist until the acoustic pulse reaches the top surface at τ_2. This time, three full periods can be distinguished, with a duration of 230 ± 6 ps.

From the temporal separation of τ_2 and τ_0 of about 1.47 ns and the averaged sound velocity in the structure of $\overline{v}$=5243 m/s, one finds that the height h of the micropillar is 7.7 µm, which corresponds to several doublelayers in the bottom DBR not being etched away. These remaining layers can also be seen in the SEM images in Fig. 3.3 (c), where one can identify them as the rings at the foot of the pillar. This patterning is most likely responsible for the observed surface artifact around τ_0 mentioned above. The reflectivity modulation looks very similar to the one of the c-GaN QW presented in the previous chapter [cf. Fig. 9.3]. Such a shape with a central peak neighbored by two dips with half the amplitude is typical for thin layers close beneath the surface, in which incident and reflected acoustic pulse overlap [2]. The detailed analysis of this surface feature does not concern the acousto-optical nanoscopy in the micropillar and will not be pursued further.

Upon the reflection from the top surface at τ_2, the acoustic pulse is redirected into the micropillar and a phase jump occurs. The signal is more or less symmetric and the reverse sequence is recorded, including the second transit through the cavity layer at τ_3 and so forth. For delays $\tau > \tau_4$, the acoustic pulse has left the micropillar. All further oscillations are assigned to either multi-reflections of the acoustic pulse inside the micropillar or to the excitation of its mechanical eigenmodes (cf. chapter 6). These signals are not considered in the following.

In contrast, all mechanical eigenmodes can be ruled out to be responsible for the oscillations between τ_0 and τ_4: the frequencies of the lowest extensional mode is somewhat below 1 GHz (cf. chapter 6) and it is not very likely that a single higher order mode is exclusively excited. Radial modes do virtually not exist for a micropillar attached at its foot whose radius almost exceeds its height. Last but not least, the first phononic stop band due to the DBRs appears close to 18 GHz.

The reflectivity modulation was also recorded for a micropillar with a smaller radius

of 1.5 µm [32]. The shape basically stays the same, but the smaller the top surface of the micropillar, the higher the noise and the larger the surface artifact at τ_0 associated with the micropillar's foot. Nevertheless, the micropillar shape is of crucial importance for the acousto-optical nanscopy, because it serves as an effective low-pass filter for phonons. When recording the reflectivity modulation next to a micropillar, pronounced Brillouin-oscillations in the GaAs substrate with a frequency of 44 GHz are observed. There are obviously high-frequency components reaching the foot of the micropillar, but their signatures cannot be found in the micropillar itself neither in the reflectivity measurements presented here nor in the emission modulation reported in chapter 6. A possible reason might be a strong scattering of high frequency phonons at imperfections of the micropillar sidewalls or its foot.

The experimental signal is reproduced by simulations according to Eq. (10.2) for which a planar microcavity is assumed. Fig. 10.5 (b) shows the light field distributions for three spectral components of the probe laser. Since these distributions vary significantly, the finite width of the laser spectrum needs to be taken into account. This is achieved by calculating the reflectivity modulation for each wavelength individually and weighting it by its spectral amplitude. The displacement pulse is modeled by a Gaussian with a FWHM of 90 ps. This profile is justified due to the high pump excitation density, the long propagation distance through the GaAs substrate, and the micropillar geometry, which filters all phonons with frequencies somewhat higher than 40 GHz. However, the outcome of the simulations is not very sensitive to the shape of the acoustic pulse, like discussed in the previous section. In fact, the duration of the pulse only influences to what extent the phase jump at τ_1 and τ_3 is smeared out. The agreement between simulations and experiment is excellent and almost all features of the measured curve are well captured by the model. Notable deviations occur around τ_0, when the reflection from the partly removed doublelayers from the bottom DBR is modulated. The surface artifact is obviously not included in the simulations. Moreover, the simulations fail to reproduce the pronounced asymmetry around τ_2 in the experiment. Since the calculated displacement profile includes all acoustic reflections, the stronger asymmetry in the experiment indicates that there is no regular acoustic reflection taking place at the micropillar's top. Apparently , the top surface is rather rough resulting in a diffusive scattering of phonons. Remnants of the photoresist, that was used to cover the micropillars during the preparation process (see also Fig. 6.8) might be the reason for the irregular reflection.

The excellent agreement underlines the validity of the acousto-optical nanoscopy method and allows one to perform an analysis of the metrology of the photonic device. The starting point are the nominal layer thicknesses to which rescaling factors are applied. These factors are used as fitting parameters in the simulations. Since the micropillar consists of more than hundred layers, only the cavity layer is treated individ-

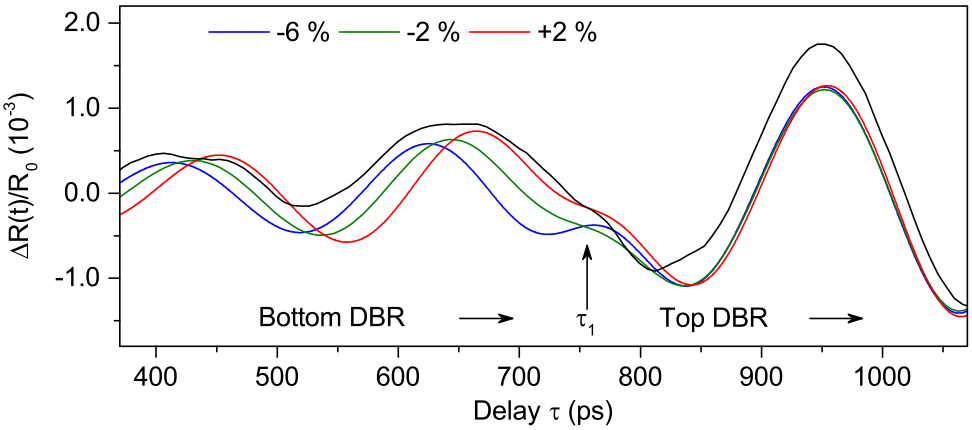

Figure 10.6: Error of the acousto-optical nanoscopy method. Experimental data (black curve) compared with simulations for various thicknesses of the cavity layer (colored curves). The calculations are vertically shifted for better visibility.

ually. To each of the two DBRs a rescaling factor is assigned that is applied to all layers in the respective DBR; i.e., each DBR possesses a uniform mean periodicity. Three quantities can therefore be extracted from the simulations: the cavity layer thickness and the mean periodicity of the bottom and top DBR.

The cavity layer thickness is found to be 2 % (=5.3 nm) thinner than intended by adjusting the phase difference between the oscillations in the bottom and top DBR. These oscillations very precisely yield the mean periodicity. Here, the period of 220 ps in the bottom DBR is slightly smaller than the one of 230 ps in the top DBR. Obviously, the probe wavelength is closer to the stop band in the top DBR. Since the probe wavelength is on the high energy flank, this means that the top DBR has a smaller periodicity than the bottom DBR. Indeed, the simulations reveal that the mean periodicity in the top and bottom DBR is 4.1 % and 3.9 % smaller than expected. For individual layers like the cavity spacer, the method yields a precision of a few nanometer, while the mean periodicity in periodic structures can be determined with an ever higher accuracy. The different mean periodicity found for the bottom and top DBR corresponds to a sub-nanometer resolution.

Finally, the error and the validity of the model will be assessed. It is quite easy to provide the error of the experimental setup, but not so straight forward to determine to what extend this error limits the accuracy of the acousto-optical nanoscopy method. The accuracy of the method depends strongly on the sensitivity of the reflectivity modulation towards structural changes of the photonic device; i.e., the error can be minimized if a probe wavelength is chosen, for which smallest changes of the layer thicknesses result in a significantly different light field distribution. However, it is hard to provide a formal

expression for the error of individual layers like the cavity spacer, for example. Fig. 10.6 shows the experimental data (black curve) together with simulations for various cavity layer rescaling factors to get an impression of the method's precision. The arrow at τ_1 indicates the passage of the acoustic pulse from the bottom into the top DBR, which is accompanied by a phase jump in the reflectivity modulation. While the simulated curves in the top DBR are not strongly affected by the thickness of the cavity layer, there are pronounced phase shifts of the oscillations appearing in the bottom DBR. Best agreement with the experiment is achieved for a 2 % thinner cavity and one can see that the curves with slightly different rescaling factors yield a worse result.

The close up image also reveals that the width of the oscillations in the simulations is too narrow only in the case of the bottom DBR. It was already shown earlier, that this issue cannot be solved by simply increasing the duration of the acoustic pulse and the fact that the width is correct in the top DBR suggests that the reason is indeed related to the bottom DBR and not to the acoustic pulse. One possible explanation for wider peaks in the experiment might be due to the $Al_{0.09}Ga_{0.55}In_{0.36}As$ QD that are placed in the cavity layer center and serve as the active medium of the device. Maybe their interaction with different spectral components of the probe light needs to be included to account for this broadening of the oscillations. Most probable is that there is no uniform periodicity in the bottom DBR. If the periodicity varies across one oscillation cycle, the peak will smear out. Unfortunately, the acoustic pulse has a duration of about 90 ps and is too long to resolve single interfaces. With a shorter pulse with a duration on the order of 10 ps it would in principle be possible to resolve single interfaces such that the thickness of individual layers can be determined. However, such a short pulse would automatically be accompanied by Brillouin-oscillations, which might mask this information again.

This chapter presented the acousto-optical nanoscopy as a new non-invasive tool for the characterization of photonic devices and their internal light field distribution. In the beginning, the theoretical background of the method was outlined and explained by taking the slow light mode in a planar microcavity as an intuitive example. Several conditions must be fulfilled for a successful operation, namely (i) a negligible photoelastic contribution, (ii) a lack of high frequency phonons, and (iii) the uniqueness of the light field distribution; i.e., a given light field distribution can only arise from a certain geometry. The technique was applied to a slow light mode in an AlAs/GaAs micropillar, where the geometry of the device acts as a low-pass filter for phonons and a proper choice of the probe wavelength minimized the photoelastic contribution. The measured reflectivity modulation is in excellent agreement with the model. The internal light field distribution was calculated by an optical transfer-matrix and used to fit the outcome of the simulations to the experimental data. From this backwards-engineering process, the layer thicknesses were automatically obtained with a resolution of a few nanometers for single layers and sub-nanometer resolution for the mean-periodicity in superlattices.

Chapter 11

Conclusion and Outlook

In the third part of this thesis two different aspects of picosecond ultrasonics nanoscopy were investigated. The first experimental work dealt with the detection of short acoustic pulses in a cubic GaN QW. The transit of acoustic pulses through the thin layer was tracked optically and manifested itself as a modulation of the reflectivity. The response of the QW could well be separated from the surrounding barrier material given that their optical properties were sufficiently different. Moreover, the experiments showed a strong dependence on the chosen optical wavelength and the profile of the reflectivity modulation changed significantly when the photon energy was tuned from the resonance of the QW to the one of an adjacent bulk c-GaN layer. A model allowed one to analyze the role of the different acousto-optic interactions, namely the interface displacement and the photoelasticity contribution of the different c-GaN layers. It turned out that the QW is an excellent detector of short acoustic pulses with a maximum possible temporal resolution of a few picoseconds and that its signal can well be separated from adjacent GaN bulk layers.

There are several ideas how to optimize c-GaN QWs as strain detectors. One idea is to replace a small part of the gallium content in the barriers by indium in order to match the lattice constants of the QW and the barrier material [7]. This way, the quality of the interfaces can strongly be enhanced. Nevertheless, the proposal is already ten years old and it is questionable if c-GaN heterostructure with good quality will be realized within the next years. The SEM images of the investigated sample shows that the layers and in particular the QW are strongly bent, which has to be avoided if the quality of c-GaN QWs shall catch up with the one of GaAs QWs [cf. the SEM images in Fig. 9.1 (a) and Fig. 3.3 (a)]. It is hard to evaluate how far the bent layers affect the strain detection - most probably sharp strain components are washed out. It would moreover be interesting to increase the width of the barriers such that the incoming and the reflected acoustic pulse do not overlap in the QW. This way, one could resolve both acoustic pulses separately.

The second work presented and developed the acousto-optical nanoscopy method. Unlike in conventional ultrasound imaging, the acoustic echoes were not of interest; instead, a characteristic internal light field distribution was probed by the acoustic pulse. The information about the light field were deduced from a complex interference pattern by a backwards-engineering process, which automatically yielded the layer thicknesses of the studied device. The accuracy of this method is striking: even for long acoustic pulses with a spatial extent of hundreds of nanometers, layer thicknesses could be probed with a nanometer resolution. The mean periodicity in periodic structures was determined with an even better resolution of less than a nanometer. The light field distributions for all wavelengths occurring in the spectrum of the probe pulse were deduced from the calculations. In the case of the micropillar laser, these results are useful for example when the VCSEL shall be optically pumped. One may pick an excitation wavelength whose distribution is found to possess a maximum at the position of the active medium.

It would be favorable to use ps-pulses for the probe beam in future acousto-optical nanoscopy experiments. These pulses provide a sufficient time resolution to track the propagation of acoustic pulses, but possess a narrower emission spectrum. This would reduce the number of wavelengths, whose light field distributions enter the simulations. The more light field distributions need to be accounted for and the stronger they differ, the more ambiguous does the outcome of the simulations become.

Moreover, it would be interesting to investigate nanometer-sized devices with solitonic acoustic pulses. Potential Brillouin-oscillations due to the high-frequency components can in principal be suppressed by applying a numerical band-pass filter to the reflectivity modulation afterwards. It might be possible to measure the convolution function of the acousto-optical nanoscopy directly at single interfaces.

In general, the method can be applied to any kind of layered photonic device, where information about light field distributions shall be obtained with depth resolution. If a probe wavelength is chosen for which all materials are transparent, the maximum available depth is only limited by the propagation distance of the acoustic pulse into the structure. For materials with an enormous acoustic mismatch/attenuation, this might turn out to be the most severe limitation. Moreover, it is necessary to suppress the photoelastic contribution, but there are materials where this is virtually impossible. These are for example materials with a polar lattice that comes along with strong piezoelectricity. The piezoelectricity then in turn couples strain and refractive index via the electro-optical effect [21].

In the present work, the micropillars act as phononic low-pass filters on their own. If the photonic device does not automatically shape the acoustic pulse into the desired form, more sophisticated tailoring of the acoustic pulse is required. If one wants to achieve Gaussian displacement pulses of a certain duration, one might for example use a semiconductor instead of a metal film in the generation process. By tuning the pump absorption length via its wavelength, one can pick the desired duration of the acoustic

pulse [128]. The profile of the acoustic pulse can also be modified after the generation process. A lot of effort is put into designing phononic low-passes, since these devices can be used to engineer thermal properties. Such low-passes often rely on complicated compound materials, like for example clathrates [43]. More easy to implement are phononic devices that rely on superlattices. These act as tunable band pass filters [120] or acoustic rectifiers [73], which can help to select a specific part of the phononic spectrum to be forwarded to the investigated device.

Bibliography

[1] S. Adachi. GaAs, AlAs, and $Al_xGa_{1\hat{a}\acute{L}\check{S}x}As$: Material parameters for use in research and device applications. *J. Appl. Phys.*, 58:R1–R29, 1985.

[2] A. V. Akimov, A. V. Scherbakov, D. R. Yakovlev, C. T. Foxon, and M. Bayer. Ultrafast band-gap shift induced by a strain pulse in semiconductor heterostructures. *Phys. Rev. Lett.*, 97:037401, 2006.

[3] A. V. Andrianov, V. M. Mylnikov, M. Y. Koptev, S. V. Muravyev, and A. V. Kim. Fibre laser with a subterahertz repetition rate of ultrashort pulses in the telecom range. *Quant. Electron.*, 46:387, 2016.

[4] Y. Arakawa, A. Larsson, J. Paslaski, and A. Yariv. Active Q switching in a GaAs/AlGaAs multiquantum well laser with an intracavity monolithic loss modulator. *Appl. Phys. Lett.*, 48:561, 1986.

[5] O. Arcizet, P.-F. Cohadon, T. Briant, M. Pinard, and A. Heidmann. Radiation-pressure cooling and optomechanical instability of a micromirror. *Nature*, 444:71, 2006.

[6] D. J. As. *Optoelectronic Properties of Semiconductors and Superlattices*, volume 19, chapter 9, page 323. Taylor & Francis, New York, 2003.

[7] D. J. As, M. Schnietz, J. Schörmann, S. Potthast, J. W. Gerlach, J. Vogt, and K. Lischka. MBE growth of cubic $Al_xI_{1-x}N$ and $Al_xGa_yIn_{1-x-y}N$ lattice matched to GaN. *Phys. Stat. Sol. (c)*, 4:2318, 2007.

[8] D R. Askeland, P. P. Fulay, and W. J. Wrigh. *The Science and Engineering of Materials*. Wadsworth Publishing, Boston, 2010.

[9] M. Aspelmeyer, T. J. Kippenberg, and F. Marquardt. Cavity optomechanics. *Rev. Mod. Phys.*, 86:1391, 2014.

[10] P. Babilotte, P. Ruello, D. Mounier, T. Pezeril, G. Vaudel, M. Edely, J.-M. Breteau, V. Gusev, and K. Blary. Femtosecond laser generation and detection of high-frequency acoustic phonons in GaAs semiconductors. *Phys. Rev. B*, 81:245207, 2010.

[11] M. L. M. Balistreri, H. Gersen, J. P. Korterik, L. Kuipers, and N. F. van Hulst. Tracking femtosecond laser pulses in space and time. *Science*, 294:1080, 2001.

[12] A. Bartels, T. Dekorsy, H. Kurz, and K. Köhler. Coherent zone-folded longitudinal acoustic phonons in semiconductor superlattices: excitation and detection. *Phys. Rev. Lett.*, 82:1044, 1999.

[13] P. L. Bender, D. G. Currie, S. K. Poultney, C. O. Alley, R. H. Dicke, D. T. Wilkinson, D. H. Eckhardt, J. E. Faller, W. M. Kaula, J. D. Mulholland, H. H. Plotkin, E. C. Silverberg, and J. G. Williams. The lunar laser ranging experiment. *Science*, 182:229, 1973.

[14] T. Berstermann, C. Brüggemann, M. Bombeck, A. V. Akimov, D. R. Yakovlev, C. Kruse, D. Hommel, and M. Bayer. Optical bandpass switching by modulating a microcavity using ultrafast acoustics. *Phys. Rev. B*, 81:085316, 2010.

[15] G. Binnig, C. F. Quate, and C. Gerber. Atomic force microscope. *Phys. Rev. Lett.*, 56:930, 1986.

[16] C. Böckler, S. Reitzenstein, C. Kistner, R. Debusmann, A. Löffler, T. Kida, S. Höfling, A. Forchel, L. Grenouillet, J. Claudon, and J. M. Gérard. Electrically driven high-Q quantum dot-micropillar cavities. *Appl. Phys. Lett.*, 92:091107, 2008.

[17] S. Brand, A. Lapadatu, T. Djuric, P. Czurratis, J. Schischka, and M. Petzold. Scanning acoustic gigahertz microscopy for metrology applications in three-dimensional integration technologies. *J. Micro/Nanolith. MEMS MOEMS.*, 13:011207, 2014.

[18] E. H. Brandt. Acoustic physics: Suspended by sound. *Nature*, 413:474, 2001.

[19] C. Brüggemann, A. V. Akimov, A. V. Scherbakov, M. Bombeck, C. Schneider, S. Höfling, A. Forchel, D. R. Yakovlev, and M. Bayer. Laser mode feeding by shaking quantum dots in a planar microcavity. *Nat. Photon.*, 6:30, 2012.

[20] D. Brunner, H. Angerer, E. Bustarret, F. Freudenberg, R. Höpler, R. Dimitrov, O. Ambacher, and M. Stutzmann. Optical constants of epitaxial AlGaN films and their temperature dependence. *J. Appl. Phys.*, 82:5090, 1997.

[21] F. Castles. Linear electro-optic effects due to high-order spatial dispersion. *Phys. Rev. A*, 92:063804, 2015.

[22] W. Chen, H. J. Maris, Z. R. Wasilewski, and S.-I. Tamura. Attenuation and velocity of 56 GHz longitudinal phonons in gallium arsenide from 50 to 300 K. *Philos. Mag. B*, 70:687, 1994.

[23] W. W. Chow, F. Jahnke, and C. Gies. Emission properties of nanolasers during the transition to lasing. *Light-Sci. Appl.*, 3:e201, 2014.

[24] W. W. Chow and S. W. Koch. Theory of semiconductor quantum-dot laser dynamics. *IEEE J. Quantum Electron.*, 41:495, 2005.

[25] S. Christopoulos, G. B. H. von Högersthal, A. J. D. Grundy, P. G. Lagoudakis, A. V. Kavokin, J. J. Baumberg, G. Christmann, R. Butté, E. Feltin, J.-F. Carlin, and N. Grandjean. Room-temperature polariton lasing in semiconductor microcavities. *Phys. Rev. Lett.*, 98:126405, 2007.

[26] B. Cluzel, D. Gérard, E. Picard, T. Charvolin, F. de Fornel, and E. Hadji. Subwavelength imaging of field confinement in a waveguide-integrated photonic crystal cavity. *J. Appl. Phys.*, 98:086109, 2005.

[27] R. S. C. Cobbold. *Foundations of Biomedical Ultrasound*. Oxford University Press, 2006.

[28] A. P. Cracknell and L. Hayes. *Introduction to Remote Sensing*. Taylor and Francis, London, 1991.

[29] J. F. Creemer and P. J. French. The piezojunction effect in bipolar transistors at moderate stress levels: a theoretical and experimental study. *Sensors and Actuators A: Physical*, 82:181, 2000.

[30] T. Czerniuk, C. Brüggemann, J. Tepper, S. Brodbeck, C. Schneider, M. Kamp, S. Höfling, B. A. Glavin, D. R. Yakovlev, A. V. Akimov, and M. Bayer. Lasing from active optomechanical resonators. *Nat. Commun.*, 5:4038, 2014.

[31] T. Czerniuk, T. Ehrlich, T. Wecker, D. J. As, D. R. Yakovlev, A. V. Akimov, and M. Bayer. Picosecond acoustics in single quantum wells of cubic GaN/(Al,Ga)N. *Phys. Rev. Applied*, 7:014006, 2017.

[32] T. Czerniuk, C. Schneider, M. Kamp, S. Höfling, B. A. Glavin, D. R. Yakovlev, A. V. Akimov, and M. Bayer. Acousto-optical nanoscopy of buried photonic nanostructures. *Optica*, 4:588, 2017.

[33] T. Czerniuk, J. Tepper, A. V. Akimov, S. Unsleber, C. Schneider, M. Kamp, S. Höfling, D. R. Yakovlev, and M. Bayer. Impact of nanomechanical resonances on lasing from electrically pumped quantum dot micropillars. *Appl. Phys. Lett.*, 106:041103, 2015.

[34] T. Czerniuk, D. Wigger, A. V. Akimov, C. Schneider, M. Kamp, S. Höfling, D. R. Yakovlev, T. Kuhn, D. E. Reiter, and M. Bayer. Picosecond control of quantum dot laser emission by coherent phonons. *Phys. Rev. Lett.*, 118:133901, 2017.

[35] G. Czycholl. *Theoretische Festkörperphysik*. Springer, Berlin, 2007.

[36] S. Danworaphong, M. Tomoda, Y. Matsumoto, O. Matsuda, T. Ohashi, H. Watanabe, M. Nagayama, K. Gohara, P. H. Otsuka, and O. B. Wright. Three-dimensional imaging of biological cells with picosecond ultrasonics. *Appl. Phys. Lett.*, 106:163701, 2015.

[37] P.-L. de Assis, I. Yeo, A. Gloppe, H. A. Nguyen, D. Tumanov, E. Dupont-Ferrier, N. S. Malik, E. Dupuy, J. Claudon, J.-M. Gérard, A. Auffèves, O. Arcizet, M. Richard, and J.-P. Poizat. Strain-gradient position mapping of semiconductor quantum dots. *Phys. Rev. Lett.*, 118:117401, 2017.

[38] C. Degen, I. Fischer, and W. Elsäßer. Transverse modes in oxide confined VCSELs: Influence of pump profile, spatial hole burning, and thermal effects. *Opt. Express*, 5:38, 1999.

[39] T. Dehoux, M. A. Ghanem, O. F. Zouani, M. Ducousso, N. Chigarev, C. Rossignol, N. Tsapis, Ma.-C. Durrieu, and B. Audoin. Probing single-cell mechanics with picosecond ultrasonics. *Ultrasonics*, 56:160, 2015.

[40] H. Deng, G. Weihs, D. Snoke, J. Bloch, and Y. Yamamoto. Polariton lasing vs. photon lasing in a semiconductor microcavity. *Proc. Natl. Acad. Sci. USA*, 100:15318, 2003.

[41] X. Ding, Y. He, Z.-C. Duan, N. Gregersen, M.-C. Chen, S. Unsleber, S. Maier, C. Schneider, M. Kamp, S. Höfling, C.-Y. Lu, and J.-W. Pan. On-demand single photons with high extraction efficiency and near-unity indistinguishability from a resonantly driven quantum dot in a micropillar. *Phys. Rev. Lett.*, 116:020401, 2016.

[42] R. Dingle, A. C. Gossard, and W. Wiegmann. Direct observation of superlattice formation in a semiconductor heterostructure. *Phys. Rev. Lett.*, 34:1327, 1975.

[43] H. Euchner, S. Pailhès, L.-T.-K. Nguyen, W. Assmus, F. Ritter, A. Haghighirad, Y. Grin, S. Paschen, and M. de Boissieu. Phononic filter effect of rattling phonons in the thermoelectric clathrate $Ba_8Ge_{40+x}Ni_{6-x}$. *Phys. Rev. B*, 86:224303, 2012.

[44] A. Fainstein, N. D. Lanzillotti-Kimura, B. Jusserand, and B. Perrin. Strong optical-mechanical coupling in a vertical GaAs/AlAs microcavity for subterahertz phonons and near-infrared light. *Phys. Rev. Lett.*, 110:037403, 2013.

[45] J. E. G. Farina. *International Encyclopedia of Physical Chemistry and Chemical Physics*, volume 1. Pergamon, Oxford, 1975. Topic 2.

[46] M. Feneberg, M. Röppischer, C. Cobet, N. Esser, J. Schörmann, T. Schupp, D. J. As, F. Hörich, J. Bläsing, A. Krost, and R. Goldhahn. Optical properties of cubic GaN from 1 to 20 eV. *Phys. Rev. B*, 85:155207, 2012.

[47] L. Garwin and T. Lincoln, editors. *A century of nature: twenty-one discoveries that changed science and the world*, page 107. University of Chicago Press, 2003.

[48] J. M. Gérard, B. Sermage, B. Gayral, B. Legrand, E. Costard, and V. Thierry-Mieg. Enhanced spontaneous emission by quantum boxes in a monolithic optical microcavity. *Phys. Rev. Lett.*, 81:1110, 1998.

[49] B. A. Glavin, V. A. Kochelap, T. L. Linnik, K. W. Kim, and M. A. Stroscio. Generation of high-frequency coherent acoustic phonons in superlattices under hopping transport. I. Linear theory of phonon instability. *Phys. Rev. B*, 65:085303, 2002.

[50] B. A. Glavin, V. A. Kochelap, T. L. Linnik, K. W. Kim, and M. A. Stroscio. Generation of high-frequency coherent acoustic phonons in superlattices under hopping transport. II. Steady-state phonon population and electric current in generation regime. *Phys. Rev. B*, 65:085304, 2002.

[51] R. Goldhahn, C. Buchheim, V. Lebedev, V. Cimalla, O. Ambacher, C. Cobet, M. Rakel, N. Esser, U. Rossow, D. Fuhrmann, A. Hangleier, S. Potthast, and D. J. As. Dielectric function and critical points of the band structure for hexagonal and cubic GaN and AlN, 2004. Published online.

[52] M. Grabherr, R. Jäger, R. Michalzik, B. Weigl, G. Reiner, and K. J. Ebeling. Efficient single-mode oxide-confined GaAs VCSEL's emitting in the 850-nm wavelength regime. *IEEE Photon. Technol. Lett.*, 9:1304, 1997.

[53] H. Haken. *Laser theory.* Springer, Berlin, 1970.

[54] H.-Y. Hao and H. J. Maris. Experiments with acoustic solitons in crystalline solids. *Phys. Rev. B*, 64:064302, 2001.

[55] M. Hilbert and P. López. The world's technological capacity to store, communicate, and compute information. *Science*, 332:60, 2011.

[56] M. Hu, X. Wang, G. V. Hartland, P. Mulvaney, J. P. Juste, and J. E. Sader. Vibrational response of nanorods to ultrafast laser induced heating: theoretical and experimental analysis. *J. Am. Chem. Soc.*, 125:14925, 2003.

[57] D. L. Huffaker, D. G. Deppe, K. Kumar, and T. J. Rogers. Native oxid confined ring contact low threshold vertical cavity lasers. *Appl. Phys. Lett.*, 65:97, 1994.

[58] J. L. Jewell, J. P. Harbison, A. Scherer, Y. H. Lee, and L. T. Florez. Vertical-cavity surface-emitting lasers: Design, growth, fabrication, characterization. *IEEE J. Quantum Electron.*, 27:1332, 1991.

[59] R. Johne, N. A. Gippius, G. Pavlovic, D. D. Solnyshkov, I. A. Shelykh, and G. Malpuech. Entangled photon pairs produced by a quantum dot strongly coupled to a microcavity. *Phys. Rev. Lett.*, 100:240404, 2008.

[60] C. Jung, R. Jäger, M. Grabherr, P. Schnitzer, R. Michalzik, B. Weigl, S. Müller, and K. J. Ebeling. 4.8 mW singlemode oxide confined top-surface emitting vertical-cavity laser diodes. *Electron. Lett.*, 33:1790, 1997.

[61] V. Juvé, A. Crut, P. Maioli, M. Pellarin, M. Broyer, N. Del Fatti, and F. Vallée. Probing elasticity at the nanoscale: terahertz acoustic vibration of small metal nanoparticles. *Nano Letters*, 10:1853, 2010.

[62] A. Kavokin, J. J. Baumberg, G. Malpuech, and F. P. Laussy. *Microcavities.* Oxford science publishing, Oxford, 2007.

[63] A. V. Kavokin, G. Malpuech, A. Di Carlo, M. Vladimirova, P. Lugli, and F. Rossi. Optical polarization grating in semiconductors induced by exciton polaritons. *Phys. Rev. B*, 60:15554, 1999.

[64] H. Kazumo, K. Honda, M. Matsuya, M. Date, and C. Nielsen. Field emission SEM with a spherical and chromatic aberration corrector. *Proc. Microsc. Microanal.*, 10:1370, 2004.

[65] J. C. Knight, N. Dubreuil, V. Sandoghdar, J. Hare, V. Lefèvre-Seguin, J. M. Raimond, and S. Haroche. Mapping whispering-gallery modes in microspheres with a near-field probe. *Opt. Lett.*, 20:1515, 1995.

[66] B. Krummheuer, V. M. Axt, and T. Kuhn. Theory of pure dephasing and the resulting absorption line shape in semiconductor quantum dots. *Phys. Rev. B*, 65:195313, 2002.

[67] I. V. Kukushkin, J. H. Smet, L. Höppel, U. Waizmann, M. Riek, W. Wegscheider, and K. von Klitzing. Ultrahigh-frequency surface acoustic waves for finite wave-vector spectroscopy of two-dimensional electrons. *Appl. Phys. Lett.*, 85:4526, 2004.

[68] L. D. Landau, E. M. Lifshitz, A. M. Kosevich, and L. P. Pitaevskii. *Theory of Elasticity.* Butterworth-Heinemann, Oxford, 1986.

[69] K. L. Lear, V. M. Hietala, H. Q. Hou, J. Banas, B. E. Mammons, J. Zolper, and S. P. Kilcoyne. Small and large signal modulation of 850 nm oxide-confined vertical cavity surface emitting lasers. *Conference on Lasers and Electro-Optics*, page CWA2, 1997.

[70] Yoan Léger. Double Magic Coincidence in an Optomechanical Laser Cavity. *Physics*, 6:6, 2013.

[71] R. Lerch, G. M. Sessler, and D. Wolf. *Technische Akustik*. Springer, Berlin, 2009.

[72] M. Y. M. Leung, A. B. Djurišić, and E. H. Li. Refractive index of InGaN/GaN quantum well. *J. Appl. Phys.*, 84:6312, 1998.

[73] B. Liang, X.-S. Guo, J. Tu, D. Zhang, and J.-C. Cheng. An acoustic rectifier. *Nat. Mater.*, 9:989, 2010.

[74] Q. Lin, J. Rosenberg, D. Chang, R. Camacho, M. Eichenfield, K. J. Vahala, and O. Painter. Coherent mixing of mechanical excitations in nano-optomechanical structures. *Nat. Photon.*, 4:236, 2010.

[75] H. Machhadani, M. Tchernycheva, S. Sakr, L. Rigutti, R. Colombelli, E. Warde, C. Mietze, D. J. As, and F. H. Julien. Intersubband absorption of cubic GaN/Al(Ga)N quantum wells in the near-infrared to terahertz spectral range. *Phys. Rev. B*, 83:075313, 2011.

[76] T. H. Maimann. Stimulated optical eadiation in ruby. *Nature*, 187:493, 1960.

[77] P. A. Mante, J. F. Robillard, and A. Devos. Complete thin film mechanical characterization using picosecond ultrasonics and nanostructured transducers: experimental demonstration on SiO_2. *Appl. Phys. Lett.*, 93:071909, 2008.

[78] R. Manwar and S. Chowdhury. Experimental analysis of Bisbenzocyclobutene bonded capacitive micromachined ultrasonic transducers. *Sensors*, 16:959, 2016.

[79] W. Maryam, A. V. Akimov, R. P. Campion, and A. J. Kent. Dynamics of a vertical cavity quantum cascade phonon laser structure. *Nat. Commun.*, 4:2184, 2013.

[80] O. Matsuda, M. C. Larciprete, R. Li Voti, and O. B. Wright. Fundamentals of picosecond laser ultrasonics. *Ultrasonics*, 56:3–20, 2015.

[81] O. Matsuda, T. Tachizaki, T. Fukui, J. J. Baumberg, and O. B. Wright. Acoustic phonon generation and detection in GaAs/AlGaAs quantum wells with picosecond laser pulses. *Phys. Rev. B*, 71:115330, 2005.

[82] P. W. Milonni and J. H. Eberly. *Laser physics*. John Wiley & Sons, Hoboken, 2010.

[83] R. A. Modavis and T. W. Webb. Anamorphic microlens for laser diode to single-mode fiber coupling. *IEEE Photon. Technol. Lett.*, 7:798800, 1995.

[84] D. Moss, A. V. Akimov, S. V. Novikov, R. P. Campion, C. R. Staddon, N. Zainal, C. T. Foxon, and A. J. Kent. Elasto-optical properties of zinc-blende (cubic) GaN measured by picosecond acoustics. *J. Phys. D: Appl. Phys.*, 42:115412, 2009.

[85] D. M. Moss, A. V. Akimov, B. A. Glavin, M. Henini, and A. J. Kent. Ultrafast strain-induced current in a GaAs Schottky diode. *Phys. Rev. Lett.*, 106:066602, 2011.

[86] A. K. Nowak, S. L. Portalupi, V. Giesz, O. Gazzano, C. Dal Savio, P.-F. Braun, K. Karrai, C. Arnold, L. Lanco, I. Sagnes, A. Lemaître, and P. Senellart. Deterministic and electrically tunable bright single-photon source. *Nat. Commun.*, 5:3240, 2014.

[87] International Year of Light. About the Year of Light, 2015. http://www.light2015.org/Home/About.html.

[88] University of Toronto. Paint-on laser could rescue computer chip industry. Technical report, Edward S. Rogers Sr. Department of Electrical and Computer Engineering, 2006. www.sciencedaily.com/releases/2006/04/060417124542.htm.

[89] P. Paulitschke, N. Seltner, A. Lebedev, H. Lorenz, and E. M. Weig. Size-independent Young's modulus of inverted conical GaAs nanowire resonators. *Appl. Phys. Lett.*, 103:261901, 2013.

[90] E. Péronne, N. Chuecos, L. Thevenard, and B. Perrin. Acoustic solitons: A robust tool to investigate the generation and detection of ultrafast acoustic waves. *Phys. Rev. B*, 95:064306, 2017.

[91] R. Petkewich. Brute force breaks bonds. *Chemical & Engineering News Archive*, 85:9, 2007.

[92] S. J. Polly, S. Hellstroem, M. A. Slocum, Z. S. Bittner, D. V. Forbes, P. J. Roland, R. J. Ellingson, and S. M. Hubbard. Effect of electric field on carrier escape mechanisms in quantum dot intermediate band solar cells. *J. Appl. Phys*, 121:013101, 2017.

[93] S. Raymond, S. Studenikin, A. Sachrajda, Z. Wasilewski, S. J. Cheng, W. Sheng, P. Hawrylak, A. Babinski, M. Potemski, G. Ortner, and M. Bayer. Excitonic energy shell structure of self-assembled InGaAs/GaAs quantum dots. *Phys. Rev. Lett.*, 92:187402, 2004.

[94] S. Reitzenstein, A. Bazhenov, A. Gorbunov, C. Hofmann, S. Münch, A. Löffler, M. Kamp, J. P. Reithmaier, V. D. Kulakovskii, and A. Forchel. Lasing in high-Q quantum-dot micropillar cavities. *Appl. Phys. Lett.*, 89:51107, 2006.

[95] S. Reitzenstein and A. Forchel. Quantum dot micropillars. *J. Phys. D: Appl. Phys.*, 43:033001, 2010.

[96] S. Reitzenstein, T. Heindel, C. Kistner, A. Rahimi-Iman, C. Schneider, S. Höfling, and A. Forchel. Low threshold electrically pumped quantum dot-micropillar lasers. *Appl. Phys. Lett.*, 93:061104, 2008.

[97] S. Reitzenstein, C. Hofmann, A. Gorbunov, M. Strauß, S. H. Kwon, C. Schneider, A. Löffler, S. Höfling, M. Kamp, and A. Forchel. AlAs/GaAs micropillar cavities with quality factors exceeding 150.000. *App. Phys. Lett.*, 90:251109, 2007.

[98] S. Reitzenstein, S. Münch, P. Franeck, A. Rahimi-Iman, A. Löffler, S. Höfling, L. Worschech, and A. Forchel. Control of the strong light-matter interaction between an elongated $In_{0.3}Ga_{0.7}As$ quantum dot and a micropillar cavity using external magnetic fields. *Phys. Rev. Lett.*, 103:127401, 2009.

[99] P. Rinke, M. Winkelnkemper, A. Qteish, D. Bimberg, J. Neugebauer, and M. Scheffler. Consistent set of band parameters for the group-III nitrides AlN, GaN, and InN. *Phys. Rev. B*, 77:075202, 2008.

[100] D. Rönnow, N. E. Christensen, and M. Cardona. Deformation potentials of the E_1 transition in Ge, GaAs, InP, ZnSe, and ZnTe from ab initio calculations. *Phys. Rev. B*, 59:5575, 1999.

[101] C. Rossignol, N. Chigarev, M. Ducousso, B. Audoin, G. Forget, F. Guillemot, and M. C. Durrieu. In Vitro picosecond ultrasonics in a single cell. *Appl. Phys. Lett.*, 93:123901, 2008.

[102] N. Rotenberg and L. Kuipers. Mapping nanoscale light fields. *Nat. Photon.*, 8:919, 2014.

[103] H. Sakuma, M. Tomoda, P. H. Otsuka, O. Matsuda, O. B. Wright, T. Fukui, K. Tomioka, and I. A. Veres. Vibrational modes of GaAs hexagonal nanopillar arrays studied with ultrashort optical pulses. *Appl. Phys. Lett.*, 100:131902, 2012.

[104] C. Santori, D. Fattal, J. Vuckovic, G. S. Solomon, and Y. Yamamoto. Indistinguishable photons from a single-photon device. *Nature*, 419:594, 2002.

[105] J. Sapriel, S. Francis, and B. Kelly. *Acousto-Optics*. John Wiley & Sons, Hoboken, 1979.

[106] C. Schneider, A. Rahimi-Iman, N. Y. Kim, J. Fischer, I. G. Savenko, M. Amthor, M. Lermer, A. Wolf, L. Worschech, V. D. Kulakovskii, I. A. Shelykh, M. Kamp, S. Reitzenstein, A. Forchel, Y. Yamamoto, and S. Höfling. An electrically pumped polariton laser. *Nature*, 497:348, 2013.

[107] J. Schörmann, S. Potthast, D. J. As, and K. Lischka. In situ growth regime characterization of cubic GaN using reflection high energy electron diffraction. *App. Phys. Lett.*, 90:041918, 2007.

[108] F. J. R. Schülein, E. Zallo, P. Atkinson, O. G. Schmidt, R. Trotta, A. Rastelli, A. Wixforth, and H. J. Krenner. Fourier synthesis of radiofrequency nanomechanical pulses with different shapes. *Nat. Nano.*, 10:512, 2015.

[109] T. Schupp, K. Lischka, and D. J. As. MBE growth of atomically smooth non-polar cubic AlN. *Journal of Crystal Growth*, 312:1500, 2010.

[110] J. M. Senior and M. Y. Jamro. *Optical Fiber Communications: Principles and Practice*. Pearson Education, London, 2009.

[111] L. Shao, M. Zhang, A. Banerjee, P. K. Bhattacharya, and K. P. Pipe. Electrically driven nanoscale acoustic source based on a two-dimensional electron gas. *Appl. Phys. Lett.*, 103:083102, 2013.

[112] J. Simon, N. T. Pelekanos, C. Adelmann, E. Martinez-Guerrero, R. André, B. Daudin, L. S. Dang, and H. Mariette. Direct comparison of recombination dynamics in cubic and hexagonal GaN/AlN quantum dots. *Phys. Rev. B*, 68:035312, 2003.

[113] M. S. Skolnick, T. A. Fisher, and D. M. Whittaker. Strong coupling phenomena in quantum microcavity structures. *Semicond. Sci. Technol.*, 13:645, 1998.

[114] G. S. Solomon, M. Pelton, and Y. Yamamoto. Single-mode spontaneous emission from a single quantum dot in a three-dimensional microcavity. *Phys. Rev. Lett.*, 86:3903, 2001.

[115] J. D. Sulkin, P. M. Ferreira, and K. D. Choquette. Structured nanoaperture vertical cavity surface-emitting lasers. *IEEE J. Sel. Topics Quantum Electron.*, 19:4601504, 2013.

[116] C.-K. Sun, J.-C. Liang, and X.-Y. Yu. Coherent acoustic phonon oscillations in semiconductor multiple quantum wells with piezoelectric fields. *Phys. Rev. Lett.*, 84:179, 2000.

[117] K. S. Suslick. Sonochemistry. *Science*, 247:1439, 1990.

[118] N. Suzuki, H. Hatakeyama, K. Tokutome, K. Fukatsu, M. Yamada, T. Anan, and M. Tsuji. 1.1-µm-range InGaAs VCSELs for high-speed optical interconnections. *IEEE Photon. Technol. Lett.*, 18:1368, 2006.

[119] Ta. Suzuki, H. Yaguchi, H. Okumura, Y. Ishida, and S. Yoshida. Optical constants of cubic GaN, AlN, and AlGaN alloys. *Japanese Journal of Applied Physics*, 39, 2000.

[120] N. Swinteck, P. Lucas, and P. A. Deymier. Optically tunable acoustic wave bandpass filter. *AIP Advances*, 4:124603, 2014.

[121] J. Tamayo. Mass sensing: Optomechanics to the rescue. *Nat. Nano.*, 10:738, 2015.

[122] S. Tamura, D. C. Hurley, and J. P. Wolfe. Acoustic-phonon propagation in superlattices. *Phys. Rev. B*, 38:1427, 1988.

[123] G. Tas and H. J. Maris. Electron diffusion in metals studied by picosecond ultrasonics. *Phys. Rev. B*, 49:15046, 1994.

[124] Nippon Telegraph and Telephone. 14 Tbps over a single optical fiber: successful demonstration of world's largest capacity. Technical report, NTT Science and Core Technology Laboratory Group, 2006.

[125] Nippon Telegraph and Telephone. World record one petabit per second fiber transmission over 50-km. Technical report, NTT Science and Core Technology Laboratory Group, 2006.

[126] J. D. Teufel, T. Donner, D. Li, J. W. Harlow, M. S. Allman, K. Cicak, A. J. Sirois, J. D. Whittaker, K. W. Lehnert, and R. W. Simmonds. Sideband cooling of micromechanical motion to the quantum ground state. *Nature*, 475:359, 2011.

[127] C. Thomsen, H. T. Grahn, H. J. Maris, and J. Tauc. Picosecond interferometric technique for study of phonons in the Brillouin frequency range. *Opt. Commun.*, 60:55, 1986.

[128] C. Thomsen, J. Strait, Z. Vardeny, H. J. Maris, J. Tauc, and J. J. Hauser. Coherent phonon generation and detection by picosecond light pulses. *Phys. Rev. Lett.*, 53:989, 1986.

[129] M. Trigo, A. Bruchhausen, A. Fainstein, B. Jusserand, and V. Thierry-Mieg. Confinement of acoustical vibrations in a semiconductor planar phonon cavity. *Phys. Rev. Lett.*, 89:227402, 2002.

[130] P. J. S. van Capel, E. Péronne, and J. I. Dijkhuis. Nonlinear ultrafast acoustics at the nano scale. *Ultrasonics*, 56:36, 2015.

[131] V. Villafañe, P. Soubelet, A. E. Bruchhausen, N. D. Lanzillotti-Kimura, B. Jusserand, A. Lemaître, and A. Fainstein. Slow light and slow acoustic phonons in optophononic resonators. *Phys. Rev. B*, 94:205308, 2016.

[132] S. Weis, R. Rivière S., Deléglise, E. Gavartin, O. Arcizet, Al. Schliesser, and T. J. Kippenberg. Optomechanically induced transparency. *Science*, 330:1520, 2010.

[133] P. Westbergh, R. Safaisini, E. Haglund, B. Kogel, J. S. Gustavsson, A. Larsson, M. Geen, R. Lawrence, and A. Joel. High-speed 850 nm VCSELs with 28 GHz modulation bandwidth operating error-free up to 44 Gbit/s. *Electron. Lett.*, 48:1145, 2012.

[134] D. Wigger, T. Czerniuk, D. E. Reiter, M. Bayer, and T. Kuhn. Systematic study of the influence of coherent phonon wave packets on the lasing properties of a quantum dot ensemble. *New J. Phys.*, to be published, 2017.

[135] D. Wigger, S. Lüker, D. E. Reiter, V. M. Axt, P. Machnikowski, and T. Kuhn. Energy transport and coherence properties of acoustic phonons generated by optical excitation of a quantum dot. *J. Phys.: Condens. Matter*, 26:355802, 2014.

[136] A. F. Wright. Elastic properties of zinc-blende and wurtzite AlN, GaN, and InN. *J. Appl. Phys.*, 82:2833, 1997.

[137] A. Yamamoto, T. Mishina, Y. Masumoto, and M. Nakayama. Coherent oscillation of zone-folded phonon modes in GaAs-AlAs superlattices. *Phys. Rev. Lett.*, 73:740, 1994.

[138] A. Yariv and Pochi Yeh. *Optical waves in Crystals*. John Wiley & Sons, Hoboken, 1984.

[139] M. Yasaka. X-ray thin-film measurement techniques. *The Rigaku Journal*, 26:2, 2010.

[140] F. Yun, M. A. Reshchikov, L. He, T. King, H. Morkoç, S. W. Novak, and L. Wei. Energy band bowing parameter in AlGaN alloys. *J. Appl. Phys.*, 92:4837, 2002.

Publications

1. **T. Czerniuk**, C. Brüggemann, J. Tepper, S. Brodbeck, C. Schneider, M. Kamp, S. Höfling, B. A. Glavin, D. R. Yakovlev, A. V. Akimov, and M. Bayer. *Lasing from active optomechanical resonators.* Nat. Commun. **5**, 4038 (2014).

2. J. Schmutzler, M. Aßmann, **T. Czerniuk**, M. Kamp, C. Schneider, S. Höfling, and M. Bayer. *Nonlinear spectroscopy of exciton-polaritons in a GaAs-based microcavity.* Phys. Rev. B **90**, 075103 (2014).

3. **T. Czerniuk**, J. Tepper, A. V. Akimov, S. Unsleber, C. Schneider, M. Kamp, S. Höfling, D. R. Yakovlev, and M. Bayer. *Impact of nanomechanical resonances on lasing from electrically pumped quantum dot micropillars.* Appl. Phys. Lett. **106**, 041103 (2015).

4. C. L. Poyser, **T. Czerniuk**, A. V. Akimov, B. T. Diroll, E. A. Gaulding, A. S. Salasyuk, A. J. Kent, D. R. Yakovlev, M. Bayer, and C. B. Murray. *Coherent acoustic phonons in colloidal semiconductor nanocrystal superlattices.* ACS Nano **10**, 1163 (2016).

5. **T. Czerniuk**, D. Wigger, A. V. Akimov, C. Schneider, M. Kamp, S. Höfling, D. R. Yakovlev, T. Kuhn, D. E. Reiter, and M. Bayer. *Picosecond control of quantum dot laser emission by coherent phonons.* Phys. Rev. Lett. **118**, 133901 (2017).

6. **T. Czerniuk**, T. Ehrlich, T. Wecker, D. J. As, D. R. Yakovlev, A. V. Akimov, and M. Bayer. *Picosecond acoustics in single quantum wells of cubic GaN/(Al,Ga)N.* Phys. Rev. Applied **7**, 014006 (2017).

7. **T. Czerniuk**, C. Schneider, M. Kamp, S. Höfling, B. A. Glavin, D. R. Yakovlev, A. V. Akimov, and M. Bayer. *Acousto-optical nanoscopy of buried photonic nanostructures.* Optica **4**, 588 (2017).

8. D. Wigger, **T. Czerniuk**, D. E. Reiter, M. Bayer, and T. Kuhn. *Systematic study of the influence of coherent phonon wave packets on the lasing properties of a quantum dot ensemble.* New J. Phys., to be published (2017).

Acknowledgements

Finally i would like to thank the many people, who contributed to this thesis, supported the work, or made my time at E2 productive and enjoyable. I would like to say thank you to...

... first and foremost Prof. Manfred Bayer for his excellent guidance and giving me the opportunity to perform these studies.

... Prof. Andrey V. Akimov for his great experimental support and the many fruitful discussions. From his huge expertise this thesis benefited a lot.

... Christian Brüggemann, who was a motivating teacher during the starting period of my experimental work.

... The groups of Christian Schneider and Prof. Donat J. As for providing the high-quality samples used in the performed experiments.

... Jan Lohrenz, Daniel Schmidt, and Prof. Alexey Scherbakov for proofreading my thesis.

... Thorben Jostmeier, Jan Lohrenz, and Johannes Hackmann for the time we spend in Dortmund during our studies and in our free-time.